



Universiteit
Leiden
The Netherlands

Investigations of radiation pressure : optical side-band cooling of a trampoline resonator and the effect of superconductivity on the Casimir force

Eerkens, H.J.

Citation

Eerkens, H. J. (2017, December 21). *Investigations of radiation pressure : optical side-band cooling of a trampoline resonator and the effect of superconductivity on the Casimir force*. Retrieved from <https://hdl.handle.net/1887/59506>

Version: Not Applicable (or Unknown)

License: [Licence agreement concerning inclusion of doctoral thesis in the Institutional Repository of the University of Leiden](#)

Downloaded from: <https://hdl.handle.net/1887/59506>

Note: To cite this publication please use the final published version (if applicable).

Cover Page



Universiteit Leiden



The following handle holds various files of this Leiden University dissertation:
<http://hdl.handle.net/1887/59506>

Author: Eerkens, H.J.

Title: Investigations of radiation pressure : optical side-band cooling of a trampoline resonator and the effect of superconductivity on the Casimir force

Issue Date: 2017-12-21

Investigations of Radiation Pressure

Optical side-band cooling of a trampoline resonator
and the effect of superconductivity on the Casimir force

Proefschrift

ter verkrijging van
de graad van Doctor aan de Universiteit Leiden,
op gezag van Rector Magnificus prof.mr. C.J.J.M. Stolker,
volgens besluit van het College voor Promoties
te verdedigen op donderdag 21 december 2017
klokke 13.45 uur

door

Hedwig Julia Eerkens

geboren te Diemen
in 1987

Promotor:

Prof. dr. D. Bouwmeester (Universiteit Leiden en
UC Santa Barbara, Santa Barbara, VS)

Promotiecommissie:

Dr. E. van Heumen (Universiteit van Amsterdam)
Prof. dr. D. Iannuzzi (Vrije Universiteit)
Dr. F. Intravaia (Humboldt Universität zu Berlin,
Berlijn, Duitsland)

Prof. dr. E. R. Eliel
Prof. dr. M. P. van Exter
Prof. dr. ir. T. H. Oosterkamp

The research reported in this thesis was conducted at the Leiden Institute of Physics (LION), Leiden University. This research is supported by the NWO VICI research program, which is part of the Netherlands Organization for Scientific Research (NWO).

An electronic version of this dissertation is available at the Leiden University Repository (<https://openaccess.leidenuniv.nl>).

Typesetting and cover design by H.J. Eerkens.

to reason

to love

Contents

1	Introduction	7
1.1	Cavity optomechanics	8
1.2	Casimir effect	10
I	Cavity optomechanics	13
2	Optical Side-band Cooling of a Low Frequency Optomechanical System	15
2.1	Introduction	16
2.2	Experiment	17
2.3	Results and discussion	19
2.4	Conclusion	22
3	Parametric Amplification of the Motion of an Optomechanical Resonator	23
3.1	Parametric oscillations	24
3.2	Description of the set-up	25
3.3	Comparison to simulations	26
3.4	No transition to chaotic motion	30
4	Exploring Nested Resonators for Optomechanical Cooling	31
4.1	Optomechanical cooling	32
4.2	Influence of the outer resonator motion	34
4.3	Damping of outer resonator motion	36
4.3.1	Capacitive control of the resonator motion	37
4.3.2	Dielectric force control of the resonator motion	41
4.4	Conclusions and outlook	44

II	Casimir effect	45
5	Thermal Casimir Force and Superconductors	47
5.1	Casimir force between perfect conductors	48
5.2	Lifshitz theory for the force between real conductors	49
5.3	Models for the dielectric permittivity	52
5.4	The effect of the different models on the Casimir force	56
5.5	Casimir force between superconductors	58
5.6	Casimir force with experimental parameters	63
5.7	Conclusions and outlook	65
6	Details of the Experimental Techniques	67
6.1	Fiber interferometry	68
6.1.1	GRIN lenses to focus light	73
6.2	Sample characterization	74
6.3	Plate resistance	77
7	Simultaneous Calibration Scheme for Casimir Force Measurements	79
7.1	Detection of the plate motion	80
7.2	Calibration with the electrostatic force	82
7.2.1	Validity of the proximity force approximation	87
7.3	Casimir force measurements	89
8	Dependence of the Casimir Force on the Dielectric Permittivity of NbTiN	91
8.1	Casimir force computed from the measured optical spectrum of NbTiN	92
8.1.1	Comparison to room temperature measurements	93
8.2	Low temperature measurements	96
8.2.1	The effect of superconductivity	98
8.3	Conclusion	102
9	Increased Read-Out Sensitivity with an Optomechanical Cavity	103
9.1	Considerations for Further Improvements	104
9.2	A New Measurement Set-up	106
A	Casimir force in terms of reflection coefficients	109
	Bibliography	111
	Samenvatting	123
	Curriculum Vitae	127
	List of Publications	129
	Acknowledgements	131
	Index	133

The interaction between electromagnetic radiation and an object results in a pressure exerted on its surface. This is known as radiation pressure. The interaction can be (a combination of) reflection, absorption or emission of the electromagnetic radiation. Under normal, everyday circumstances, this pressure is too small to be detected. But when the amount of radiation is increased, or when the reflective or absorbing object is sufficiently small or well isolated, radiation pressure can become significant.

It was Kepler who first put forward the notion of radiation pressure [1], observing that a comet's tail always points away from the sun. It was later put in the frame of electromagnetism by Maxwell [2]. The first experiments detecting radiation pressure were conducted by Lebedev [3] and Nichols and Hull [4] around 1900. It took many years until radiation pressure could be used to influence the Brownian motion of a mechanical resonator [5–7]. Since then, research in radiation pressure has increased enormously, with applications reaching as far as gravitational wave detectors [8].

In this thesis we will investigate two separate manifestations of radiation pressure. The interaction of electromagnetic radiation with a micromechanical resonator is studied in the field of optomechanics. The possibility to couple quantum mechanical photon states to the motion of a macroscopic mirror allows the experimental investigation of macroscopic quantum superpositions and novel decoherence mechanisms. In this thesis we will investigate the first steps necessary to achieve a macroscopic superposition, namely optical cooling of the mirror. Our results will be discussed in the first three chapters of this thesis.

The radiation pressure exerted by vacuum fluctuations is more generally known as the Casimir force. As it is based on electromagnetism, which is well understood, the occurrence of new physics can be excluded as long as measurements of the Casimir force overlap with theoretical calculations. This has inspired Casimir force measurements as tests in the search of new physics [9–11]. But the Casimir force also finds applications, mainly in the design of nano- and microelectromechanical systems (NEMS and MEMS). These systems operate in the regime where the Casimir force is significant and good understanding of the force may lead to new possibilities to tune their properties. We will measure the Casimir force between

superconducting materials, in order to better understand its dependency on the reflectivity of the surfaces. The last five chapters of this thesis are dedicated to the Casimir effect.

1.1 Cavity optomechanics

Macroscopic quantum states could be created via entanglement of a microscopic quantum state with a macroscopic state. A famous example of a macroscopic superposition created in such a way is Schrödinger's cat [12]. This thought experiment posed the question where the boundary between the quantum and classical world could be found, if such a boundary indeed exists.

A more realistic method of creating entanglement between micro- and macroscopic states, that does not endanger cats, is via radiation pressure. When light is trapped inside an optical cavity, it exerts an enhanced pressure on the end mirrors. Coupling between the cavity light and the macroscopic mirror motion can be obtained if one of the end mirrors is free to move. When the coupling is strong enough, even a single photon can exert enough pressure to significantly influence the mirror motion. This enables the transfer of the quantum mechanical properties of the photon to the macroscopic mirror [13, 14] and the investigation of the mechanism behind the decoherence of the macroscopic quantum state.

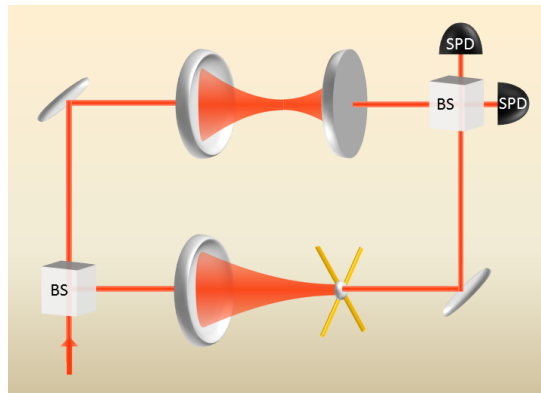


Figure 1.1: Artist impression of a set-up to create and investigate macroscopic superpositions. A single photon is brought into a superposition between two optical paths via a beam splitter (BS). In the lower path of the interferometer the photon interacts with a mechanical resonator that is represented by the yellow cross supporting a small mirror at its center. Note that this small mirror forms a cavity with a larger stable mirror to enhance the light-matter interaction. In the other arm a matching rigid cavity is inserted to make the two arms symmetric. If the radiation pressure exerted on the small mirror is strong enough, the photon can significantly displace the resonator. Entanglement between the photon and the resonator can be demonstrated by the interference signal at the single photon detectors (SPD).

The strong coupling of the macroscopic state to its environment generally causes a rapid decay, an effect known as environment-induced decoherence [15]. When this coupling is reduced significantly, novel decoherence mechanisms may occur [16], such as gravitationally induced decoherence [17, 18]. Several proposals investigate the possibilities to explore the foundations of quantum mechanics [19] and these novel decoherence mechanisms [20–24]. These proposals form the long-term motivation of our research and the basic idea of some of them can be described using Figure 1.1. A Mach Zehnder interferometer contains an optical cavity in each arm. The end mirror of one of these cavities is free to oscillate and can interact with a single photon that has entered the interferometer. Since this photon is in a superposition of being in either arm of the interferometer, the mirror is in a superposition of being moved by the photon and still being in the unperturbed state. This macroscopic superposition can be detected by looking at the interference signal of the single photon leaving the interferometer.

The distinguishability of the macroscopic superposition is largest when the mirror is cooled to its quantum mechanical ground state. The ground state of a harmonic oscillator is defined as its lowest energy state. Its motion is then equal to the zero-point fluctuations, with amplitude given by

$$x_{\text{zpf}} = \sqrt{\frac{\hbar}{2m_{\text{eff}}\Omega_m}}, \quad (1.1)$$

with \hbar the reduced Planck constant, m_{eff} the effective mass of the oscillator and Ω_m its angular resonance frequency. A classical resonator is in a thermal state, which is described by the Boltzmann distribution of the harmonic oscillator eigenstates. We therefore define that a resonator is in the quantum ground state when its thermal motion is less than the zero-point fluctuations defined for its mode.

Note that only the motion of a single mode of the resonator is addressed. The difference between optical cooling and changing the temperature of the bath (e.g. by placing the set-up in a cryostat), is that the other modes remain at the background temperature. It is therefore not correct to say that the resonator is cooled to a certain temperature, we can only say that the mode has an effective temperature, linked to the motion via the equipartition theorem.

The research field investigating the interaction between light in an optical cavity and the motion of a (nano- or microscopic) resonator is known as cavity optomechanics [25]. Apart from optical cooling a mechanical resonator to the quantum regime [26–30], optomechanical systems were proven to be useful for many more purposes, such as electromagnetically induced transparency (EIT) [31–33] and coherent state transfer [34, 35].

Our optomechanical system consist of an optical cavity with one large, fixed mirror with diameter 1.25 cm and radius of curvature 5 cm and one tiny mirror (diameter 60 – 130 μm) attached to four silicon nitride wires, which enable it to oscillate. The mechanical mode can be cooled optically, but also driven. Our results on cooling and driving will be discussed in chapters 2 and 3 respectively. These trampoline resonators operate at relative low frequencies of order 10^5 Hz, which makes them susceptible to external mechanical vibrations. We have therefore surrounded the

trampoline resonator with another mass-spring resonator that serves as a low-pass filter. The performance of these so-called nested resonators is discussed in chapter 4.

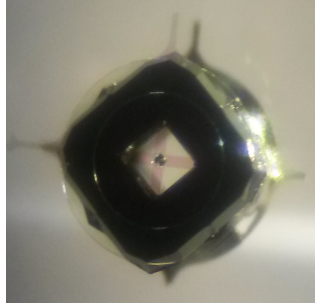


Figure 1.2: Photograph of a nested trampoline resonator that has been broken from its surrounding wafer. The small mirror is located in the center, suspended on four silicon nitride wires. The large silicon block forms the mass of the outer resonator, several of the silicon nitride arms connecting it to the wafer are still visible.

1.2 Casimir effect

Even when there is no light source available, radiation pressure can be exerted by the electromagnetic vacuum field. The vacuum is not empty, but filled with short-lived virtual particles. These particles can be of any type, depending on the vacuum field that they constitute. The electromagnetic vacuum field is made up of virtual photons, which can also be viewed as electromagnetic waves fluctuating around an expectation value of zero [36].

The vacuum state can also have an effect on macroscopic bodies. When two parallel plates are brought in each other's vicinity, the radiation pressure of the vacuum in between pushes them apart, while the vacuum outside the plates pushes them together. This is imaged in Figure 1.3 for the experimentally more accessible situation of a sphere near a plate. The surfaces set boundary conditions on the vacuum field, such that there are less modes possible between the plates than there are outside. This difference increases as the plates are brought closer together, since the density of states between the plates depends on their separation. Therefore the radiation pressure pushing the plates together is greater than the pressure exerted to keep them apart, which results in an attractive force between the plates, caused solely by the vacuum fluctuations and the boundary conditions of the plates. This effect was named after its discoverer Hendrik Casimir [37]. Casimir was interested in the van der Waals interaction between particles and had already discovered, together with Polder, that the interaction between an atom and a plate at relative large distances is influenced by retardation effects caused by the finite speed of light. A different approach to the Casimir force is that it is caused by the van der Waals interaction between the atoms of the plates under the influence of retardation.

The Casimir force is best known as a result of the zero-point fluctuations of the electromagnetic field. But other quantized fields with a vacuum state, like the

Dirac field [36], can also give rise to a Casimir effect, as long as suitable mirrors exist for that field. According to some proposals, superconductors form mirrors for gravitational waves, such that two parallel superconducting plates may give rise to a Casimir force caused by quantum fluctuations in the gravitational field [38, 39]. Analogies of the Casimir force can also be found in the classical world, as the force between parallel plates in a liquid [40] or between beads on a string [41, 42].

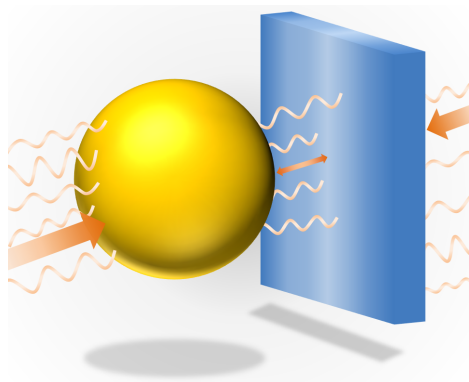


Figure 1.3: Artist impression of the Casimir force between a sphere and a plate. The electromagnetic waves of the vacuum exert radiation pressure on the surfaces. Since there are less waves between the sphere and plate, a result of their boundary conditions, the net pressure, as indicated by the arrows, is inwards.

The first experiments of the Casimir force were conducted soon after its discovery. Although they could not lead to a perfect comparison to theory due to a lack of optical data of the materials, they at least showed a qualitative agreement [43, 44] or even a good quantitative agreement [45, 46]. With the rise of nanotechnology, new methods for precision force measurements have become available, such that conclusive demonstration of the Casimir force became possible [47].

Casimir's calculation assumed that the plates were made of perfect conductors, which reflect all electromagnetic waves at all frequencies. The resulting force per area A for two plates at a distance d is given by

$$F_C = -\frac{\pi\hbar c A}{120d^4}, \quad (1.2)$$

with \hbar the reduced Planck constant and c the speed of light. Normal conductors, metals and dielectrics aren't perfect conductors, and their reflectivity is determined by the frequency dependent dielectric permittivity, which lowers the Casimir force compared to perfect conductors. Calculation of the force between real conductors is possible via the formulation developed by Lifshitz. But how exactly the dielectric permittivity affects the Casimir remains open to debate [48, 49]. The low frequency contribution needs to be extrapolated via models, but it is an open question whether to use the Drude or the plasma model. The difference is that the Drude model accounts for dissipation in the material and the plasma model does not. Precision

measurements of the Casimir force, both at room temperature and at low temperature [11, 50–54], so far have not given a satisfactory answer.

Since the dielectric permittivity is different in superconductors, comparison of the Casimir force between normal conductors and superconductors may give more insight in the exact influence of the dielectric permittivity [55]. In this thesis we investigate how the Casimir force between gold and niobium titanium nitride (NbTiN) changes as the NbTiN crosses the superconducting transition. Our set-up uses a microsphere (radius $100\ \mu\text{m}$) attached to an atomic force microscopy cantilever as a force sensor. A force gradient experienced by the cantilever changes its resonance frequency, which can be detected by a fiber-based interferometer. A photograph of the sphere, cantilever and fiber interferometer is shown in Figure 1.4. The plate is positioned underneath the sphere, on top of a translation stage used to set the distance.

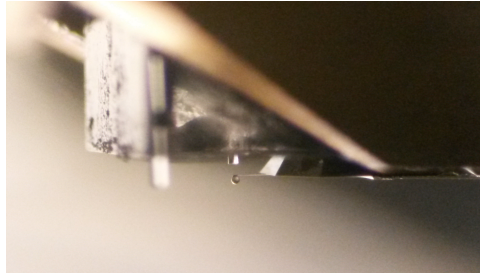


Figure 1.4: Photograph of the microsphere attached to a micromechanical cantilever. A single mode fiber is positioned above the cantilever for interferometric read-out of the cantilever motion. The plate (not shown in the image) is located below the sphere and can be positioned near it by a translation stage.

Measurements of the Casimir force are hindered by three technical aspects. The measurement apparatus needs to be calibrated, the actual distance between the surfaces has to be determined and compensation of the electrostatic force caused by the difference in work function of the materials is required. People therefore precede their force measurements by extensive calibrations. However, the system can drift between the calibrations and the measurements, causing discrepancies between the measured forces and calculations. Our set-up employs a real-time calibration scheme, based on modulation of the electrostatic force. Our Casimir force measurements now run simultaneously with our calibration, thereby practically eliminating the chance of discrepancies.

The second part of this thesis is dedicated to the Casimir effect. The theoretical background is described in chapter 5, chapter 6 gives details of some of the experimental techniques and the experimental set-up and method are explained in chapter 6. With this set-up we were able to measure the Casimir force between gold and a superconductor, the results will be discussed in chapter 8. The final chapter, chapter 9, contains some proposals to improve the force sensitivity.

PART I

Cavity optomechanics

Optical Side-band Cooling of a Low Frequency Optomechanical System

For experimental investigations of macroscopic quantum superpositions and the possible role of gravitational effects on the reduction of the corresponding quantum wave function it is beneficial to consider large mass, low frequency optomechanical systems. We report optical side-band cooling from room temperature for a 1.5×10^{-10} kg (mode mass), low frequency side-band resolved optomechanical system based on a 5 cm long Fabry-Perot cavity. By using high-quality Bragg mirrors for both the stationary and the micromechanical mirror we are able to construct an optomechanical cavity with an optical linewidth of 23 kHz. This, together with a resonator frequency of 315 kHz, makes the system operate firmly in the side-band resolved regime. With the presented optomechanical system parameters cooling close to the ground state is possible. This brings us one step closer to creating and verifying macroscopic quantum superpositions.

This chapter has previously been published: H. J. Eerkens, F. M. Buters, M. J. Weaver, B. Pepper, G. Welker, K. Heeck, P. Sonin, S. de Man, and D. Bouwmeester, "Optical side-band cooling of a low frequency optomechanical system," *Opt. Express*, **23**, 8014-8020, (2015).

2.1 Introduction

In optomechanics, interesting phenomena occur when the photon-phonon coupling is sufficiently large. Amongst other things side-band cooling to the quantum mechanical ground state [27, 28], electromagnetically induced transparency (EIT) [31, 32] and coherent state transfer [34, 35] have been demonstrated. For all these experiments good optical and mechanical quality of the set-up is required.

To use side-band cooling to reach the quantum mechanical ground state of a mechanical resonator, the cavity linewidth κ needs to be smaller than the mechanical resonator frequency Ω_m (side-band resolved regime) [56, 57]. This condition is not sufficient, since it does not specify the number of photons required, the maximum environmental temperature and the requirements for the mechanical damping rate Γ_m . A more suitable parameter is the multi-photon cooperativity: $C = 4g_0^2\bar{n}_{cav}/(\kappa\Gamma_m)$ with $g_0 = (\omega_{cav}/L)\sqrt{\hbar/2m\Omega_m}$ the optomechanical coupling rate, ω_{cav} the cavity resonance frequency, L the cavity length, m the mode mass and \bar{n}_{cav} the mean cavity photon number. When $C + 1 \gg \bar{n}_{th}$, with \bar{n}_{th} the mean phonon number of the environment, optical cooling to the ground state is possible [25].

From the cooperativity it is clear that indeed a good mechanical (small Γ_m) and optical quality factor (small κ) are needed. It also follows that when the mode mass of the mechanical resonator becomes larger, the requirements on the other parameters become more strict. Therefore most of the optomechanical devices investigated so far operate in the small mass (below $\sim 1 \times 10^{-12}$ kg), high frequency (above 1 MHz) range [27, 28, 58–62]. However, to investigate the possible involvement of gravity in the quantum to classical transition of macroscopic superpositions, large mass resonators are essential [21–24]. Another difficulty in using large mass resonators for these purposes is the low mechanical frequency, which makes reaching the side-band resolved regime difficult.

Here we present a 315 kHz optomechanical system that is sufficiently side-band resolved for ground state cooling. We have constructed an optomechanical system based on a Fabry-Perot cavity with a trampoline resonator as moving end mirror [63]. The trampoline resonator consists of a circular mirror (diameter 70 μm) hanging from four 200 μm long Si_3N_4 arms. High-quality Bragg mirrors (alternating $\text{Ta}_2\text{O}_5/\text{SiO}_2$ layers with 22 ppm transmission loss and order ppm absorption) on both the stationary and the micromechanical mirror allow us to construct a side-band resolved cavity with $\Omega_m/\kappa \approx 13.5$.

To demonstrate the capabilities of our system, we perform a side-band cooling experiment where we have $\sim\text{kHz}$ resolution of the pump laser frequency with respect to the cavity resonance. We match the experimental results to theory and find excellent agreement. The system parameters found with the side-band cooling experiment are in good agreement with parameters found from characterization measurements. These results show that with a lower base temperature, ground state cooling should be achievable. This brings investigation of the quantum to classical transition with large mass resonators one step closer.

2.2 Experiment

Our system consists of a 5 cm long Fabry-Perot cavity, operating around 1064 nm, with a trampoline resonator as the moving end mirror [63]. The trampoline resonator used in the experiments presented here has a mirror diameter of $70 \mu\text{m}$, a resonance frequency of 315 kHz, and a mode mass of 1.5×10^{-10} kg (determined using COMSOL). The optical quality of the cavity is obtained by measuring an optical cavity ring-down. For this, a resonant laser beam is quickly shut down with an acousto-optical modulator (AOM) and the decaying intensity of the transmitted light is recorded. Characterization of the mechanical resonator is done by measuring its mechanical thermal noise spectrum with a laser locked to a cavity resonance using the Pound-Drever-Hall (PDH) technique [64]. The laser power is kept sufficiently low to avoid optomechanical effects on the mechanical linewidth.

Optical side-band cooling occurs when a laser is placed precisely one mechanical frequency below a cavity resonance (see inset in Figure 2.1). Interaction of the laser with the mechanical resonator leads to up- and down-conversion of the laser frequency, creating an upper and lower side-band. The upper side-band is resonant with the cavity and the up-conversion process is therefore enhanced compared to the down-conversion process. The net effect is the extraction of energy (phonons) from the mechanical mode of the resonator.

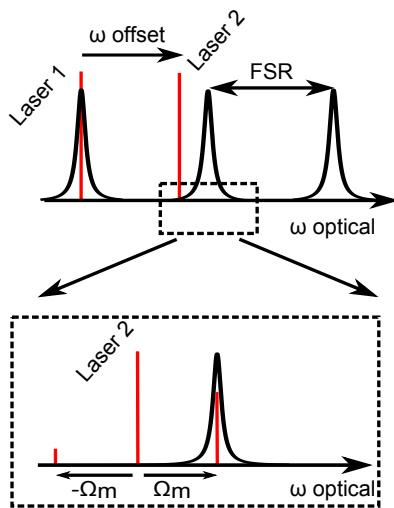


Figure 2.1: The laser scheme used for side-band cooling. Laser 1 is locked to a cavity resonance and laser 2 is locked to the first laser with a variable offset. Inset: Laser 2 is placed precisely one mechanical frequency below a cavity resonance for optimal cooling.

Since the experiment is carried out at room temperature, thermal drift and low frequency mechanical noise can potentially limit the measurement time. To compensate for these, a measurement scheme containing two lasers is used. The frequency of one laser, laser 1 in Figure 2.1, is locked to a cavity resonance using the PDH tech-

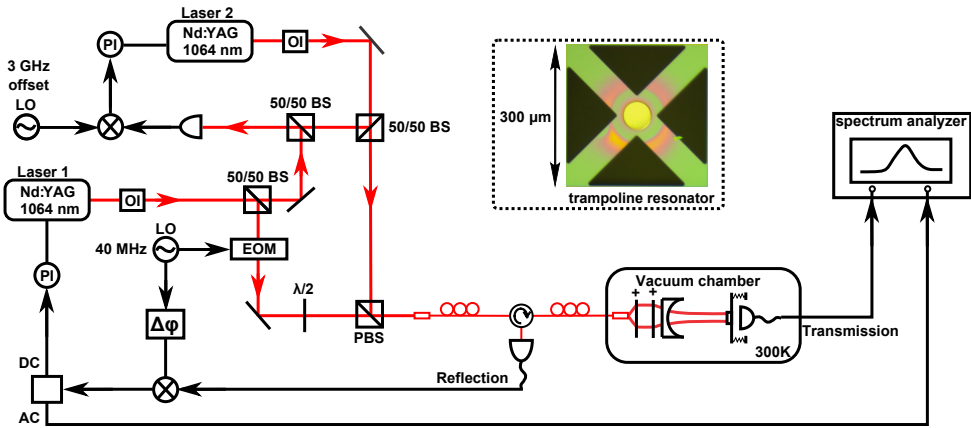


Figure 2.2: Simplified schematic of the optical set-up. The frequency of laser 1 is locked to the optomechanical cavity using the Pound-Drever-Hall (PDH) technique. Laser 2 is locked to laser 1 via an optical phase-locked loop (OPLL). Laser 2 is tuned one free spectral range (FSR) apart from laser 1 to avoid interference at frequencies relevant to the experiment. The components displayed are: LO: local oscillator, BS: beam splitter, PBS: polarizing beam splitter, EOM: electro-optical modulator, OI: optical isolator and PI: proportional-integral feedback controller. Inset: optical image of the trampoline resonator.

nique. This laser follows slow changes in the cavity length and provides a frequency reference for the second laser, laser 2 in Figure 2.1. This second laser is locked with a tunable frequency difference to the first laser with an optical phase-locked loop (OPLL) operating around 3 GHz. The frequency offset is chosen such that the second laser is close to the next cavity resonance, one free spectral range (FSR) away, to avoid unwanted interference of the two lasers at frequencies relevant to the experiment.

Figure 2.2 shows a simplified schematic of the optical set-up. For clarity, the optical components needed for the optical cavity ring-down measurement are omitted. The optomechanical cavity is placed inside a vacuum chamber ($p < 10^{-5}$ mbar) with several eddy current dampers and springs. Two \sim kHz linewidth piezo-tunable Nd:YAG lasers operating at 1064 nm are used. To realize the PDH locking scheme, laser 1 is sent through an electro-optical modulator (EOM) [64]. The light reflected from the cavity is, via a fiber circulator, picked up with an avalanche photodiode (APD). The electrical signal is mixed with the local oscillator (LO) at 40 MHz that also drives the EOM. The low-frequency part is routed to a PI controller (\sim 30 kHz bandwidth) to lock the frequency of laser 1 to a cavity resonance. The high-frequency part is sent to a spectrum analyzer to record the mechanical thermal noise spectrum of the mechanical resonator, both for the mechanical characterization and for the side-band cooling experiment.

To lock laser 2 with a variable frequency difference to laser 1 via an OPLL, the beat signal of laser 1 and 2 is continuously monitored using a fast PIN diode. This signal is mixed with a local oscillator around 3 GHz to provide the error signal for

the OPLL, which is directed to a fast PI-controller. By adjusting the frequency of the OPLL LO, laser 2 can be set to a specific cavity detuning.

By using a cavity resonance as frequency reference, any thermal drift is compensated for. The frequency tunable range of the lasers via the piezos is limited to approximately 10 MHz. However, both lasers are also temperature tunable over a broader frequency range (~ 1 GHz), although with < 1 Hz bandwidth. We have therefore implemented a slow temperature feedback loop for each laser that enables us to measure for many hours with a fully automated measurement protocol.

2.3 Results and discussion

First we show the results of the optical and mechanical characterization. This provides information about the mechanical frequency Ω_m , mechanical linewidth Γ_m and optical linewidth κ . From the optical cavity ring-down measurement in Figure 2.3(a) we obtain a cavity linewidth κ of $2\pi \times 23.2 \pm 0.1$ kHz, which corresponds to a finesse of 129000. Given the small diameter of the mirror and the multiple clean room fabrication steps it went through, it is remarkable that the optical finesse almost reaches the theoretical maximum of 140000 set by the coating of our Bragg mirrors. For the mechanical characterization, the mechanical thermal noise spectrum is recorded and a Lorentzian is fitted to it, as is shown in Figure 2.3(b). From the fit we find $\Gamma_m = 2\pi \times 3.3 \pm 0.14$ Hz, corresponding to a mechanical quality factor of 95000. From the optical and mechanical characterization alone it is clear that our optomechanical system is in the side-band resolved regime with $\Omega_m/\kappa \approx 13.5$. The small linewidth of the optical cavity allows for a large intracavity laser power with only modest input. Since the light is circulating in vacuum, rather than for example silica, secondary effects due to absorption do not play a role, as in [60]. These two ingredients contribute to a large intracavity photon number and therefore also to a large multi-photon cooperativity. We estimate, using the current system parameters, that a cooperativity of $10^5 - 10^6$ is possible depending on laser input power.

To demonstrate the “side-band resolvedness” of our system, we perform a side-band cooling experiment. We change the laser detuning of the strong pump beam (laser 2) in small steps of 5 kHz by varying the OPLL LO and measure the mechanical thermal noise spectrum. The laser power of the pump beam is about 50 times higher than the power of the read-out laser. In Figure 2.4(a) the mechanical thermal noise spectrum together with a Lorentzian fit is shown for two specific detunings. The top curve shows the spectrum for $\Delta = \omega_{laser} - \omega_{cav} = -2\Omega_m$ and the bottom curve shows the spectrum for $\Delta = -\Omega_m$.

Clearly the linewidth is larger and the integrated area smaller for the bottom mechanical thermal noise spectrum, indicating both damping and cooling. The integrated area can be related to an effective temperature via the equipartition theorem since $\langle x^2 \rangle = \frac{k_B T}{m\Omega_m^2}$. When the pump laser is off, the mechanical resonator is not cooled, so its effective temperature is equal to the environmental temperature of 300 K, assuming good thermalization with the environment. Therefore we set the related integrated area to correspond to an effective temperature of 300 K. When the pump laser is on, the effective temperature for each specific detuning is obtained

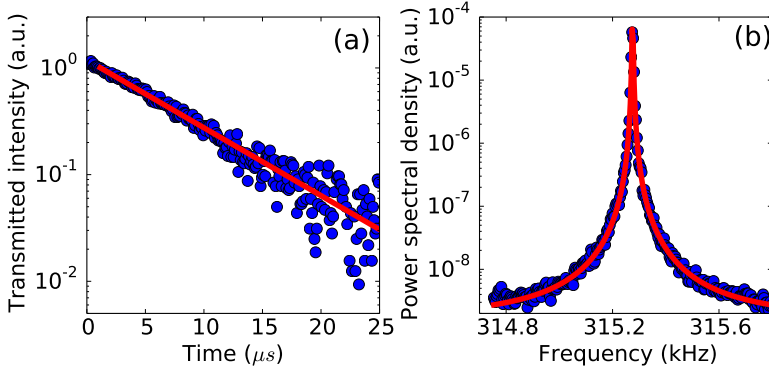


Figure 2.3: Characterization of the optomechanical system: (a) Optical cavity ring-down measurement with an exponential fit; (b) Mechanical thermal noise spectrum at 300 K with a Lorentzian fit.

by comparing the integrated area of each mechanical thermal noise spectrum to the integrated area of the mechanical thermal noise spectrum at 300 K. The effective optomechanical linewidth Γ_{eff} , which is broadened due to optical damping according to $\Gamma_{eff} = \Gamma_m + \Gamma_{opt}$, and the frequency shift due to the optical spring effect are also obtained from the Lorentzian fit. The results are shown in Figure 2.4(b)–2.4(d) together with a fit according to the equations (see for example [25]):

$$T_{eff} = \frac{\hbar\Omega_m}{k_B} \frac{\bar{n}_{th}\Gamma_m + \bar{n}_{min}\Gamma_{opt}}{\Gamma_m + \Gamma_{opt}}, \quad (2.1)$$

$$\Gamma_{eff} = \Gamma_m + \frac{P_{in}\kappa_{ex}\omega_{cav}}{2L^2m\Omega_m(\Delta^2 + \kappa^2/4)} \left[\frac{\kappa}{(\Delta + \Omega_m)^2 + \kappa^2/4} - \frac{\kappa}{(\Delta - \Omega_m)^2 + \kappa^2/4} \right], \quad (2.2)$$

$$\delta\Omega_m = \frac{P_{in}\kappa_{ex}\omega_{cav}}{2L^2m\Omega_m(\Delta^2 + \kappa^2/4)} \left[\frac{\Delta + \Omega_m}{(\Delta + \Omega_m)^2 + \kappa^2/4} + \frac{\Delta - \Omega_m}{(\Delta - \Omega_m)^2 + \kappa^2/4} \right], \quad (2.3)$$

with $\bar{n}_{min} = (\kappa/4\Omega_m)^2$ the theoretical minimum phonon number in the side-band resolved regime, P_{in} the input power and κ_{ex} the input coupling loss rate. The fit is done simultaneously for all three curves with only the input power and cavity linewidth as free parameters. The parameters obtained from the fit are $3.07 \pm 0.04 \mu\text{W}$ for the input power of the cooling laser and $2\pi \times 23.7 \pm 2 \text{ kHz}$ for the cavity linewidth.

This value for the cavity linewidth is consistent with the value obtained from the optical cavity ring-down measurement. The excellent agreement between experiment and theory, as indicated by Figure 2.4(b)–2.4(d), and the good match between the two different methods for obtaining the cavity linewidth, shows the level of precision and control we have over the system.

We would like to stress that the sharp features resulting from the optical spring effect in Figure 2.4(d) around $\Delta = -\Omega_m$ can only be visible with a high-finesse cavity and a narrow-linewidth laser, in combination with optimal performance of the entire

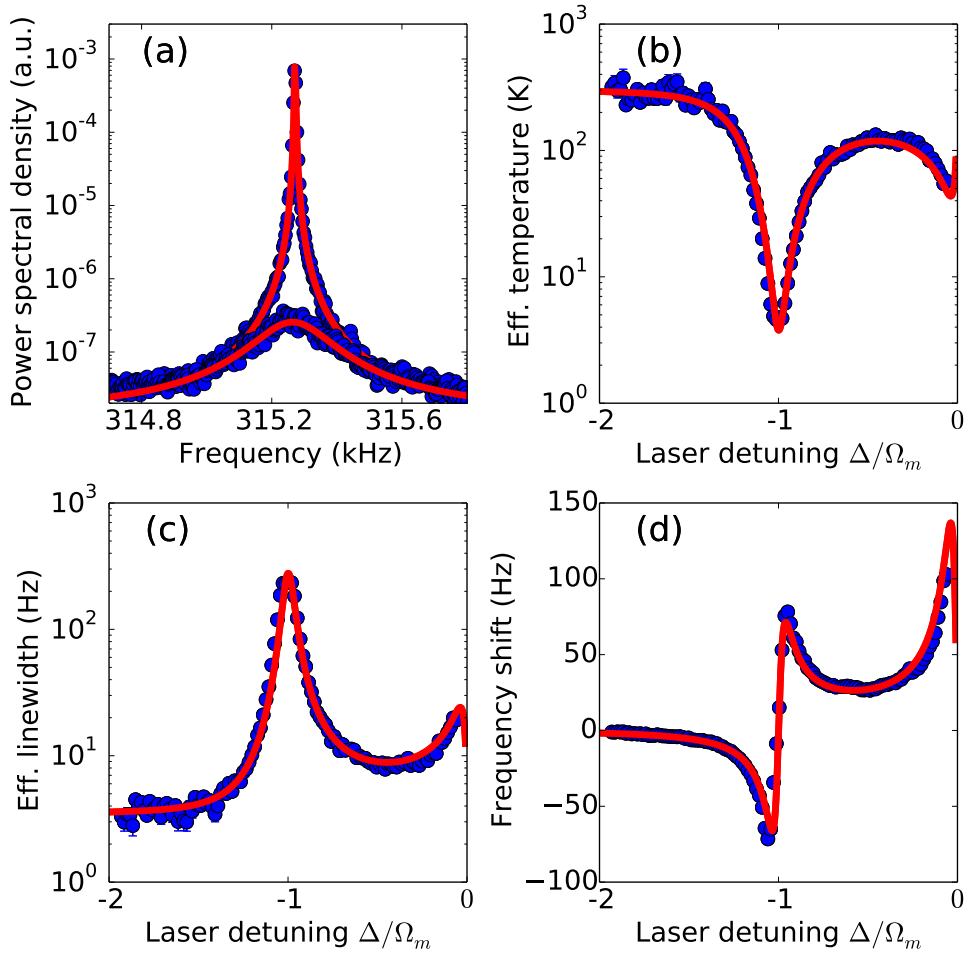


Figure 2.4: Optical side-band cooling: (a) Thermal mechanical noise spectra for $\Delta = \omega_{laser} - \omega_{cav} = -2\Omega_m$ (top curve) and $\Delta = -\Omega_m$ (bottom curve); (b) Effective temperature; (c) Effective linewidth as a result of optical damping; (d) Mechanical frequency shift due to the optical spring effect.

set-up and locking schemes. Although two narrow-linewidth lasers are used, excess laser phase noise could easily be introduced by e.g. an improper laser lock, which would blur out any sharp features such as in Figure 2.4(d) [65] and could potentially prevent ground state cooling. Observing these sharp features therefore demonstrates the cleanliness of the whole measurement chain consisting of lasers, photodetectors and feedback loops.

Although the goal of this paper is not to demonstrate large optical cooling factors, we are able to cool from room temperature to 4 K using modest laser power, as indicated in Figure 2.4(b). By increasing the laser power further, lower effective temperatures are achieved (not shown here). However, to reach the quantum mechanical ground state, the environmental temperature should be lowered significantly by placing the optomechanical cavity in a cryostat. Note that even in a cryogenic environment we can still use relatively high laser powers due to the low absorption of the mirrors. From the experimental parameters presented in this letter, we estimate that a multi-photon cooperativity of more than 10^5 is possible, indicating that a base temperature of 1 K is sufficient for ground state cooling. This is easily achievable in a variety of cryostats, bringing investigation of quantum to classical transition with low frequency resonators one step closer.

2.4 Conclusion

In this paper we have reported experiments with a high-finesse optomechanical Fabry-Perot cavity. By using high-quality Bragg mirrors for both cavity mirrors, we are able to demonstrate optical side-band cooling of a large mass, low frequency side-band resolved system ($\Omega_m/\kappa \approx 13.5$). By locking a pump laser via an optical phase-locked loop to a probe laser, we are able to achieve \sim kHz resolution laser detuning. Not only do we find a good agreement between the experiment and theory, the obtained value for the cavity linewidth from the optical cooling experiment also matches the value obtained by a separate cavity ring-down measurement. With this we demonstrate the precision of our experiment. By lowering the environmental temperature significantly, optical cooling to the quantum ground state should be possible.

Parametric Amplification of the Motion of an Optomechanical Resonator

The interaction between light and a mechanical oscillator influences the phase of the light and the motion of the oscillator. Whether the oscillator is damped or driven depends on the phase of the force introduced by the light relative to the phase of the mechanical motion. The oscillator can be damped by differentiating the motion read-out signal and then feeding back this signal by modulating the light, comparable to pushing a child on a swing. This interaction not only damps the motion, but due to the low noise of the light source also effectively cools the oscillator. This method is therefore known as active feedback cooling. Active feedback cooling was already demonstrated by using electronic read-out [66, 67] or by optical read-out [7, 68, 69].

When the light used to read out the motion of the oscillator is contained in an optomechanical cavity, the interaction between the light and mechanical oscillator enters a vicious circle where the light influences the mechanical motion, which influences the phase of the light, which influences the mechanical motion again, etcetera. The system is now described as a parametric oscillator, where the mechanical resonator is driven or damped by varying one of the parameters of the system. This can be compared to a child that pushes itself on a swing by varying the swing's moment of inertia [70]. This passive cavity cooling of a mechanical oscillator has also been demonstrated multiple times [25, 71, 72]. Instead of monitoring and altering the phase of the light, cooling is now possible by changing the frequency of the laser light with respect to the cavity resonance. Optical cooling occurs when the laser is detuned to the red side of the resonance, below the cavity frequency.

At the blue side-band, the oscillator is driven which can lead to parametric instabilities [73], self-induced oscillations [74] and even chaos [75, 76]. The theoretical framework for this behaviour has also been developed [77, 78] and introduces an attractor diagram [79] that gives an overview of the optomechanical gain of the system

This chapter is based on: F. M. Buters, H. J. Eerkens, K. Heeck, M. J. Weaver, B. Pepper, P. Sonin, S. de Man and D. Bouwmeester, "Large parametric amplification in an optomechanical system," *Phys. Scr.*, **T165**, 014003, (2015).

as a function of the mirror amplitude and the laser detuning. This attractor diagram can be explored experimentally [80] and shows that at higher oscillator amplitude driving (cooling) is not restricted to the blue (red) side of the cavity resonance. In this chapter we will show large parametric amplification of our mirror motion, leading to self-induced oscillations without the appearance of chaotic motion even at large amplitudes [81].

3.1 Parametric oscillations

When the frequency of a laser is scanned across the resonance of an optomechanical cavity, the resonance peak shows up in the transmission signal read out by a photodetector. However, when the laser power is large enough and the frequency scan rate slow enough, not only the main resonance is visible, but also several side-bands appear at multiples of the mechanical resonance frequency Ω_m . An example of this transmission signal is shown in Figure 3.1, which shows the transmitted intensity as a function of the laser detuning $\Delta = \omega_{\text{laser}} - \omega_{\text{cav}}$, normalized to the mechanical frequency. Here we introduce the angular frequencies ω_{laser} and ω_{cav} for the laser and cavity respectively.

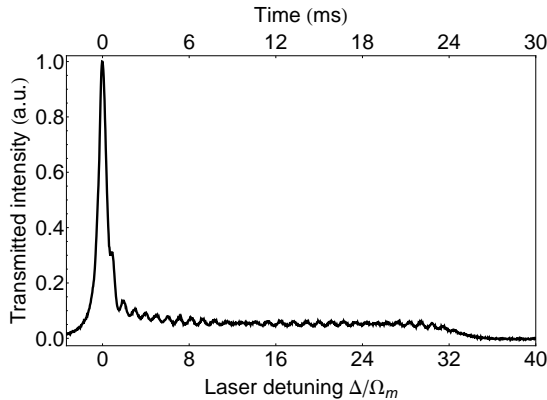


Figure 3.1: Transmission signal of a linear frequency sweep across an optomechanical cavity, the main cavity resonance is visible as well as side-bands spaced at the mechanical frequency. These side-bands are a result of parametric driving of the mechanical oscillator, while its increased amplitude creates stronger modulation of the amplitude field, which in turn allows even more driving of the oscillator.

We can understand the appearance of the side-bands with the following explanation. As the laser is scanned across the cavity resonance at ω_{cav} , the resonance peak is visible in transmission. The interaction with the mirror results in Stokes and anti-Stokes side-bands located at $\omega_{\text{cav}} \pm \Omega_m$. Here we assume that the amplitude of the mirror oscillation is small, such that no higher order side-bands are formed. The cavity light interferes with the incoming laser light, which creates a force at Ω_m acting on the mirror. However, since the side-bands appear at both sides of the cavity,

this force both damps and drives the mirror, such that in effect the mirror motion remains unaltered. The laser is then scanned slowly towards the blue side-band, at which point the interaction with the mirror results in side-bands at ω_{cav} and at $\omega_{\text{cav}} + 2\Omega_m$. The first side-band is resonant with the cavity field and is enhanced, while the second is suppressed. Since the interference of the laser light with the cavity field now only results in a driving force, the mirror amplitude is increased. This leads to a stronger optical field modulation, which in turn increases the amplitude even further, leading to an even stronger modulation, until a balance is reached. This is known as limit cycle behaviour. The laser is then detuned even further, while the larger mechanical amplitude allows the creation of increasingly more side-bands. During the sweep, the Stokes side-bands are enhanced, while the anti-Stokes side-bands remain suppressed, driving the mirror when the detuning is at multiples of the mechanical frequency.

This whole process is known as parametric amplification of the resonator, since it is induced by a change in the parameters of the system. It continues until the power loss due to friction in the system is no longer balanced by the power put into the system via the laser light. The mirror amplitude is then no longer increased and reduces to its original value given by the thermal motion of the mirror. When the laser is set back to a frequency below the cavity resonance frequency, the sweep can be repeated, leading to the same output field. Note that this parametric amplification, despite similar appearances, should not be confused with optical ringing in a high-finesse Fabry-Perot cavity [82].

3.2 Description of the set-up

Our optomechanical system is an $L = 5$ cm long confocal optical cavity where a trampoline resonator forms one of the end mirrors. The trampoline resonator consists of a Bragg mirror with diameter $60 \mu\text{m}$ attached via four Si_3N_4 wires to a silicon substrate [63]. The motion of interest is the fundamental mechanical mode with a resonance frequency of $\Omega_m/2\pi = 300$ kHz. A schematic of the set-up is given in Figure 3.2.

The light from a CW Nd:YAG laser (Coherent Mephisto) with a wavelength $\lambda = 1064$ nm passes through an optical isolator to avoid back reflections and an electro-optic phase modulator (EOM) tuned at 9.5 MHz that is used for calibration of the detuning. The light is coupled into an optical fiber that transports it into a vacuum chamber which contains the optomechanical cavity. Most of the experiments were done at a background pressure of 10^{-6} mbar. To avoid mechanical noise, a vibration isolation system containing several Eddy-current dampers decouples the optomechanical cavity from the outside world.

The laser frequency can be tuned via a piezo on the laser crystal, with a typical scan speed of 100 – 400 MHz/s, which is slow compared to the cavity life time. The light from the cavity, imprinted with the motion of the trampoline resonator, is detected by two photodetectors placed in transmission and, via an optical circulator, in reflection. The data is acquired by a digital oscilloscope (Agilent DSO-X 2004A).

The experimental parameters of our optomechanical cavity were determined sep-

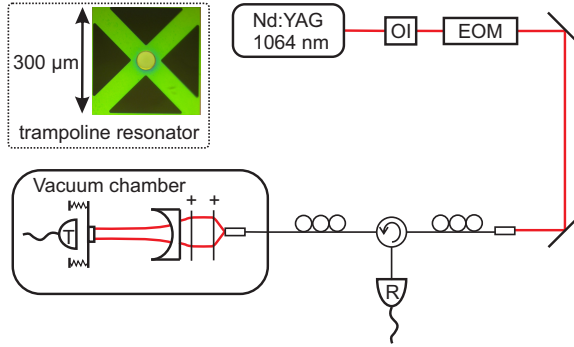


Figure 3.2: Schematic of the experimental set-up; the light of a Nd:YAG laser operating around 1064 nm is coupled into a single mode optical fiber and propagates via an optical circulator to our optomechanical cavity, which is placed inside a vacuum chamber. The transmitted light falls onto a photodetector and the reflected light is detected after passing the circulator again. The electro-optic modulator (EOM) tuned at 9.5 MHz is used to calibrate the detuning of the laser frequency with respect to the cavity. The inset shows an optical image of the trampoline resonator.

arately. The cavity linewidth $\kappa/2\pi = 300$ kHz was obtained from an optical ring-down measurement and from the thermal mechanical noise spectrum we could determine a mechanical linewidth of $\Gamma_m/2\pi = 8.8$ Hz at the background pressure of 10^{-6} mbar. This corresponds to a mechanical quality factor of $Q_m = 34000$. The intrinsic linewidth can be altered by changing the background pressure in the vacuum chamber.

3.3 Comparison to simulations

To better understand our experimental results, we compare it with simulations based on the equations of the system. There are two coupled equations of motion for our optomechanical cavity, the first describes the optical field in the cavity α and the second the displacement x of the oscillator. We have neglected thermal and mechanical noise sources.

$$\dot{\alpha}(t) = -\frac{\kappa}{2}\alpha(t) + i(\Delta + Gx(t))\alpha(t) + \sqrt{\kappa_{\text{ex}}}\alpha_{\text{in}}, \quad (3.1)$$

$$\ddot{x}(t) = -\Omega_m^2 x(t) - \Gamma_m \dot{x}(t) + \frac{\hbar G}{m_{\text{eff}}} |\alpha(t)|^2, \quad (3.2)$$

here the dot indicates the time-derivative. The other parameters are as follows: $G = \omega_{\text{cav}}/L$ the optical frequency shift per displacement, the cavity coupling loss rate $\kappa_{\text{ex}}/2\pi = 50$ kHz, α_{in} the laser field, \hbar the reduced Planck constant and $m_{\text{eff}} = 110 \times 10^{-12}$ kg the effective mass of the mechanical mode. By solving these equations of motion, we can give a more quantitative understanding of our parametric oscillator.

The motion of the mechanical oscillator is partly determined by its effective damping rate which is a sum of the intrinsic linewidth and the optomechanical damping rate $\Gamma_{\text{eff}} = \Gamma_m + \Gamma_{\text{opt}}$. An expression for Γ_{opt} in terms of the optical field and the amplitude A of the oscillator is deduced from the equation above [83]:

$$\Gamma_{\text{opt}}(A) = \frac{2\hbar G \kappa_{\text{ex}} \alpha_{\text{in}}^2}{m_{\text{eff}} \Omega_m A} \text{Im} \left(\sum_n \alpha_{n+1}^* \alpha_n \right), \quad (3.3)$$

$$\alpha_n = \frac{J_n(-GA/\Omega_m)}{\kappa/2 - i\tilde{\Delta} + in\Omega_m}, \quad (3.4)$$

where $J_n(x)$ is the Bessel function of the first kind and $\tilde{\Delta} = \omega_{\text{laser}} - \omega_{\text{cav}} + G\bar{x}$ is the effective laser detuning which also accounts for the static displacement \bar{x} of the mirror due to radiation pressure. This static displacement is small enough that we can neglect it, such that $\tilde{\Delta} \approx \Delta$.

The harmonics in the optical field are indicated by α_n for the n th harmonic. They are created by the mirror motion, which phase modulates the incoming laser light via the term $Gx(t)\alpha(t)$ in Eq. 3.1. The modulation depth is given by the argument of the Bessel function, $\phi_0 = -GA/\Omega_m$, and determines the number of side-bands that appear at frequencies $\omega = \omega_{\text{laser}} \pm n\Omega_m$. Note that the thermally excited mirror amplitude at 300 K is already sufficient to create a side-band, but more side-bands are created as the amplitude increases and more harmonics of the mechanical frequency Ω_m are imprinted on the cavity field. These side-bands are scaled by the cavity line shape as the denominator in Eq. 3.4 indicates. The modulated cavity field interacts again with the mirror, via the radiation pressure proportional to the cavity intensity $|\alpha^2|$, see Eq. 3.2. But the mirror only reacts to components of the force at the mechanical frequency, which are formed by the mixing at the moving mirror of two consecutive side-bands, $\sum_n \alpha_{n+1}^* \alpha_n$. The real part of this sum is responsible for the optical spring effect. But we are interested in optical damping or driving, which is described by the imaginary part of the sum, as is shown in Eq. 3.3.

When the optomechanical damping rate Γ_{opt} is larger than zero, the mechanical oscillator is damped and effectively cooled. But the optomechanical damping rate can also be negative. When the optomechanical damping rate overcomes the intrinsic mechanical linewidth, such that the effective linewidth is negative, self-induced oscillations occur. This is better expressed in terms of the optomechanical gain [83]:

$$\zeta_{\text{opt}} = -\frac{\Gamma_{\text{opt}}}{\Gamma_m} = \frac{P_{\text{rad}}}{P_{\text{fric}}} \quad (3.5)$$

with P_{rad} the power in the radiation pressure acting on the mirror motion, that can either be extracted from the oscillator or delivered to it. P_{fric} is the power lost from the oscillator via friction. From the ratio in Γ_{opt} and Γ_m we see that damping and cooling occurs when the optomechanical gain is smaller than zero, in this case the radiation pressure extracts power from the oscillator. Parametric oscillations occur when more power is added to the resonator than can be drained via friction, so when $\zeta_{\text{opt}} > 1$. In this situation Γ_{opt} is negative and has a larger magnitude than Γ_m , in accordance with what was mentioned before. In the intermediate regime

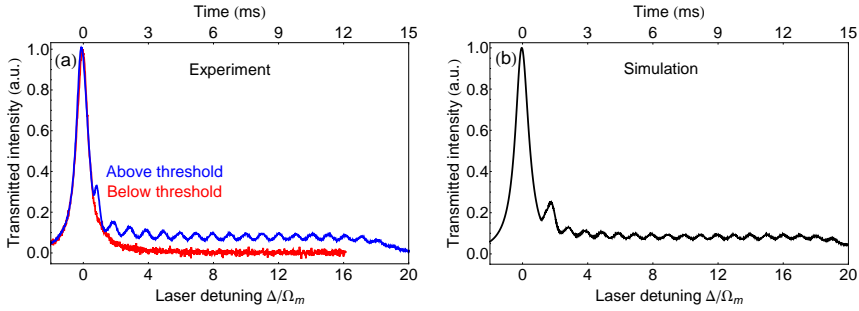


Figure 3.3: Linear frequency sweep across an optomechanical cavity resonance: (a) Experimental results below (red line) and above (blue line) the power threshold, with a mechanical quality factor $Q_m = 7300$ and scan speed 400 MHz/s; (b) Simulation based on the equations of motion of the system, with input the thermal amplitude of the mirror motion at 300 K.

$0 \leq \zeta_{\text{opt}} < 1$ the linewidth of the oscillator is reduced, but not enough for parametric oscillations to occur.

Parametric oscillations occur only above a certain power threshold, when $P_{\text{rad}} > P_{\text{fric}}$. Self-induced oscillations are therefore also known as mechanical or phonon lasing [25]. The effect of the power threshold is visible in Figure 3.3(a), which shows the experimental results of two linear frequency sweeps with a scan speed of 400 MHz/s. The two sweeps were obtained at different laser powers. No parametric oscillations occur below the power threshold, while above the power threshold oscillations continue to a detuning of $\Delta = 19\Omega_m$. The numerical simulations in Figure 3.3(b) are obtained by solving the two equations of motion, Eqs. 3.1 and 3.2. As input parameters we used $\alpha(0) = 0$, $\dot{\alpha}(0) = 0$, $x(0) = x_0$ and $\dot{x}(0) = 0$, with x_0 the thermally excited mirror amplitude at 300 K. In the simulations, the laser detuning is varied linearly across the cavity resonance while the laser power was kept constant. The simulations show excellent agreement with our experimental results above the power threshold.

When we zoom in at the optical side-bands, we should see the harmonics of the mechanical frequency imprinted on the cavity field [79]. Since our photodetector in transmission is not fast enough to see these fast modulations, we use the reflection detector. The numerical simulations are also computed in reflection. Both the numerical and experimental results are shown in Figure 3.4, for different values of the detuning. As we can see, the number of harmonics increases with larger detuning and therefore with larger amplitude of the mirror. The striking resemblance between simulations and experiment is another indication of the quality of the experimental set-up.

The self-induced oscillations occur as long as the optomechanical gain defined in Eq. 3.5 is larger than one. An indicator of the duration of the parametric oscillations is the amount of side-bands that are created. According to the definition of the optomechanical gain, this plateau length should be linear in the laser power, above a certain threshold, and inversely proportional to the mechanical linewidth. The effect of laser power is shown in Figure 3.5(a), where we have plotted the plateau length

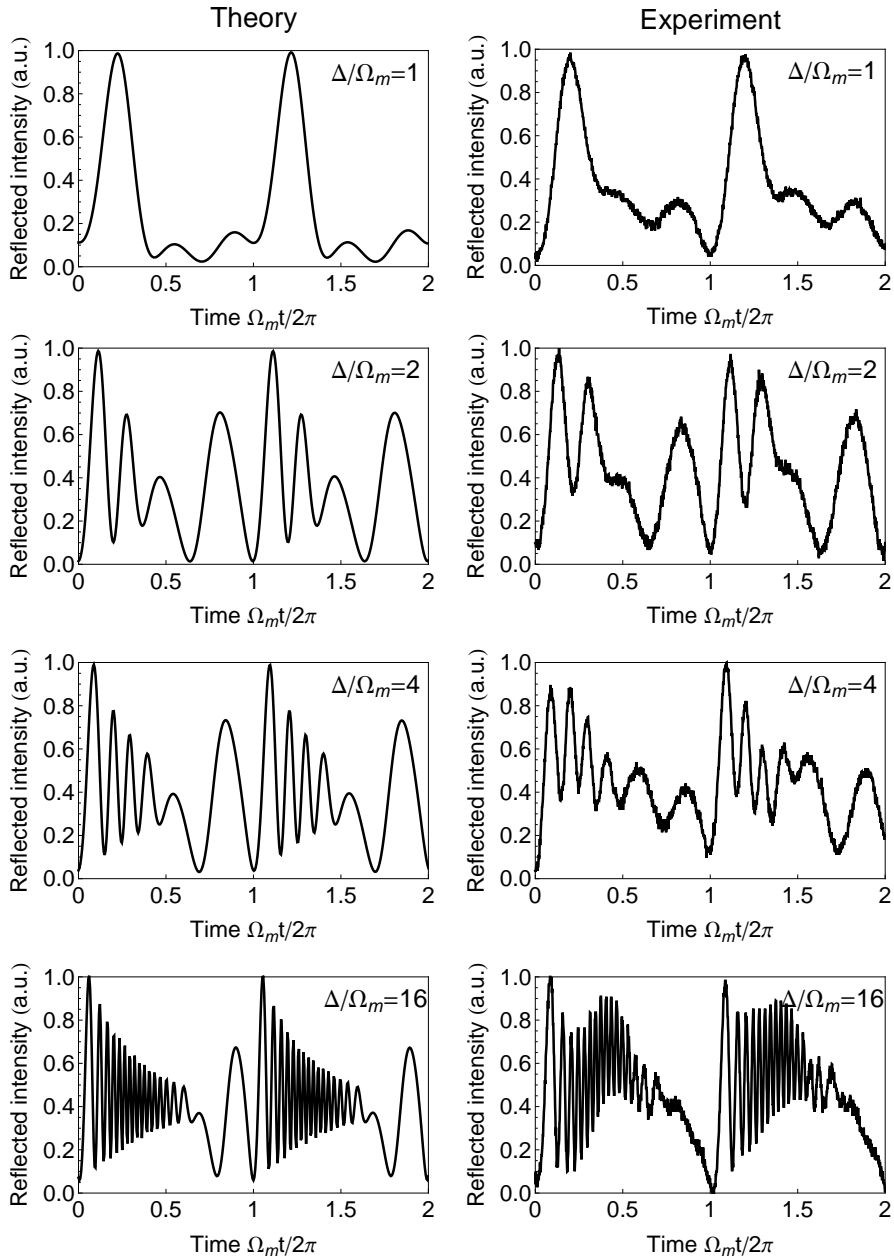


Figure 3.4: Imprint of the mechanical motion as harmonics of the mechanical frequency Ω_m on the reflected cavity field. Simulations based on solving Eqs. 3.1 and 3.2 are shown in the left column at different detunings, the experimental results at the same detuning are shown in the right column.

for different laser input powers (blue dots). There are no parametric oscillations until the power is increased enough, after which the plateau length increases linear with power. The red line is a fit to the expression in Eq. 3.5.

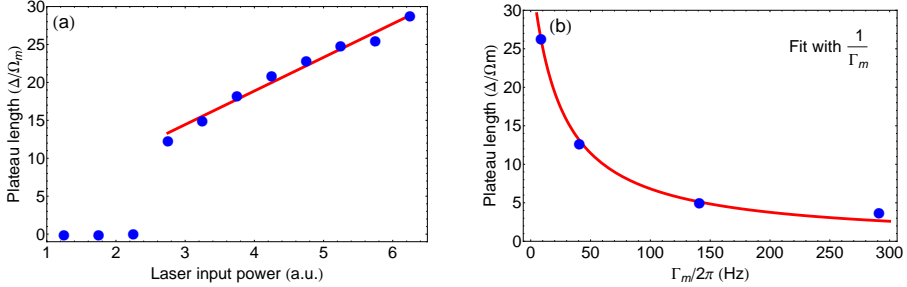


Figure 3.5: Plateau length as an indication of the optomechanical gain, the blue dots mark the amount of side-bands under different experimental conditions, the red line is a fit of the optomechanical gain: (a) Above a certain power threshold, the optomechanical gain is linear in the laser power; (b) The optomechanical gain is inversely proportional to the intrinsic mechanical linewidth.

To measure the influence of the mechanical linewidth, we have increased the background pressure in the vacuum chamber. For four different pressures, resulting in four different values of Γ_m , but at constant laser power, we have determined the plateau length, see Figure 3.5(b). The fit to ζ_{opt} shows that it is indeed inversely proportional to the mechanical linewidth. We can therefore conclude that the optomechanical gain shows the expected behaviour.

3.4 No transition to chaotic motion

We have shown that the two equations of motions introduced in Eqs. 3.1 and 3.2 are sufficient to describe the observed self-induced oscillations. When we take another look at Figure 3.1, we see parametric oscillations up to a detuning of $\Delta = 32\Omega_m$. The amplitude of the mirror at this point is found, by solving $\zeta_{\text{opt}}(\Delta = 32\Omega_m, A) < 1$, to be 450 times larger than the thermally excited mirror amplitude at 300 K.

In other systems, such high increase in amplitude is often not reached due to the transition to chaotic motion [75, 76], induced either by an extra photothermal force due to heating induced expansion of the mirror, or by the influence of outside vibrations. The absence of chaos in our system is a result of our high-quality mirror coatings with low absorption and of our good mechanical isolation from the environment. This opens the possibility of optical stabilization of the mirror at large amplitudes to greatly enhance the sensitivity when the optomechanical set-up is used for force detection [84].

Exploring Nested Resonators for Optomechanical Cooling

Optomechanical systems have gained increasing popularity over the past years for their promising possibilities to explore quantum mechanical behaviour in macroscopic objects. By coupling an optical field to a mechanical resonator, it may be possible to transfer the quantum mechanical properties of the photons to massive objects. This process is counteracted by influences from the outside world and by the thermal occupancy of the mechanical resonator. It is therefore beneficial to operate the resonator close to its quantum mechanical ground state. Several systems involving a mechanical mode with a relatively high resonance frequency have already been cooled to a phonon occupation less than one [26–30]. For lower frequency resonators the effective temperature associated with the quantum ground state lies lower, increasing the need for cryostats with lower base temperature. Since the base temperature of cryostats is limited in practice, optical side-band cooling is needed to reach lower effective mode temperatures. A higher possible optical cooling factor lowers the demand for the cryostat base temperature. In addition, low frequency resonators are more sensitive to surrounding vibrational noise. This means that the system should mechanically be better isolated from the environment.

In this chapter we will show mechanical isolation of a trampoline resonator in the form of a second resonator acting as a mechanical low-pass filter. Although this outer resonator successfully isolates the inner resonator from mechanical vibrations, its motion also influences the optomechanical response of the system.

This chapter is partially based on: M. J. Weaver, B. Pepper, F. M. Buters, H. J. Eerikens, G. Welker, B. Perock, K. Heeck, S. de Man, and D. Bouwmeester, "Nested trampoline resonators for optomechanics," *Appl. Phys. Lett.*, **108**, 033501, (2016).

4.1 Optomechanical cooling

In chapter 2 we presented optical cooling of a low frequency mechanical resonator [72]. Using a two laser scheme operating at different frequencies, it was possible to reach an effective temperature of 4 K starting from room temperature. Lower effective temperatures could not be detected due to mechanical noise in our system. This is visualized in Figure 4.1, which shows the mechanical power spectral density of a cooled resonator buried under mechanical noise peaks. This puts a limit on the observable cooling factor and therefore on the lowest effective temperature that can be measured when the optical cooling is started from a certain base temperature.

The possible cooling factor and the effect of the mechanical noise peaks depends on the intrinsic quality factor of the resonator. When the intrinsic linewidth is smaller, it can be damped more until it disappears in the background. Since the single resonators are dominated by clamping losses [85], a high quality factor cannot be guaranteed. Not only can it change every time a sample is remounted, it may also change drastically when the resonator is cooled in a cryostat.

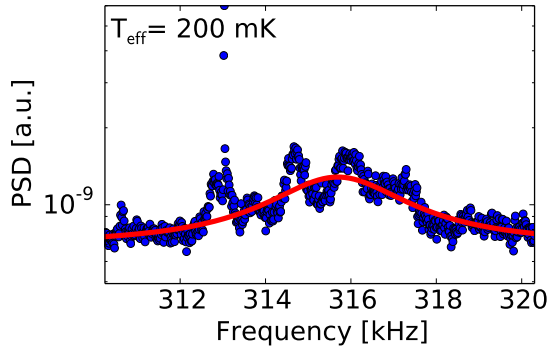


Figure 4.1: Power spectral density of a single resonator cooled to an effective temperature of 200 mK, the Lorentzian peak describing the mechanical motion is buried under mechanical noise peaks.

The exact source of the mechanical noise peaks is unknown, but it is likely that they originate from the multiple components of our set-up. With a cavity length of 5 cm it is difficult to create a monolithic system that is less prone to internal vibrations. We therefore need to isolate the trampoline resonator from the vibrations of the set-up and the cryostat. Since the noise may arise from anywhere in the set-up, we designed an on-chip isolation to be as close to the resonator as possible. An extra low frequency resonator is fabricated around the inner resonator and acts as a low-pass filter [86–90]. An optical image of this nested resonator is shown in Figure 4.2(a). The inner resonator has a mirror diameter of $80\ \mu\text{m}$ and a resonance frequency of 240 kHz. The outer resonator consists of a ring of $500\ \mu\text{m}$ thick silicon hanging from four Si_3N_4 arms. Due to the relatively large mass it has a resonance frequency of 2.4 kHz. A description of the fabrication process is given in [91].

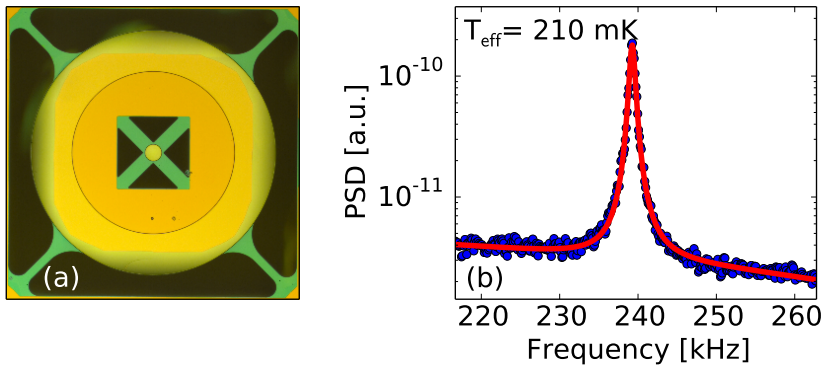


Figure 4.2: Nested resonators: (a) Optical image of a nested resonator consisting of an inner resonator with mirror diameter of $80\ \mu\text{m}$ and resonance frequency $240\ \text{kHz}$ and an outer resonator with resonance frequency $2.4\ \text{kHz}$; (b) Power spectral density of the motion of the inner resonator cooled to an effective temperature of $210\ \text{mK}$, the mechanical noise peaks are no longer visible.

To check the influence of clamping on the quality factor, the sample was mounted and remounted several times while the quality factor of both the inner and outer resonator was measured. For the outer resonator values changed by an order of magnitude, while the inner resonator quality factors varied less than ten percent [91]. So the outer resonator guarantees a consistent good quality factor of the inner resonator.

Optical cooling of the inner resonator was performed next to check the isolation provided by the outer resonator. Using the set-up described in chapter 2, the pump laser was fixed at a detuning of $\Delta = -\frac{1}{2}\Omega_m$ with respect to the cavity resonance. The laser power was then increased in steps while at each step the mode temperature was determined from the area under the mechanical power spectral density. At an effective temperature of $210\ \text{mK}$, the resonator is still clearly distinguishable and no other noise peaks are visible, see Figure 4.2(b). The outer resonator successfully isolates the inner resonator from mechanical noise, which means that we are able to detect lower effective temperatures than with a single resonator.

We increase the laser power even further to find the lowest effective temperature we can reach. The effective mode temperature as a function of pump laser power is shown in Figure 4.3(a). The effective temperature is linear in laser power, showing that we are not yet limited by phase noise in our cavity light [65]. The lowest mode temperature that could be determined is $23\ \text{mK}$. Starting from room temperature, this means a cooling power factor of 13.000. Note again that the power spectral densities in Figure 4.3(b), taken at different laser powers, show no influence of mechanical noise, even at the lowest effective temperatures. Further cooling is limited by the intrinsic linewidth of the resonator and by the stability of the system. The resonance at $23\ \text{mK}$ is barely distinguishable from the background. Further remarks on the system stability shall be given in the following sections. Still, a cooling factor of 13.000

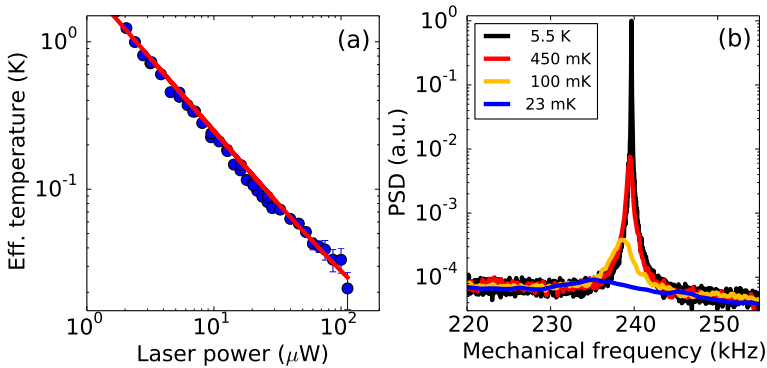


Figure 4.3: Optical cooling of a nested trampoline resonator from room temperature: (a) Effective mode temperature of the inner resonator as a function of pump laser power, a mode temperature of 23 mK is reached; (b) Power spectral densities at several effective temperatures, even at 23 mK the motion of the inner resonator can be clearly distinguished.

means that ground state cooling should be possible starting from a base temperature of 100 mK. This is an easily achievable temperature for a dilution refrigerator.

4.2 Influence of the outer resonator motion

Adding an outer resonator solves several problems, but the mechanical properties of this extra resonator also influence the cavity length and therefore also couple to the optical field. To investigate the effect of the outer resonator, we performed a sweep of the pump laser detuning with respect to the cavity resonance. The detuning was altered in steps of 5 kHz and at each step the mechanical spectrum of the inner resonator was recorded. From each spectrum we determined three parameters, the effective damping, frequency shift and effective temperature. The dependence of these parameters on the pump laser detuning is shown in Figure 4.4. The red line through the data shows a fit to the optomechanics theory. From the fits we could determine an intracavity power of $3.01 \pm 0.04 \mu\text{W}$ and a cavity linewidth of $\kappa = 52 \pm 1 \text{ kHz}$. This parameter coincides well with the previously determined value of $\kappa = 53 \text{ kHz}$ obtained from an optical cavity ring-down.

The theory fits well to the data, so it seems that the effect of the outer resonator is indeed minimal. However, when a detuning of $\Delta = -\frac{1}{2}\Omega_m$ is reached, the system becomes unstable and the laser locks, on which our measurement scheme depends, can no longer follow the cavity length changes. The value of Δ where this effect occurs is not fixed, but depends on laser power and happens sooner with higher laser power. Therefore the system also becomes unstable when the detuning is fixed at $\Delta = -\Omega_m$ and the power is increased. To fully understand this effect and the influence of the outer resonator on the system, we need to look at the schematic shown in Figure 4.5. The masses of the mirror and the silicon ring of the outer resonator are

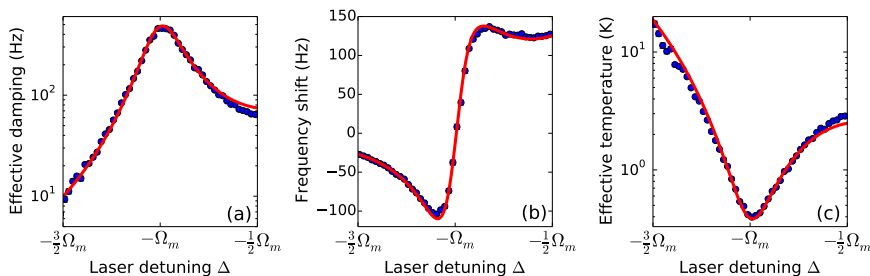


Figure 4.4: Sweep of the pump laser detuning with respect to the cavity resonance and the response of the mechanical motion of the inner resonator: (a) Effective damping; (b) frequency shift and (c) effective temperature. The blue dots show data, the red line is a fit with theory.

indicated, as well as the optical field and the big mirror at the opposite end of the cavity. The Si_3N_4 arms of both resonators are represented as a spring parallel to a damper.

The optical field interacts directly with the inner resonator. However, at frequencies below the resonance of the outer resonator, the transfer of motion between the two resonators is equal to one. This means that the resonators effectively move as a single resonator and the optical field interacts with the outer resonator as well. For clarity, we will separate the optomechanical response into two frequency ranges. For the high frequency range, the outer resonator hardly moves and the optical field only couples to the inner resonator motion. The ratio between the cavity linewidth and the mechanical frequency makes the optomechanical interaction side-band resolved, which means large optical damping and relatively small optical spring effect when the laser is detuned at $\Delta = -\Omega_m$. At low frequencies, the optical field couples effectively to both resonators, but due to a different mechanical frequency to cavity linewidth ratio, this interaction is not side-band resolved. The result is a relatively low damping effect and a large optical spring. The spring effect drives the mechanical frequency of the outer resonator down, which increases the sensitivity for low frequency noise and makes the system unstable.

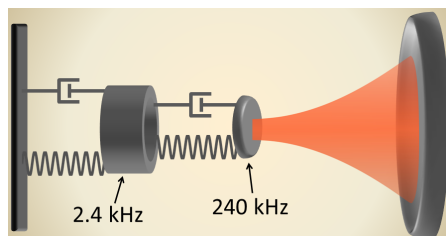


Figure 4.5: Schematic of the inner and outer resonator coupled to an optical field. The Si_3N_4 arms can be represented as a spring and a damper, with the masses coming from the mirror and the silicon ring.

Note that at positive detunings, the optical spring effect drives the resonator towards higher frequencies. The static response of the system decreases, which increases the possibility to measure at positive detunings. This is almost not possible for single resonators. Since we are ultimately only interested in cooling the outer resonator, we have not investigated this effect further.

4.3 Damping of outer resonator motion

The stability of the system is also influenced by the amplitude of the outer resonator motion. The outer resonator has a mode mass of $m_{\text{eff}} = 160 \times 10^{-9}$ kg and a resonance frequency of $\Omega_m/2\pi = 2.4$ kHz, which means that at room temperature it has an RMS motion of

$$x_{\text{rms}} = \sqrt{\langle x^2 \rangle} = \sqrt{\frac{k_B T}{m_{\text{eff}} \Omega_m^2}} = 10.6 \text{ pm}, \quad (4.1)$$

where k_B is the Boltzmann constant. Compared to the cavity length of $L = 5$ cm, the change of the cavity resonance frequency at 2.4 kHz is

$$\Delta\omega_{\text{cav}} = \omega_{\text{cav}} \frac{\Delta L}{L} = 2\pi \times 59.2 \text{ kHz}. \quad (4.2)$$

This is not a significant portion of the range of 16 MHz of our Pound-Drever-Hall (PDH) cavity frequency lock [64, 72]. But under the influence of external vibrations the outer resonator can easily be driven to an amplitude of several nanometers, beyond the reach of the lock. One solution is to prevent these vibrations, but since they can come from within the set-up, this may require yet another on-chip resonator.

It is clear that the motion of the outer resonator needs to be controlled. Since reading out the motion via the intracavity light might interfere with the already existing PDH lock, we have chosen to read out the motion using fiber interferometry [92]. A cleaved single mode fiber end is positioned behind the cavity at a distance of several hundred micrometers from the outer resonator. Light from a telecom laser ($\lambda = 1550$ nm) travels via a fiber coupler to the cleaved fiber end. The light reflected at the outer resonator surface couples back into the fiber and passes the fiber coupler again. It exits the coupler via a different portal than where the laser light originally entered and falls onto a detector. The resonator motion translates linearly to detector signal when the laser frequency is tuned at quadrature. The sensitivity of the read-out in Volts per meter can be determined from a single laser frequency scan at the start of each measurement [92]. We can therefore directly determine the resonator motion in meters.

To control the motion, we need to apply a force. There are many ways to do this, but we have chosen to investigate two different methods, which will be described and compared in this section. First we made the outer resonator one half of a parallel-plate capacitor, by coating it with a conductive aluminium layer. The other half of the capacitor is created by positioning an aluminium coated plate in its vicinity. The capacitive energy causes an electrostatic force that can be adjusted by setting the voltage across the two surfaces.

Another method to influence the resonator motion is by applying an electrostatic field gradient around the resonator [93]. This is achieved by positioning a small wire near the resonator and setting its potential with respect to the sample mount. The dielectric material of the outer resonator (silicon) polarizes in this electrostatic field and is pulled towards the wire. We are able to drive or damp the motion, depending on the phase of the feedback signal compared to the motion of the resonator.

4.3.1 Capacitance control of the resonator motion

A capacitor consists of two parallel conductive plates close together. The energy stored in the electric field between the two plates is given by

$$E = \frac{1}{2}CV^2, \quad (4.3)$$

with V the voltage across the capacitor and C the capacitance, which is equal to $C = \frac{\varepsilon A}{d}$. Here ε is the electric permittivity of the material between the plates (in our set-up this is usually vacuum or air, so we can take $\varepsilon = \varepsilon_0$), A is the overlap area and d is the distance between the plates (both unknown in our set-up). When one of the plates is free to move, the distance changes and therefore the capacitance. The force experienced by the movable plate is given by

$$F_c = -\frac{1}{2} \frac{\partial C}{\partial d} V^2 = \frac{\varepsilon_0 A V^2}{2d^2}. \quad (4.4)$$

This force can be used to control the motion of the outer resonator, when it is part of a parallel plate capacitor. Since the resonator is originally not made of conductive materials, it is coated with a conductive layer of aluminium. A second silicon wafer, pressed against the sample wafer and also coated with aluminium, serves as the second capacitor plate. If we would press the two wafers directly on top of each other, the aluminium coating would make contact, thereby eliminating the capacitance. So part of the wafer is recessed prior to coating, and the recessed part is aligned to the outer resonator. A schematic of the sample package is shown in Figure 4.6. To allow optical access for the fiber interferometric read-out, a hole is etched in the center of the recessed area. Since we are only interested in the general behaviour of this sample, we have performed the measurements at room temperature and ambient pressure without any vibration isolation.

To control the motion of the outer resonator, we apply a voltage across the two coated surfaces via wires attached at the edge of the wafers¹. Since the force depends quadratically on the voltage, it is always attractive. Applying a DC voltage would only pull on the resonator and an AC voltage would result in a force at twice the chosen frequency. When the applied voltage is a sum of these voltages, $V = V_{DC} + V_{AC} \cos(\omega t)$, the force on the resonator contains a cross-term that is linear in V_{DC} and at the same frequency as the applied AC voltage:

$$F_c = \frac{\varepsilon_0 A}{2d^2} \left[\left(V_{DC}^2 + \frac{1}{2} V_{AC}^2 \right) + 2V_{DC} V_{AC} \cos(\omega t) + \frac{1}{2} V_{AC}^2 \cos(2\omega t) \right]. \quad (4.5)$$

¹Only the recessed part of the silicon wafer was electrically connected.

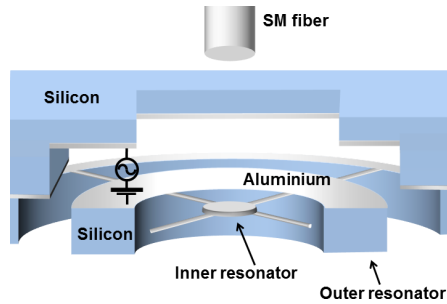


Figure 4.6: Schematic of the sample package allowing capacitive control of the outer resonator. The nested resonator is coated with a conductive aluminium layer. An aluminium coated silicon wafer is pressed against the resonator wafer. Part of the silicon wafer is recessed to prevent direct contact between the coating layers. A single mode (SM) fiber and hole for optical access are also indicated.

We verify whether this force can indeed be used to drive the outer resonator by looking at the response of the system to the 1f-component of the force, the second term on the RHS in Eq. 4.5. The DC voltage and the amplitude of the AC voltage are both set to 1 V, while the frequency of the AC voltage is scanned across the resonance frequency of 940 Hz. The signal from the fiber interferometer at each frequency step is detected and demodulated by a lock-in amplifier. The signal can be converted to nanometers by a separately performed calibration of the interferometer signal. The result is shown in Figure 4.7. For comparison the red line in the same figure shows the thermal motion of the resonator at room temperature obtained from a Fourier transform of the detector signal without drive.

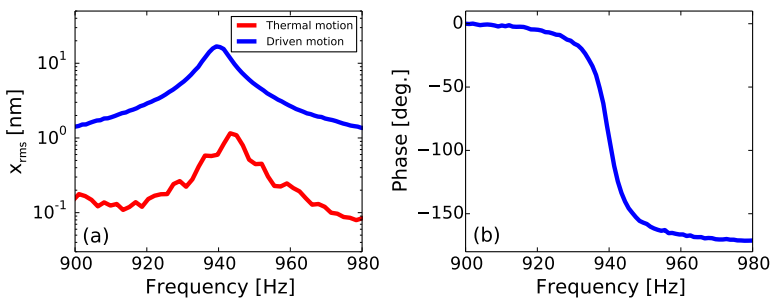


Figure 4.7: Frequency scan of the response of the outer resonator to the capacitive force: (a) Amplitude of the resonator motion (blue line) compared to the undriven thermal motion (red line); (b) Phase of the driven resonator motion.

It is clear that the capacitive drive of the outer resonator works and can easily increase the resonator motion by more than an order of magnitude. So it should in principle be possible to create a feedback loop to damp the motion, instead of

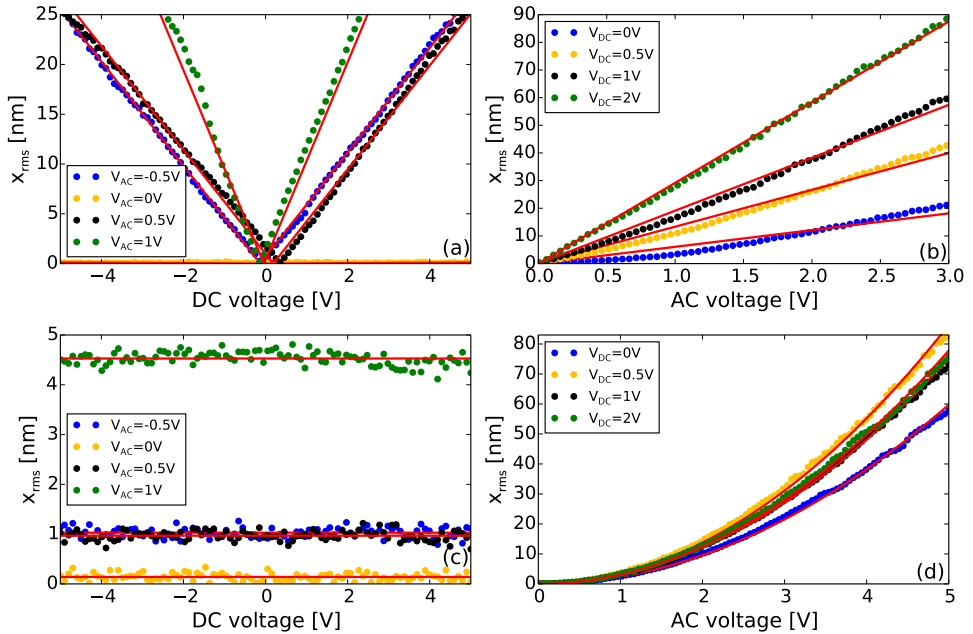


Figure 4.8: Scans of the (a,c) DC and (b,d) AC voltage while monitoring the response (a,b) at the applied frequency and (c,d) at twice the applied frequency. The points show data while the red lines show fits of the expected response.

driving it. But before we investigate this further, we want to be sure that the system responds as expected. We therefore performed sweeps of the DC and AC voltages while monitoring the 1f- and 2f-components of the force response (the second and third terms in Equation 4.5 respectively).

When the AC voltage is applied at the resonance frequency, with the signal demodulated at the same frequency, the response should be linear in both V_{AC} and V_{DC} . Figures 4.8(a) and 4.8(b) demonstrate indeed roughly a linear increase in resonator motion. Note that since we measure the RMS motion, the response is also positive at negative voltages.

When we apply the AC voltage at half the resonance frequency, we still expect response at the resonance frequency due to the third term in Equation 4.5. This term is independent of the DC voltage, as indeed shown in Figure 4.8(c). The average RMS motion increases with AC voltage, which we expect, and Figure 4.8(d) shows that this response is indeed quadratic.

In general, the voltage sweep show the expected trends. However, the linear response shows some small deviations. Figure 4.8(a) shows a tiny offset in DC voltage where the response is minimal, which should be at zero voltage. This is due to a small background voltage caused by a difference in work function between the two aluminium coatings.

A closer look at the linear response in Figure 4.8(b) shows some nonlinear be-

haviour. This deviation may be caused by measurement imprecisions, but it is also likely that other aluminium coated areas in the vicinity of the outer resonator form stray capacitors, which influence the resonator response.

Preventing the formation of stray capacitors is challenging, since it depends on a combination of sample fabrication techniques and manually aligning the two wafers. Minimizing the effect of unwanted capacitors generally also lowers the capacitance used to control the outer resonator. The aligning process is already quite cumbersome and requires a sample mount flexible enough for manipulation while being able to fix the wafers when aligned. Another disadvantage of the capacitive drive is that coating the nested resonator with a conductive aluminium layer is likely to negatively affect the mechanical quality factor of the inner resonator. So investigating another method for controlling the outer resonator motion seems beneficial.

But before we completely switch to another method, we use the constructed sample to demonstrate the amount of mechanical isolation it provides. The amount of isolation is proportional to the transferred energy, which again is proportional to the squared amplitude of the outer resonator motion [94], which we can measure directly. We drive the outer resonator capacitatively with a DC voltage of -2 V and an AC voltage amplitude of 1 V. The frequency of the drive is swept between 100 Hz and 100 kHz, and the interferometer signal, demodulated at the drive frequency, is squared. This method is similar to the measurement already shown in Figure 4.7. The resulting transfer function, normalized to one at low frequencies, is given in Figure 4.9. The blue points are the results from the sweep, while the red line is a fit with the theoretical transfer function. The resonances at frequencies above 10 kHz are caused by other vibrational modes of the nested resonator.

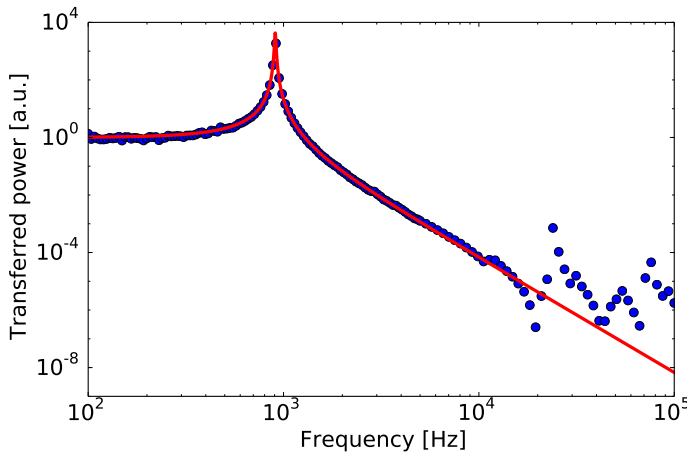


Figure 4.9: Frequency scan of the outer resonator motion (blue dots), converted to the power transferred by the outer resonator. This indicates the amount of vibrational isolation provided by the outer resonator. From the fit to the expected transfer function (red line) we can deduce an isolation of 40 dB/decade, resulting in an expected isolation of 80 dB at the inner resonance frequency of around 300 kHz.

From the slope of the transfer function above resonance we can infer a mechanical isolation of 40 dB/decade. Since the resonance frequency of the outer resonator is designed to be two orders of magnitude below that of the inner resonator, the mechanical isolation at the inner resonator frequency is expected to be 80 dB. Because of this large isolation, the motion of the resonator at the inner resonator frequency was no longer distinguishable with the sensitivity of the fiber interferometer, so the 80 dB of isolation could not be measured directly. It is clear, however, that the outer resonator provides significant isolation.

4.3.2 Dielectric force control of the resonator motion

An electric field induces polarization in a dielectric material. The formed dipoles are then attracted towards the point of maximum field strength. If the electric field is homogeneous, the dipoles are attracted equally to the positive and negative electrode and the net effect is zero. In order to create a force to attract the resonator, a strong gradient in the electric field is needed. If we describe the whole dielectric by a single dipole \mathbf{p} , the force on it is given by [95]:

$$\mathbf{F}_d = (\mathbf{p} \cdot \nabla)\mathbf{E}. \quad (4.6)$$

In our system the dielectric is the silicon outer resonator attracted to a $100\ \mu\text{m}$ diameter wire positioned in the vicinity. The other electrode is the copper sample mount located far from the resonator, such that the electric field is strongest near the wire. All the data showed in this section are obtained with this wire in the vicinity. However, it turned out that a wire pulls unevenly on the resonator, so in later designs we replaced the wire by a ring electrode with a diameter of $600\ \mu\text{m}$. The relative positions of the ring electrode, SM fiber and nested resonator are indicated in Figure 4.10. The dotted lines represent the electric field lines between the ring electrode and sample mount.

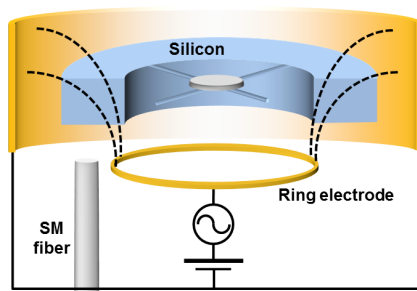


Figure 4.10: Schematic of the the nested resonator surrounded by the sample mount which is electrically connected to a ring electrode positioned near the outer resonator. A single mode (SM) fiber points towards the outer resonator for read-out of its motion. The electric field lines between the ring electrode and sample mount are indicated by the dotted lines.

If we set the direction of the field lines near the ring electrode and through the resonator in the z -direction and ignore the contribution of other directions, the force is equal to

$$F_{d,z} = \varepsilon_0 \chi_e E_z \frac{\partial E_z}{\partial z}, \quad (4.7)$$

with the outer resonator polarized in the z -direction, $p_z = \varepsilon_0 \chi_e E_z$ with χ_e the electric susceptibility of the silicon. The electric field distribution is not trivial and we are ultimately not interested in the exact magnitude of the force. So we further simplify the expression above by observing that the electric field (and its derivative) between the two electrodes is proportional to the applied voltage. It follows that the force depends quadratically on the voltage, just as in the case of a capacitive drive. We can therefore repeat the measurements presented in the previous section by applying similar voltages, namely the sum of a DC voltage to polarize the outer resonator and an AC modulation to influence its motion. The force is then proportional to

$$F_{d,z} \propto [V_{\text{DC}} + V_{\text{AC}} \cos(\omega t)]^2 = \left(V_{\text{DC}}^2 + \frac{1}{2} V_{\text{AC}}^2 \right) + 2V_{\text{DC}} V_{\text{AC}} \cos(\omega t) + \frac{1}{2} V_{\text{AC}}^2 \cos(2\omega t). \quad (4.8)$$

Similar to the result in Figure 4.7 we first check that we can drive the outer resonator by sweeping the AC voltage across the outer resonator frequency, while demodulating the interferometric read-out signal at the same frequency as the drive. Significantly higher voltages are needed than with the capacitive drive: the DC voltage is set to -40 V and the AC amplitude is 8 V. Again, the driven motion in Figure 4.11 is compared to the undriven thermal motion obtained from a Fourier transform of the interferometer signal.

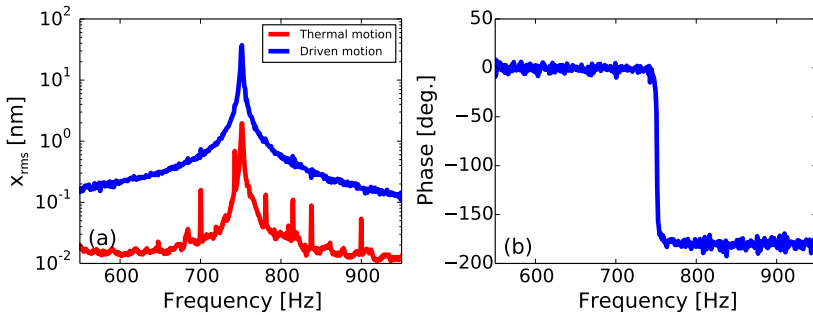


Figure 4.11: Frequency scan of the response of the outer resonator to the dielectric force: (a) Amplitude of the resonator motion (blue line) compared to the undriven thermal motion (red line); (b) Phase of the driven resonator motion.

The outer resonator clearly reacts to the dielectric force, its amplitude increases by more than an order of magnitude. This is a similar response to that observed with the capacitive drive. However, the sample preparation is more convenient, since it only requires positioning a SM fiber and an electrode in the vicinity of the outer resonator. Another disadvantage of the capacitive control was the presence

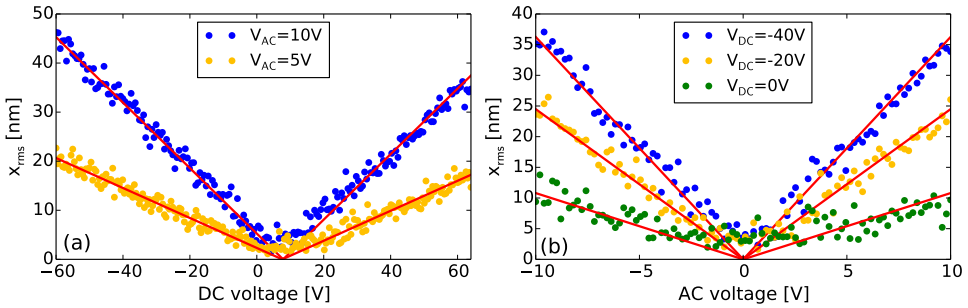


Figure 4.12: Sweeps of the (a) DC and (b) AC voltage while monitoring the response at the applied frequency. The red lines are fits of the expected response through the data points.

of spurious capacitors, influencing the linear response of the resonator on the voltage sweeps in Figure 4.8. These sweeps are repeated in Figure 4.12 with the dielectric drive. The response is now clearly linear, which means that the dielectric force as described by Eq. 4.7 is the only source that drives the resonator and that we can safely create a feedback loop that minimizes the resonator motion without being affected by other effects.

In such a feedback loop the phase-shifted interferometer signal is send back to the positive electrode with an adjustable gain. If the feedback is set correctly, the damping rate of the outer resonator should increase with loop gain. This is verified via amplitude ring-down measurements, where the resonator was first driven to a certain high amplitude before the feedback was switched on. The amplitude of

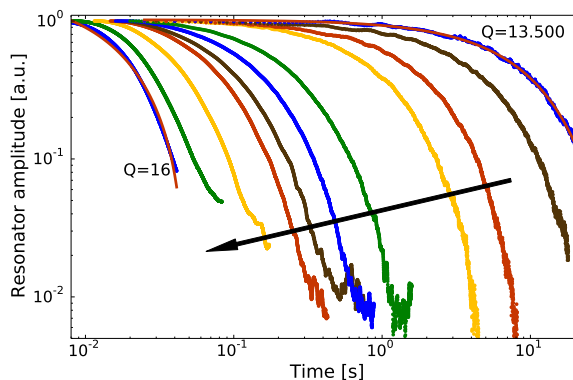


Figure 4.13: Resonator amplitude ring-down measurements with different loop gain. The arrow indicates the direction of increasing gain and, related, increasing damping rate of the outer resonator. From exponential decay fits (red lines, only shown for the outermost ring-downs) the mechanical quality factor is determined.

the outer resonator was measured as a function of time and followed an exponential decay. The quality factor is determined from the time constant. The ring-down measurements are displayed in Figure 4.13 for different values of the loop gain, with increasing gain indicated by the arrow.

With this method, the quality factor of the outer resonator is decreased significantly. Figure 4.13 shows that the quality factor, which starts at 13.500 without feedback, can be reduced to 16. This helps significantly in controlling the outer resonator motion. Even when external vibrations drive the outer resonator, which is likely to happen when the system is placed in a cryostat, this damping system is capable of damping the resonator motion to manageable amplitudes.

4.4 Conclusions and outlook

Adding a resonator around the original trampoline resonator is a good solution to prevent high-frequency vibrational noise from coupling to the trampoline resonator motion. As the single resonator is cooled optically, its signal becomes concealed by these vibrational noise peaks, which limits the achievable observable optical cooling factor. With the nested resonator, the resonator can be cooled further, reaching an effective temperature of 23 mK from room temperature before the signal disappears under the measurement noise floor.

But adding the outer resonator is not solely beneficial. Its mechanical properties influence the stability of the system, making it very sensitive to low-frequency vibrational noise. To damp this motion, two methods of applying a force were investigated: capacitively and dielectrically. Both methods are successful in driving the outer resonator motion and can also be used to damp it. However, using the dielectric force profits from an easier set-up design.

With our control of the outer resonator motion, we have added the possibility to not only lock the laser frequency to follow changes in the cavity length, but also to adjust the cavity length to follow the laser frequency [96]. Instead of letting the laser be influenced by the vibrational noise, the length variations are now eliminated by actively stabilizing the position of the nested resonator.

The mechanical quality factor determines the optical cooling factor that can be achieved before the signal disappears in the background. With the current optical cooling factor, it should in principle be possible to achieve a phonon occupancy of less than one starting at a base temperature of 100 mK. Placing the set-up in a dilution refrigerator is therefore the next logical step.

PART II

Casimir effect

Thermal Casimir Force and Superconductors

The van der Waals force is carried by virtual photons that are exchanged by two interacting atoms or molecules. As their separation increases, the interaction is no longer instantaneous due to the finite speed of light. The result is a faster decay of the force with distance. Two macroscopic conducting plates at small separation are attracted to each other by the van der Waals interactions of the individual atoms, although the interactions cannot simply be added pairwise and one has to correct for the presence of the other atoms. When the plate separation becomes larger, one has to account again for the retardation of the interaction photons. This retarded van der Waals force between macroscopic bodies is better known as the Casimir force. The retarded van der Waals force is one interpretation of the origin of the Casimir force and several other methods exist to calculate this force [36]. One of these methods will be explored in this chapter.

In 1948, Hendrik Casimir calculated the interaction between two parallel plates due to the existence of the vacuum fluctuations of the electromagnetic field [37]. In his approach he considered perfectly reflecting, uncharged and nonmagnetic plates, having a reflectivity equal to one at all frequencies. Lifshitz later found that for real materials the force is determined by the values of the complex dielectric constant of the media involved [97]. However, one needs to know these values at all frequencies to compute the force. And this poses problems, since experimental characterization of the material is currently only accessible at certain frequency ranges. Extrapolating the data to all frequencies is possible via two different models. One model, the Drude model, accounts for frictional dissipation in the material, while in the other model, the plasma model, dissipation is not included. At room temperature, the difference appears only at the DC contribution to the Casimir force. To this day there remains controversy on which model is more appropriate.

Although the Casimir force is determined by the dielectric permittivity at all frequencies, not all frequency ranges contribute equally. It is possible to set the measurement conditions in a way that especially the low frequencies contribute, such

that the difference between the models is most distinct. One solution is to measure the Casimir force at larger distances [50]. However, these measurements seem to conflict with precision measurements at smaller distances [11]. So measurements of this type have not given a decisive answer yet. Another solution is to measure the Casimir force at higher temperatures, but this is limited by experimental requirements, such as the maximum working temperature of piezo-electric transducers.

The solution we will explore is the use of superconducting materials [49]. Superconductors repel a static magnetic field due to the Meissner effect. Below the critical temperature, the contribution of this field to the total Casimir force is therefore known and can be used as a reference when the material is brought into a non-superconducting state.

In this chapter we will give the theoretical background of the Casimir force between real conductors. Since accurate derivations can be found in literature [36, 97, 98], we will only outline the main steps and focus on the important components. The influence of the models is shown and how the difference becomes apparent at larger distances and higher temperature. Finally we will introduce a simple model for the Casimir force between superconductors

5.1 Casimir force between perfect conductors

There are several ways to find an expression for the Casimir force between two parallel plates [36, 98–101]. Some of these methods calculate the electromagnetic modes that can exist between the plates and assign to each mode a zero-point energy $E_0 = \frac{1}{2}\hbar\omega$, with \hbar the reduced Planck constant and $\omega = ck$ the angular frequency of the mode, with c the speed of light and k the wave vector. The total Casimir energy of the system can then be approached as the sum over all modes between the plates, minus the continuum of modes outside the plates:

$$E_C = \sum_{\omega} \frac{1}{2}\hbar\omega - \int \frac{\hbar c}{2} k \, dk. \quad (5.1)$$

At first glance, this seems to result in an infinite energy. It is however reasonable to set a cut-off frequency that corresponds to a wavelength smaller than the size of the atoms of the plates. For waves at these frequencies, the plates form no obstacle and their zero-point energy is not influenced.

In his original paper [37] Casimir assumed that the plates are made of perfect conductors. Perfect conductivity means that the reflection coefficient of the plates is equal to plus or minus one (depending on the polarization). The possible waves in the direction normal to the plates therefore have wave numbers $k_z = \frac{\pi}{d}n_z$, with d the plate separation. For infinite plates the parallel wave vectors, k_x and k_y , are continuous, and so is k_z when the plate separation is infinite. Casimir calculated the energy difference between plates at infinite and finite separation and derived from that the following expression for the force per area A

$$F_C = -\frac{\pi^2\hbar c A}{240d^4}. \quad (5.2)$$

An interpretation of this force is that the discrete number of modes between the plates exert less radiation pressure than the continuous spectrum of modes outside the plates.

5.2 Lifshitz theory for the force between real conductors

The calculations to obtain the Casimir force become more elaborated when we no longer assume perfect reflectors. In this section we will outline the steps followed by Lifshitz to find an expression for the Casimir force. We will comment on its limitations and how they can be circumvented.

For real conductors, the boundary conditions of the plates are related to the complex dielectric permittivity

$$\varepsilon(\omega) = \varepsilon'(\omega) + i\varepsilon''(\omega), \quad (5.3)$$

where $\varepsilon'(\omega)$ accounts for the dispersion in the material and $\varepsilon''(\omega)$ for the absorption.

Furthermore, at finite temperatures T , the interacting photons have a distribution not only given by the zero-point fluctuations, but also by their Bose-Einstein statistics, with the number of photons in a mode with frequency ω given by

$$n(\omega) = \frac{1}{2} + \frac{1}{e^{\hbar\omega/k_B T} - 1} = \frac{1}{2} \coth \frac{\hbar\omega}{2k_B T}, \quad (5.4)$$

with k_B Boltzmann's constant. Note that the presence of these finite temperature fluctuations is directly linked to the absorption term $\varepsilon''(\omega)$ in the dielectric permittivity by the fluctuation-dissipation theorem. Absorption of radiation in the plates transforms the radiation energy into heat, which in turn causes thermal fluctuations in the plates.

Consider now two half spaces filled with two media (representing the parallel plates) separated by a distance d . This situation is depicted in Figure 5.1, where we have indicated the dielectric permittivities of the media with ε_1 and ε_2 , these materials are taken to be nonmagnetic. Since in our measurements the space between the two plates is vacuum, we set $\varepsilon_3 = 1$. It is of course possible to extend the calculations by filling this space with some other medium (gas or fluid), which would alter the strength of the Casimir force, or even change its sign from attractive to repulsive [102–104].

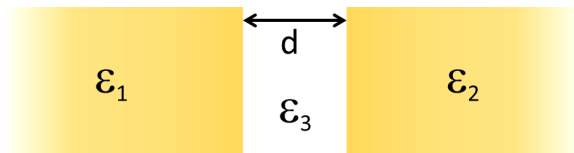


Figure 5.1: The parallel plates can be represented as two half spaces filled with media 1 and 2, separated by a distance d . The space in between (medium 3) is vacuum.

The force is derived [97] from the electric and magnetic fields between the plates, which in turn can be found by solving Maxwell's equations with the appropriate boundary conditions. For monochromatic electric and magnetic fields, in the form $\mathbf{E}_0 e^{-i\omega t}$ and $\mathbf{B}_0 e^{-i\omega t}$, we seek solutions of

$$\nabla \times \mathbf{E}_0 = i\frac{\omega}{c}\mathbf{B}_0, \quad (5.5)$$

$$\nabla \times \mathbf{B}_0 = -i\frac{\omega}{c}\varepsilon(\omega)\mathbf{E}_0 - i\frac{\omega}{c}\mathbf{K}. \quad (5.6)$$

An extra fluctuating, random field \mathbf{K} is added to account for the thermal and quantum fluctuations of the material's microscopic constituents [97, 105], and determined by its correlation function

$$\langle K_i(\mathbf{r})K_j(\mathbf{r}') \rangle = 2\hbar \coth\left(\frac{\hbar\omega}{2k_B T}\right) \varepsilon''(\omega)\delta_{ij}\delta(\mathbf{r} - \mathbf{r}'), \quad (5.7)$$

where the use of the δ -function means that the fluctuations are only locally correlated. We assume nonmagnetic materials, therefore only electric noise is added. This additional random field \mathbf{K} is zero in the vacuum between the plates.

Solutions of Maxwell's equations are found in the two media and in the vacuum between them after demanding continuity of the normal and tangential components of the fields and transversality of the waves. These solutions are given in momentum space in terms of the wave vector \mathbf{k} , where we separate the component perpendicular to the plane of the gap k_z from the tangential components \mathbf{k}_\parallel such that $k^2 = k_\parallel^2 + k_z^2$.

The Casimir force is derived from the zz -component of the Maxwell stress tensor, based only on the electric and magnetic fields in the vacuum between the plates. The fields in the plates still have influence on the force, because they shape the vacuum fields via the continuity conditions. The calculated fields are monochromatic, so the total force is obtained after an integration over all frequencies ω . The expressions for the fields contain another integration, over the tangential wave vector component \mathbf{k}_\parallel . To make the final expression more compact, this integration is transformed to an integration over a parameter p defined as

$$p = \sqrt{1 - \frac{c^2}{\omega^2}k_\parallel^2}. \quad (5.8)$$

The paths of integration for both p and ω are shown in Figure 5.2(a). The integration over ω is purely over the real axis, but the path of integration for p lies both on the real and imaginary axis, due to the integration over k_\parallel from zero to infinity. This means that part of the integration is along a path where both p and ω are real. This is problematic because the integrand contains an expression $e^{-2ip\omega d/c}$, which oscillates along this part, especially at large distances d . This can be solved by transforming the paths of integration via contour integration. Note that part of the contour is a semicircle with infinite radius, which does not depend on distance such that the contribution along this path goes to zero. The new paths of integration are depicted in Figure 5.2(b). The variable p is now purely real, but the frequencies ω have become purely imaginary.

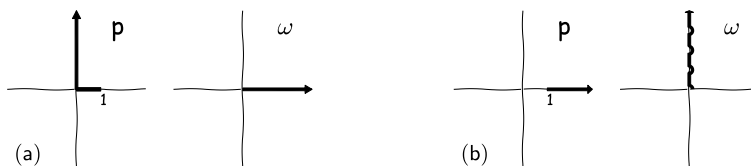


Figure 5.2: Integration paths for the integrals in the expression of the Casimir force: (a) As originally calculated, the integrand becomes highly oscillatory at the real part of the path of integration for p ; (b) After transformation of the integration paths, the integrand no longer oscillates but the integration over ω is now over purely imaginary values.

At zero temperature, we can then replace $\omega = i\xi$, with ξ real. At finite temperature, however, the integrand contains a term $\coth(\hbar\omega/2k_B T)$, which has poles along the imaginary frequency axis. According to Cauchy's residue theorem, the integral over the imaginary frequencies can be replaced by a sum over the residues at the poles. These poles are positioned at points where the argument of the cotangent is equal to a multiple of π , so at frequencies

$$\omega_n = i\xi_n = i\frac{2\pi k_B T}{\hbar}n, \quad (5.9)$$

with n an integer. These frequencies are known as the Matsubara frequencies. Note that because of the residue theorem only these frequencies contribute to the force.

The total force per unit area is therefore described by a sum over these Matsubara frequencies and an integral over the parameter p , which represents the tangential wave vector component:

$$P_C = -\frac{k_B T}{\pi c^3} \sum_{n=0}^{\infty} \int_1^{\infty} p^2 \xi_n^3 \left\{ \left[\frac{(s_1 + p)(s_2 + p)}{(s_1 - p)(s_2 - p)} e^{2p\xi_n d/c} - 1 \right]^{-1} + \left[\frac{(s_1 + \varepsilon_1 p)(s_2 + \varepsilon_2 p)}{(s_1 - \varepsilon_1 p)(s_2 - \varepsilon_2 p)} e^{2p\xi_n d/c} - 1 \right]^{-1} \right\} dp, \quad (5.10)$$

where $\varepsilon_j = \varepsilon_j(i\xi_n)$ and where the parameter $s_j = \sqrt{\varepsilon_j(i\xi_n) - 1 + p^2}$, with $j = 1, 2$, is introduced for compactness. The prime on the summation mark indicates that the $n = 0$ term is multiplied with an extra factor $\frac{1}{2}$. At zero frequency only half the residue is taken into the summation. Physically, this can be understood since zero-order modes only have one polarization while higher order modes have two polarizations.

This expression describes the Casimir force between two media 1 and 2 at nonzero temperature and holds for nonmagnetic media. For magnetic materials, the force can be derived with the magnetic permeability $\mu(\omega)$ included [102, 106, 107]. We will only consider nonmagnetic materials in this thesis. For spatially dispersive media, like superconductors, there is interaction among different parts of the system with a response that depends on their separation $\mathbf{r} - \mathbf{r}'$. In this situation the dielectric

permittivity is also influenced by contributions at this separation and depends, after a Fourier transform, on the wave vector: $\varepsilon = \varepsilon(\mathbf{k}, \omega)$ [108]. Note that the presence of the gap violates the translational invariance in the direction perpendicular to the plates required for the Fourier transform. It is therefore only a phenomenological approach to repeat the calculations leading to the Lifshitz expression while including the wave vector dependence [109], another possibility is to directly rewrite Eq. 5.10 in terms of the reflection coefficients of the plates [110]. If the parameters p and $s_{1,2}$ are written out, it is possible to recognize the Fresnel equations in Eq. 5.10. The full calculation is shown in Appendix A and leads to

$$P_C = -\frac{k_B T}{\pi} \sum_{n=0}^{\infty} \int_0^{\infty} q_n k_{\parallel} \left\{ \left[\left(r_{\text{TE}}^{(1)} r_{\text{TE}}^{(2)} \right)^{-1} e^{2q_n d} - 1 \right]^{-1} + \left[\left(r_{\text{TM}}^{(1)} r_{\text{TM}}^{(2)} \right)^{-1} e^{2q_n d} - 1 \right]^{-1} \right\} dk_{\parallel}, \quad (5.11)$$

where $q_n^2 = \frac{\xi_n^2}{c^2} + k_{\parallel}^2$ and $r_{\text{TE}}^{(1,2)}$ and $r_{\text{TM}}^{(1,2)}$ denote the reflection coefficients for the transverse electric and transverse magnetic modes respectively, the superscript indicates the corresponding medium. When the appropriate reflection coefficients are used, this equation for the Casimir force can also be used for spatially dispersive media.

5.3 Models for the dielectric permittivity

The Casimir force is determined by the reflectivity of the surfaces, which in turn depends on the dielectric permittivity of the materials. However, due to the transformation described in the previous section, the dielectric permittivity needs to be expressed in terms of imaginary frequencies. This expression is obtained via the Kramers-Kronig relation

$$\varepsilon(i\xi) = 1 + \frac{2}{\pi} \int_0^{\infty} \frac{\omega \varepsilon''(\omega)}{\omega^2 + \xi^2} d\omega. \quad (5.12)$$

The integration over all real frequencies means that full knowledge of the dielectric permittivity is necessary to compare experimental data with theoretical calculations. For high frequencies, such data can be obtained from optical measurements and tabulated optical data are available for several materials¹ [112]. For the low frequency range where the dielectric permittivity is not determined experimentally, the data has to be extrapolated. One model that can be used for extrapolation [113, 114] is the Drude model for electrical conduction [115, 116]:

$$\varepsilon_D(\omega) = 1 - \frac{\Omega_p^2}{\omega(\omega + i\gamma)}, \quad (5.13)$$

¹Note that the dielectric function depends on the sample preparation and therefore the best agreement between theory and experiment is achieved when the optical data is obtained from the actual sample that is used for the Casimir force measurements [111].

where Ω_p is the plasma frequency, which is given by

$$\Omega_p^2 = \frac{4\pi n_e e^2}{m^*} \quad (5.14)$$

with n_e the electron density, e the electron charge and m^* the effective mass of the electrons, and where γ is the relaxation frequency that accounts for Ohmic conductivity

$$\gamma = \frac{\Omega_p^2 \varepsilon_0}{\sigma_0}, \quad (5.15)$$

with σ_0 the static conductivity. It is therefore possible to obtain values for Ω_p and γ from measurements of the resistance in the material. The dielectric permittivity at imaginary frequencies according to the Drude model is given by

$$\varepsilon_D(i\xi) = 1 + \frac{\Omega_p^2}{\xi(\xi + \gamma)}, \quad (5.16)$$

which can be used if no extensive optical data are available. However, due to some theoretical discrepancies that have been argued, but also refuted [48, 117–123], some prefer to use the plasma model of infrared optics:

$$\varepsilon_p(\omega) = 1 - \frac{\Omega_p^2}{\omega^2}. \quad (5.17)$$

In this model the dielectric permittivity is purely real, therefore the model does not account for Ohmic dissipation. This is contradictory with the fact that metals are resistive at low frequencies and the use of the plasma model would seem incorrect, except that certain Casimir force experiments have shown better agreement with this model than with the Drude model [11, 52, 107, 124]. Since the plasma model is purely real, using it to extrapolate the imaginary dielectric permittivity is not feasible. A solution is to use the plasma model at imaginary frequencies,

$$\varepsilon_p(i\xi) = 1 + \frac{\Omega_p^2}{\xi^2}, \quad (5.18)$$

but this does not take the measured optical data into account. Optical spectra of real materials often contain extra resonances that are not modeled by the Drude and plasma models. These extra resonances are a result of a restoring force binding the core electrons to the nuclei [116]. To describe the optical spectrum including these resonances, the Drude model for metals is extended with Lorentz oscillators to the Drude-Lorentz model

$$\epsilon_{DL}(\omega) = 1 - \frac{\Omega_p^2}{\omega(\omega + i\gamma)} + \sum_j \frac{f_j}{\omega_{0j}^2 - \omega^2 - i\beta_j\omega}, \quad (5.19)$$

where each oscillator j is described by an oscillator strength f_j , oscillator frequency ω_{0j} and damping rate β_j . Values for these parameters are obtained from fits to the

optical spectra. The dielectric permittivity at imaginary frequencies is more correctly described by the Drude-Lorentz model

$$\varepsilon_{\text{DL}}(i\xi) = 1 + \frac{\Omega_p^2}{\xi(\xi + \gamma)} + \sum_j \frac{f_j}{\omega_{0j}^2 + \xi^2 + \beta_j \xi}, \quad (5.20)$$

or by the generalized plasma model [98]

$$\varepsilon_{\text{gp}}(i\xi) = 1 + \frac{\Omega_p^2}{\xi^2} + \sum_j \frac{f_j}{\omega_{0j}^2 + \xi^2 + \beta_j \xi}. \quad (5.21)$$

These models do account correctly for the resonances in the material, although resonances lying outside the range of the optical reflection measurements are not taken into account. In principle, the transformation of the optical data extrapolated via the Drude model to imaginary frequencies should result in the same dielectric permittivity as described by the Drude-Lorentz model. Note that by maintaining the resonances but setting $\gamma = 0$, the generalized plasma model does describe the relaxation of the core electrons, but not of the conduction electrons [98]. For the calculations presented in this chapter we use these Drude-Lorentz and generalized plasma models, although we may refer to them as the Drude and plasma models for simplicity.

To this day a controversy exists how to deal with the low frequency range of the dielectric permittivity. Both models can be used to calculate the Casimir force, such that comparison to precision measurements can give more insight in this issue. Figure 5.3 indicates how the dielectric permittivity of gold depends on the imaginary frequency ξ . Optical data are available [112] for frequencies higher than 1.9×10^{14} rad/s, for lower frequencies the dielectric permittivity is computed according to the Drude-Lorentz and generalized plasma models and the values $\Omega_p = 9.0$ eV and $\gamma = 35$ meV [114]. The deviation between the two models is clearly visible.

At finite temperature, the Casimir force is computed only at a finite set of frequencies, the Matsubara frequencies, since the contribution at other frequencies goes to zero². It turns out that at room temperature, all except the zero-order frequency lie above 1.9×10^{14} rad/s, the lowest frequency at which optical data is available, the position of $\xi_1 = 2.4 \times 10^{14}$ rad/s is indicated in Figure 5.3. This means that the contribution of these frequencies can not reveal a difference between the Drude and plasma models. The difference only shows up in the zero-order Matsubara frequency, which represents a static field. Because the expressions for the dielectric permittivities diverge at zero frequency, we will continue our discussion in terms of the reflection coefficients mentioned in Eq. 5.11. The reflection coefficients are different for the TM and TE modes, which, at zero frequency, represent a static electric and static magnetic field respectively. The reflection coefficient can be determined by substituting the dielectric permittivities into the Fresnel equations (the expressions are given in Appendix A). For the zeroth order TM mode, which has only electric fields in the direction of propagation, the reflection coefficient becomes

$$r_{\text{TM}}^{(D,p)}(\xi_0) = 1. \quad (5.22)$$

²Although the theory is developed at finite temperature, it is important to note that the problem how to extrapolate the dielectric permittivity to lower frequencies is not temperature dependent and also occurs at zero temperature.

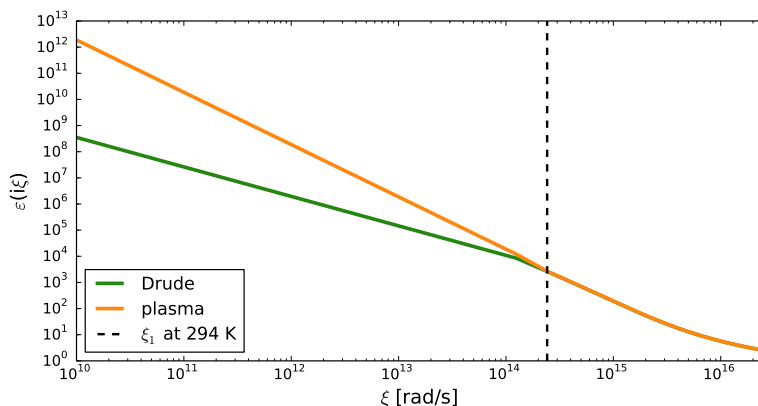


Figure 5.3: Dielectric permittivity of gold at imaginary frequencies $i\xi$ as a function of ξ . For frequencies above 1.9×10^{14} rad/s optical data are available, the extrapolation to lower frequencies was obtained with the values $\Omega_p = 9.0$ eV and $\gamma = 0.035$ eV. It is clear that the Drude and plasma models deviate at lower frequencies. The first order Matsubara frequency at room temperature is also indicated.

Note that this does not depend on the material and is also independent of temperature. More importantly, both Drude and plasma models predict the same coefficient. Physically, this value also makes sense, since metals reflect static electric fields.

The remaining term is the reflection coefficient of the static magnetic field, the zeroth order TE mode. This does have a different value for each model. The Drude model predicts

$$r_{\text{TE}}^{(D)}(\xi_0) = 0, \quad (5.23)$$

which physically can be understood since nonmagnetic materials form no obstacles for static magnetic fields. When substituted into the Lifshitz expression, this term results in a zero contribution to the Casimir force. This value is independent of Ω_p and γ and is purely a consequence of this model. According to the Drude model, therefore, only the static electric term contributes to the force at zero frequency.

The plasma model predicts a different coefficient:

$$r_{\text{TE}}^{(p)}(\xi_0) = \frac{k_{\parallel}c - \sqrt{k_{\parallel}^2c^2 + \Omega_p^2}}{k_{\parallel}c + \sqrt{k_{\parallel}^2c^2 + \Omega_p^2}}. \quad (5.24)$$

This leads to a nonzero contribution to the Casimir force, which is somewhat smaller than the contribution of the zeroth order TM mode. For large distances, $d \gg \frac{c}{2\Omega_p}$, and large temperatures the contribution approximates to the value at the zeroth order TM mode, which makes the total zeroth order contribution of the plasma model twice as large as the Drude model in this limit.

5.4 The effect of the different models on the Casimir force

Since a controversy exists on how to deal with the low frequency contribution of the dielectric permittivity to the Casimir force, experimental data are necessary to give a final verdict. Since only the zeroth order TE mode differs for both models, it is important to minimize the effect of the higher order modes. If we take a closer look at Eq. 5.11, we notice the factors

$$e^{-2q_n d} = e^{-2\sqrt{\xi_n^2/c^2 + k_{\parallel}^2} d}. \quad (5.25)$$

The result of this term is that the Casimir force quickly reduces with distance and with ξ_n . Recall that the Casimir force is a sum of the contributions at the Matsubara frequencies. For larger distances, less Matsubara frequencies contribute to the force. This influence is visualized in Figure 5.4. The Casimir pressure as a function of distance, for two gold coated plates at room temperature, is shown in Figure 5.4(a). The difference between the two models only becomes visible at distances approaching $1 \mu\text{m}$ or larger. The Matsubara frequencies that contribute to the force are shown in Figures 5.4(b) and 5.4(c), for a distance of 100 nm and $1 \mu\text{m}$ respectively. Note that the contributions of both models overlap for the frequencies ξ_n with $n > 0$. At a distance of 100 nm , many frequencies have to be considered, whereas at $1 \mu\text{m}$ only the input of the first couple of frequencies is significant. Therefore, the relative contribution of the zeroth order Matsubara frequency is larger and the effect of the zeroth order TE mode is more likely to be detected.

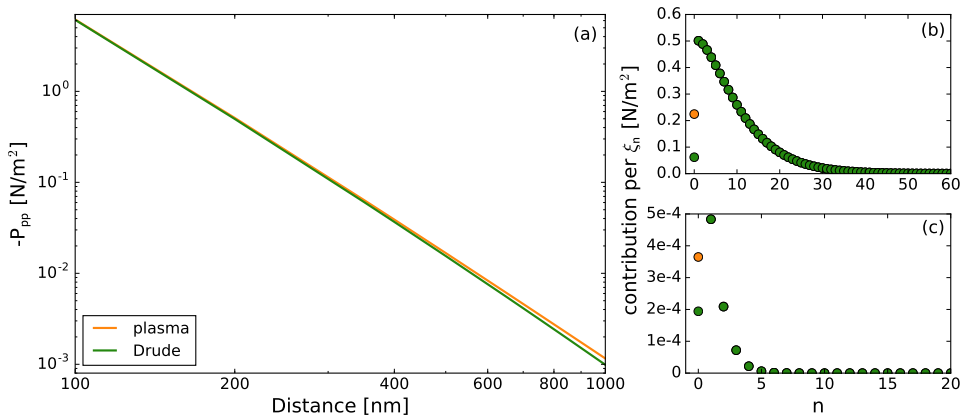


Figure 5.4: Distance dependence: (a) Casimir pressure as a function of distance at room temperature, the two models give diverging contributions only at larger distances; (b) Contribution of the different Matsubara frequencies for the two models at a distance of 100 nm ; (c) At a distance of $1 \mu\text{m}$ less Matsubara frequencies contribute to the force.

There is a lot of interest to resolve the difference between the models via precise

measurements at large distances [11, 47, 50, 98]. But since the Casimir force reduces rapidly with distance, the signal quickly becomes too small to detect. So far, measurements of the distance dependence of the force have not resulted in a conclusive answer yet.

Another approach may be more successful. Since the Matsubara frequencies depend linearly on temperature, raising the temperature has a similar effect as increasing the distance without reducing the force. Measurements of the Casimir force at higher temperatures therefore should also show the difference between the two models [125]. In Figure 5.5(a) we have plotted the temperature dependence of the Casimir force for the two models. The distance between the plates is set at 100 nm, where the force can easily be detected.

While evaluating the temperature dependence, we must be careful to note that not only the force itself is a function of temperature (due to the interacting thermal photons), but that also the dielectric permittivity as described by the Drude model changes with temperature. The relaxation frequency γ is temperature dependent because it is related to the conductance of the material. If no impurities are present, the material's resistivity can be described with the Bloch-Grüneisen formula, such that for gold [48]

$$\gamma(T) = 0.087 \left(\frac{T}{\Theta} \right)^5 \int_0^{\Theta/T} \frac{x^5 e^x}{(e^x - 1)^2} dx, \quad (5.26)$$

with $\Theta = 175$ K the Debye temperature for gold. Of course, this is only a model. It would be better to use measurements of the dielectric permittivity of the material at all temperatures of interest. Since these data are only sporadically available, we have to revert to the model. The temperature-dependent dielectric permittivity is calculated using a plasma frequency of $\Omega_p = 9.0$ eV and a relaxation frequency given by Eq. 5.26. Note that compared to the dielectric permittivity obtained from optical reflection measurements this model underestimates the permittivity at higher frequencies. For comparison, the graph in Figure 5.5(a) shows two calculations for the Drude model, one based on the optical data of gold with the relaxation frequency kept constant at the room temperature value of 35 meV (green line) and one with the permittivity calculated via the model only (yellow line). Note that since the model underestimates the permittivity, the Casimir force is also estimated lower than in reality. Without the availability of optical data at a large temperature range, we will continue our calculations with the temperature-independent relaxation frequency.

The relative difference between the two models, normalized to the plasma model, is shown in Figure 5.5(b). As expected, the difference increases with temperature. A significant difference, of more than a few percent, arises at temperatures above 1000 K, which is technically unrealistic to achieve. This requirement can be relieved by using a combination of larger distance and a temperature lower than 1000 K, but higher than room temperature. At a distance of 400 nm, there is a significant difference of more than 10 percent at a temperature of 600 K. The effect might also be investigated by varying the temperature over a large range. Figure 5.5(a) shows that in the plasma model, the Casimir force is monotonically increasing with temperature, while the Drude model predicts a slight decrease in a certain temperature

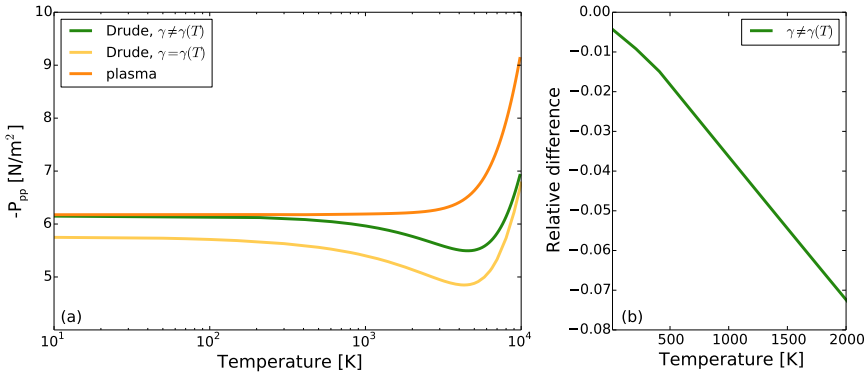


Figure 5.5: Temperature dependence of the Casimir force, for a distance of 100 nm between the plates: (a) At higher temperatures the two models diverge. The green line shows the influence of the Drude model with γ kept at the room temperature value of 35 meV, while for the yellow line the relaxation rate is calculated according to Eq. 5.26; (b) Difference between the Drude and plasma models, normalized to the plasma model, for the temperature independent dielectric permittivity.

range. From a temperature scan at a fixed distance, the model can be deduced from the sign of the force's rate of change. This does, however, require a large achievable temperature range.

So, by increasing the distance or the temperature the influence of higher order Matsubara frequencies is decreased, and therefore the relative influence of the zeroth order modes is increased. This allows investigation of the effect of these terms at the cost of the necessity of very accurate measurements.

5.5 Casimir force between superconductors

There is another approach to specifically investigate the effect of the zeroth order TE mode. Recalling that this mode represents a static magnetic field, and that superconductors expel such a field, measuring the Casimir force between superconductors is a logical and more direct step to approach the issue [49, 55, 126]. A disadvantage of using superconductors is that measurements can only be performed at low temperatures, where the amount of higher order frequencies contributing to the force is increased significantly compared to room temperature. This lessens the relative effect of the zero-order frequency.

Just as with normal conductors, to calculate the Casimir force between superconductors full knowledge of the dielectric permittivity of the material is required. There are several models describing the conductivity of superconductors, from which the dielectric permittivity at imaginary frequencies can be deduced. Two of these models will be discussed below. Both models operate in the local limit, where the dielectric permittivity only depends on the frequency and not on the wave vector or on

position. A model for the dielectric permittivity in the non-local limit, which would be more correct for spatially dispersive superconductors, can be deduced from Ref. [127].

The macroscopic two-fluid model [128] describes superconductivity on the basis of thermodynamics. It states that only part of the conduction electrons contribute to the supercurrent, while the other conduction electrons remain normal. The core electrons remain unaltered, their contribution to the dielectric permittivity is described by the Lorentz oscillations. The superconducting electrons have no dissipation, so they are best described by the plasma model. For the normal electrons it is generally accepted that they are dissipative and can therefore be described by the Drude model. We will first follow this description, later in this section we will explain the results if we apply the plasma model description for the normal electrons as well. The ratio of superconducting electrons to normal electrons is temperature dependent and follows the Gorter-Casimir order parameter $\eta(T)$:

$$\eta(T) = \left[1 - \left(\frac{T}{T_c} \right)^4 \right] \Theta(T_c - T), \quad (5.27)$$

$$\Theta(x) = \begin{cases} 0, & x < 0 \\ 1, & x \geq 0 \end{cases}$$

Above the critical temperature there are no superconducting electrons, which is ensured in the model by the Heaviside step function $\Theta(x)$. The conductivity of a superconductor, and therefore its dielectric permittivity, is a sum of the supercurrent permittivity and the permittivity of the normal electrons [129], with the Lorentz oscillators also included:

$$\epsilon_{2F}(i\xi) = 1 + \frac{\Omega_p^2}{\xi^2} \eta(T) + \frac{\Omega_p^2}{\xi(\xi + \gamma)} (1 - \eta(T)) + \sum_j \frac{f_j}{\omega_{0j}^2 + \xi^2 + \beta_j \xi}, \quad (5.28)$$

where Ω_p and γ are the plasma and relaxation frequencies of the superconducting material in the normal state. Note that due to the character of the order parameter, the permittivity behaves plasma-like at zero temperature and Drude-like close to the critical temperature. As the temperature decreases, more electrons contribute to the supercurrent and the system is less influenced by Ohmic dissipation. Since the two-fluid model assumes that the normal electrons in the superconductor are described by the Drude model, this assumption should be continued above the critical temperature in order to warrant a continuous transition across the critical temperature. The Casimir force gradually changes from the value predicted by the Drude model above the critical temperature to a value predicted by the plasma model as the temperature approaches 0 K. For simplicity, we will call the combination of the two-fluid model for superconductors and the Drude model for the normal state, including the Lorentz oscillators, the Drude-two-fluid model.

In the plasma model description, the situation is different. The normal electrons above the critical temperature are described by the generalized plasma model. Below the critical temperature the resistivity of the normal electrons would not change, such that in the superconductor both the normal electrons and the superconducting

electrons follow the plasma model. The change in their ratio with temperature therefore does not alter the dielectric permittivity of the material and the superconducting transition has no effect at all on the Casimir force. In the following, we will refer to the two-fluid model combined with the generalized plasma model description for the normal electrons simply as the plasma model.

The absence or presence of an effect of the superconducting transition is directly measurable as the temperature is changed across the critical temperature. Since it is a relative measurement, it requires a less strict calibration of the set-up than with measurements at large distances. Compared to the high temperature measurements, it has the advantage of a relative small temperature change between 0 K and the critical temperature. In this chapter we will estimate the magnitude of the change in the Casimir force, measurements of the force will be discussed in chapter 8.

To arrive at an expression for the Casimir force, we can follow the same procedure as with normal conductors. The expression is given by Eq. 5.11, where the reflectivity of the superconductor is deduced via the Fresnel equations. The zero-order terms are based on a reflectivity of one for the TM mode for both the Drude-two-fluid model and the plasma model. As with normal conductors, the static electric field is repelled. The reflectivity of the zero order TE mode in the plasma model is the same as given by Eq. 5.24, in the Drude-two-fluid model we insert the two-fluid dielectric permittivity at imaginary frequencies in the Fresnel equations and then take the limit $\xi \rightarrow 0$, the resulting term is given by

$$r_{\text{TE}}^{(2\text{F})}(\xi_0) = \frac{k_{\parallel} - \sqrt{k_{\parallel}^2 + \eta(T)\Omega_p^2/c^2}}{k_{\parallel} + \sqrt{k_{\parallel}^2 + \eta(T)\Omega_p^2/c^2}}. \quad (5.29)$$

At $T = T_c$, this correctly leads to the Drude reflectivity $r_{\text{TE}}^{(D)} = 0$, while at $T \ll T_c$ the plasma zero-order reflectivity is recovered. Note that for ideal metals ($\Omega_p \rightarrow \infty$) the plasma zero-order reflectivity goes to -1 , i.e. perfect reflection of the static magnetic field due to the Meissner effect.

The two-fluid model is only a phenomenological model, a more complete description for superconductors is given by the microscopic BCS-theory [130, 131]. From the current density in a superconductor [132], it is possible to deduce the conductivity [133]:

$$\sigma(\omega) = -i \frac{2n_e e^2 \gamma}{m^* \omega} \int_{-\infty}^{\infty} \int_{-\infty}^{\infty} \left\{ L(\omega, \epsilon, \epsilon') - \frac{f(\epsilon) - f(\epsilon')}{\epsilon' - \epsilon} \right\} \frac{1}{(\epsilon' - \epsilon)^2 + \gamma^2} d\epsilon d\epsilon' \quad (5.30)$$

where ϵ is the energy measured from the Fermi surface, $f(\epsilon)$ the Fermi-Dirac function and the spectral function $L(\omega, \epsilon, \epsilon')$ is a function of the quasi-particle energy $E = \sqrt{\epsilon^2 + \Delta(T)^2}$ and the BCS gap $\Delta(T)$. Note that the BCS theory also assumes dissipative normal electrons, and should therefore only be used in combination with the Drude model description. The integration over ϵ and ϵ' is computationally consuming, and via the Kramers-Kronig relations another integration over the frequency is needed to arrive at the desired expression of the dielectric permittivity at imaginary frequencies. A less consuming calculation is offered in Ref. [134]. There it was found

that impurity scattering lowers the dielectric permittivity and therefore the Casimir force compared to the two-fluid model. This means that according to BCS theory, at $T \ll T_c$ the Casimir force will not reach the value predicted by the plasma model. The calculations in this chapter, obtained with the two-fluid model, therefore give an overestimation of the Casimir force and therefore of the expected influence of superconductivity on the Casimir force.

The calculated Casimir pressure between two plates of niobium titanium nitride (NbTiN) is shown in Figure 5.6(a) as a function of temperature. NbTiN is the material we use in our experiments and has a critical temperature (T_c) of 13.6 K. In the calculations, the plates are separated by 100 nm. The Casimir pressure according to the plasma model is indicated by the orange line. The green line shows the Casimir pressure as calculated by the Drude-two-fluid model.

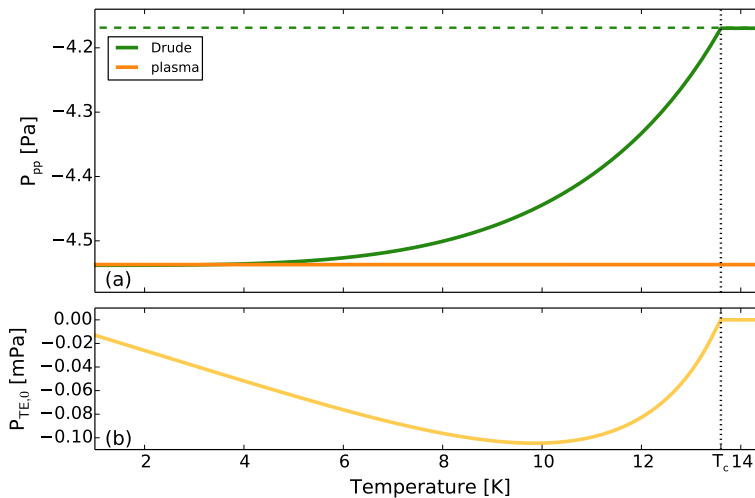


Figure 5.6: Casimir pressure between two niobium titanium nitride plates at a distance of 100 nm: (a) Total pressure described by the Drude model plus two-fluid model (green line) and plasma model (orange line). The Lorentz oscillations accounting for the core electrons are included in the calculations. According to the Drude model description, the pressure between the two superconductors transitions from the Drude model value above the critical value of 13.6 K towards the plasma value at 0 K. The plasma model description predicts no significant changes over temperature. The calculations are based on a plasma frequency of $\Omega_p = 5.33$ eV and relaxation rate $\gamma = 0.42$ eV; (b) Contribution of the zero order TE mode only, the calculation is based on the reflectivity given in Eq. 5.29.

Below the critical temperature, the magnitude of the pressure increases towards the pressure calculated by the plasma model. For comparison, the calculation based on the Drude model only is extended by the dashed green line below the critical temperature, as if no superconducting transition occurs. All the calculations are based on a plasma frequency of $\Omega_p = 5.33$ eV and relaxation frequency of $\gamma = 0.42$ eV. The contributions of four Lorentz oscillators are included as well. We refer to chapter 8

for a more detailed description of how these values are obtained from optical spectra of NbTiN.

As predicted, the plasma model shows no change with temperature. The Drude-two-fluid model shows a gradual transition in the Casimir pressure from the Drude model value above the critical temperature to the plasma model value at $T \ll T_c$. The superconducting transition should therefore only show a significant change in Casimir pressure with temperature for the Drude model. If we compare the expected Casimir pressure at low temperature with the pressure just above the critical temperature, we find a difference of 8.8% compared to the pressure around T_c . A temperature-dependent measurement of the Casimir force can therefore distinguish between the two models as the absence or presence of a change of the order of 8.8%, which should be detectable with our current measurement accuracy.

The contribution of the zero-order TE mode in the Drude-two-fluid model is plotted in Figure 5.6(b). Above the critical temperature it is equal to zero, as the Drude model describes. Below the critical temperature, the contribution increases as the reflectivity increases according to Eq. 5.29. Due to the prefactor $k_B T / \pi$ in Eq. 5.11, this zero-order contribution also decreases eventually as the temperature is decreased. Note that the zero-order contribution is very small compared to the total Casimir pressure, the change in this term is too small to explain the total effect of 8.8% change with temperature.

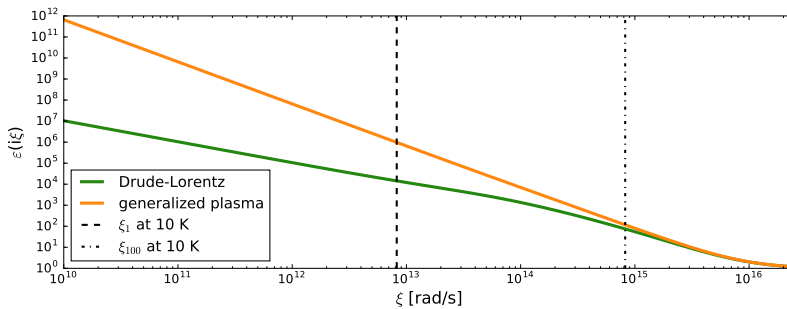


Figure 5.7: Dielectric permittivity of niobium titanium nitride at imaginary frequencies $i\xi$ as function of frequency. The plot is based on actual optical data of our NbTiN sample, extrapolated to lower frequencies either via the Drude-Lorentz model (green line) or generalized plasma model (orange line). The position of the first order Matsubara frequency at 10 K is indicated and shows that the two models predict different contributions at this frequency as well. Even at the hundredth Matsubara frequency, also indicated, the two models differ.

To better understand this seeming discrepancy, we take a closer look at the dielectric permittivity of niobium titanium nitride at imaginary frequencies, which is plotted in Figure 5.7. This plot is similar to the graph in Figure 5.3. In chapter 8 we will explain how the optical data were obtained that lead to values for the plasma and relaxation frequencies as well as the parameters describing the Lorentz oscillators, which are used either for the Drude-Lorentz model (green line) or for the

generalized plasma model (orange line).

Compared to the dielectric permittivity of gold, the two models coincide at a much higher frequency, this is caused by the higher resistivity of NbTiN (we measured a resistivity of $1.1 \pm 0.6 \times 10^{-6} \Omega\text{m}$, two orders of magnitude higher than reported values of gold). The vertical dashed line indicates the position of the first order Matsubara frequency at 10 K. Note that in contrast to the situation with gold, both models lead to a different dielectric permittivity at this frequency, which means that both models contribute differently to the Casimir force at this frequency. Even up to the hundredth Matsubara frequency, differences could be observed between the models. Although the total number of contributing Matsubara frequencies is larger at low temperatures (at 10 K, this is about 2500), there still are relatively more frequencies at which the contribution is different for the two models than in the case of gold at room temperature. These added contributions at the first hundred Matsubara frequencies can explain a much larger total difference in the Casimir force than can be explained by the zero-order TE mode only.

5.6 Casimir force with experimental parameters

The calculations so far are based on an idealized situation. In an experimental set-up, certain parameters differ from this situation, which may influence the effect of the superconducting transition. Although the calculations all express the Casimir force in the plate-plate geometry, actually measuring the force between two plates is technically challenging [135]. Most experiments, as well as the experiments in this thesis, are set up in a sphere-plate geometry. A theoretical prediction about the force between a sphere and a plate, can be derived from the parallel-plate pressure via the proximity force approximation (PFA) [136–138], which relates the parallel-plate pressure to the sphere-plate force gradient:

$$\frac{\partial F_{sp}}{\partial d} \approx 2\pi R P_{pp}, \quad (5.31)$$

where R is the sphere radius. The error in the approximation is estimated [139] to be of the order of d/R , which for significantly large spheres with a radius around $100 \mu\text{m}$, at distances around 100 nm is around a tenth of a percent. Since we are ultimately only interested in a relative difference below and above the critical temperature, this error falls away. In our experimental set-up we measure the sphere-plate force gradient divided by the sphere radius, which is equal to 2π times the parallel-plate pressure.

The choice of which superconductor to use is motivated by several arguments. As mentioned in section 5.4, less higher order Matsubara frequencies contribute to the force when the temperature increases. If we want to investigate specifically the effect of the 0-frequency contribution, we want to do the measurements preferably at a high temperature. Superconductors with a high critical temperature exist, but can be prone to oxidation, which may result in surface charges. These charges hinder the calibration of our set-up. We have therefore chosen niobium titanium nitride (NbTiN) as our superconductor. Thin film NbTiN has a critical temperature near 15 K [140] and the presence of the nitrogen atoms prevents oxidation.

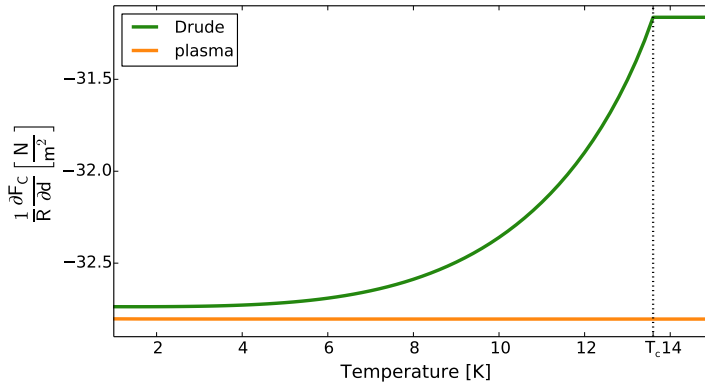


Figure 5.8: Casimir force gradient, normalized to the sphere radius, between a gold sphere and a niobium titanium nitride plate as a function of temperature. The green line shows the situation where the gold sphere and the normal electrons in the NbTiN plate are described by the Drude model, while the orange line shows a description by the plasma model.

During the measurements we want to be sure that the superconductors are indeed in the superconducting state. For the plate, this can be done by monitoring the plate's resistance. But for the sphere, this is technically more challenging since attaching wires to a microsphere is not very feasible. A more feasible method would be to position the sphere in a magnetic field and read out the change in this field by a SQUID as the sphere transitions to its superconducting state [141]. But this required a significant alteration to our initial set-up. We have therefore chosen to pair the superconducting plate with a gold sphere. Note that this is far from ideal if we wish to probe the zero-frequency term specifically. The Casimir force depends on the multiplication of the reflectivities of the surfaces. For the TE mode at zero frequency, the Drude model sets the reflectivity of gold to zero, such that the effect of the change in static reflectivity of the superconductor is canceled. Physically, it is like only one mirror exists for this mode. The plasma model does lead to nonzero contributions of both mirrors, but they are small and hard to distinguish in comparison to the zero contribution predicted by the Drude model. However, the higher order modes still lead to significant changes between the Drude and plasma models, so the effect of the superconducting transition should still be visible as a possible change in the contribution of these modes.

Figure 5.8 shows the Casimir force gradient, normalized to the sphere radius, between a gold coated sphere and a NbTiN plate as a function of temperature at a sphere-plate separation of 100 nm.

Two situations are depicted. In the first situation (green line), the spherical gold surface and flat niobium titanium nitride surface above the critical temperature are described by the Drude-Lorentz model, while the superconductor (NbTiN below the critical temperature) follows the two-fluid model. As with the parallel NbTiN plates, Figure 5.6, there is a continuous transition across the critical temperature. At

$T \ll T_c$, the force gradient does approach the plasma-model prediction, but does not reach the same value, since the gold sphere still follows the Drude-Lorentz model.

In the second situation, the gold surface follows the generalized plasma model, as does the NbTiN in its normal state. The two-fluid model is still used for the superconductor, but now describes a mixture of plasma-like superconducting electrons and plasma-like normal electrons, so in effect we can use the generalized plasma model for the NbTiN below the critical temperature as well. The orange line in Figure 5.8 indicates that there is hardly any change in the Casimir force gradient with temperature.

In the Drude model description, the force gradient changes about 5.1% compared to the value at the critical temperature. This is less than the change with temperature between two NbTiN parallel plates, but it is still measurable. For comparison, room temperature measurements were reported with a relative error of 0.19 to 9.0 percent [11].

5.7 Conclusions and outlook

The Casimir force between real conductors is determined by the frequency dependent, complex dielectric permittivity of the opposing surfaces. Full knowledge of the dielectric permittivity is required, since electromagnetic waves at all frequencies (up to a certain cut-off frequency) contribute. To avoid oscillations in the integrand, the frequency path of integration is transformed from real to imaginary frequencies. At finite temperatures, only a discrete set of frequencies, known as the Matsubara frequencies ξ_n , contribute to the Casimir force. The dielectric permittivity at a certain Matsubara frequency follows from a integration of the dielectric permittivity over all real frequencies, but the integrand is weighted by each ξ_n , such that the greatest contribution comes from the frequency range around the given Matsubara frequency. Effectively, only knowledge of the dielectric permittivity around the Matsubara frequencies is necessary, which somewhat lifts the requirement to know the full dielectric permittivity. For gold at room temperature, the dielectric permittivity at all higher order frequencies can be deduced from measurements and only the static contributions remain unknown. Since the contribution from the static electric field can be determined from the reflectivity, only the contribution from the static magnetic field remains open to debate. In superconductors, the reflectivity for the static magnetic field is determined by the Meissner effect. Therefore, measurements of the Casimir force between superconductors may give information on the contribution of this field to the total force.

For two plates of niobium titanium nitride, we calculate an effect of 8.8 percent across the superconducting transition. This is significantly larger than what you would expect based on a possible change at only one Matsubara frequency. From the dielectric permittivity of NbTiN at imaginary frequencies we can induce that certain higher order modes also contribute differently to the Casimir force for the Drude and plasma models. Across the superconducting transition it is not only the zero-order mode that changes, which explains the large effect. For an experimentally more accessible geometry of a niobium titanium nitride plate paired with a gold sphere, this

effect is smaller, a little more than 5 percent. Note that our calculations overestimate these percentages, since the two-fluid model predicts a larger effect than the physically more correct BCS theory. The experiments in the following chapters will show whether the effect of the superconducting transition is indeed measurable and if so, what the magnitude of this effect to the Casimir force is.

Details of the Experimental Techniques

In the past, measurements of the Casimir force were performed using different kinds of experimental set-ups. The first measurements relied on macroscopic objects, such as two metallic parallel plates [44] or a lens and a plate [45, 46]. Technological progress allowed an enhanced force sensitivity and sensor read-out, as well as force measurements between microscopic surfaces. Modern set-ups for Casimir force measurements include torsion pendulums [47, 50], atomic force microscopes [51, 52, 54, 142–144], microelectromechanical systems [145], micromechanical cantilevers [135] and micromechanical torsional oscillators [11, 146, 147]. For an overview of Casimir force experiments, see for example Refs. [98, 148].

In this thesis we will use a set-up based on atomic force microscopy. We have attached a polystyrene sphere with $200\ \mu\text{m}$ diameter on a micromechanical cantilever, such that the cantilever and sphere act as a force sensor [149]. When the sphere is positioned above a plate, any force between the sphere and plate causes changes in the cantilever motion. We read out this motion using fiber interferometry [92, 150]. The first part of this chapter will describe fiber interferometry in more detail and its possibilities and limits when applied to our set-up. We also investigate the use of graded index (GRIN) lenses to focus the light onto the cantilever.

Since surface roughness influences Casimir force measurements, it is important that the surfaces can still be considered flat at the smallest sphere-plate separation. We will show topography images of our gold coated sphere as well as of the two plate coatings that are used for Casimir force measurements in this thesis: gold and the superconductor niobium titanium nitride. We will also show that cooling has no effect on the gold coating of the sphere.

A description of our measurement method will follow in chapter 7. There we will explain that it depends on the potential we set on the plate. We simultaneously want to perform a conductance measurement of the superconducting plate to check whether it is in its normal or superconducting state. These two measurements may not interfere. In the final part of this chapter we will explain our plate resistance detection scheme that can run simultaneously with our Casimir force measurement.

6.1 Fiber interferometry

Fiber interferometry [92, 150] is based on the interference between light reflected at the end facet of a single-mode fiber and light that is reflected at a surface some distance d in front of the fiber end facet. Since the light originates from the same laser source and follows the same path through the fiber, the interference signal is in principle only sensitive to changes between the fiber end and reflective surface. In order to deduce a general formula for the interferometer signal, we need to know the amplitudes of the two reflected beams, which are indicated in Figure 6.1.

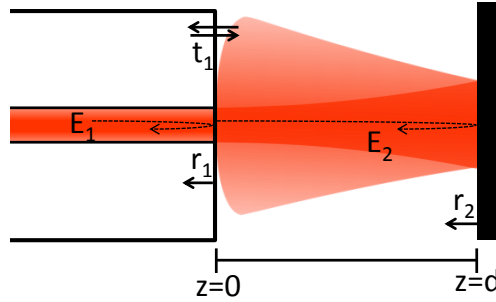


Figure 6.1: Schematic image of a fiber end in front of a reflective surface, separated by a distance d . Also shown are the reflection and transmission coefficients and the paths of the two interfering beams with amplitudes E_1 and E_2 .

Light propagates through the fiber and encounters a 4% intensity reflection at the fiber-to-air interface. The normalized amplitude of the Gaussian beam reflected at this surface is given by [151]:

$$E_1(r, t) = -r_1 \sqrt{\frac{2}{\pi}} \frac{1}{w_0} e^{-\frac{r^2}{w_0^2}} e^{-i\omega t}, \quad (6.1)$$

where $r^2 = x^2 + y^2$, $-r_1$ is the reflection coefficient at the fiber-to-air interface¹, w_0 is the beam waist at $z = 0$ and ω is the angular frequency of the light.

The second beam is coupled out of the fiber, reflected at the second surface a distance d away and coupled back into the fiber. In the first step, the amplitude is multiplied by the transmission coefficient t_1 . The light then travels a distance z where the beam waist w and radius of curvature R are altered according to:

$$w(z) = w_0 \sqrt{1 + \left(\frac{z}{z_R}\right)^2} \quad (6.2)$$

$$R(z) = z + \frac{z_R^2}{z} \quad (6.3)$$

¹Note the minus sign, which is due to time-reversal invariance. The Stokes relations dictate a phase difference of 180° between internally and externally reflected light [152].

with the Rayleigh length $z_R = \pi w_0^2/\lambda$ and λ the wavelength of the light. At the second surface, the light picks up a reflection coefficient r_2 . The light then travels back to the fiber end facet; the total travel distance is equal to $2d$. Since both the beam waist and radius of curvature have changed, the beam no longer overlaps with the fiber core. We need to find the coupling coefficient that describes how much light couples back into the fiber. The effect of the radius of curvature can be ignored, however, regardless of the travel distance. For small distances, the curvature hasn't changed much and the beam is still effectively flat. At large distances the beam is curved significantly, but since the beam has expanded as well, we can assume that the beam is locally flat at the fiber core³. So we just look at the coupling coefficient between a beam with waist $w(z)$ and the fiber mode with waist w_0 . Since the beams are normalized, the coupling coefficient is given by the overlap integral:

$$\begin{aligned}\eta_c(z) &= \int_0^\infty \frac{2}{\pi} \frac{1}{w_0} e^{-\frac{r^2}{w_0^2}} \frac{1}{w(z)} e^{-\frac{r^2}{w^2(z)}} 2\pi r \, dr \\ &= \frac{2w_0 w(z)}{w_0^2 + w^2(z)} = \frac{2\sqrt{1 + (z/z_R)^2}}{2 + (z/z_R)^2}.\end{aligned}\quad (6.4)$$

Considering this coupling coefficient and an extra factor t_1 to account for the transmission back into the fiber, the amplitude of the second beam in the fiber is given by

$$E_2(r, t + \tau) = \eta_c t_1^2 r_2 \sqrt{\frac{2}{\pi}} \frac{1}{w_0} e^{-\frac{r^2}{w_0^2}} e^{-i\omega(t+\tau)}, \quad (6.5)$$

where $\tau = 2d/c$ is the time delay resulting from the extra path length. The detector signal W follows from the autocorrelation function of the sum of the two beams [153], multiplied by the detector responsivity ρ :

$$\begin{aligned}W(d, f) &= \rho \langle \{E_1(r, t) + E_2(r, t + \tau)\}^* \{E_1(r, t) + E_2(r, t + \tau)\} \rangle \quad (6.6) \\ &= \frac{\rho}{T} \int_{-T/2}^{T/2} \{E_1(r, t) + E_2(r, t + \tau)\}^* \{E_1(r, t) + E_2(r, t + \tau)\} dt \\ &= \rho \left[r_1^2 \frac{2}{\pi w_0^2} e^{-\frac{2r^2}{w_0^2}} + \eta_c^2 t_1^4 r_2^2 \frac{2}{\pi w_0^2} e^{-\frac{2r^2}{w_0^2}} - \eta_c r_1 t_1^2 r_2 \frac{2}{\pi w_0^2} e^{-\frac{2r^2}{w_0^2}} (e^{-i\omega\tau} + e^{i\omega\tau}) \right] \\ &= \rho I_1 + \rho I_2 - 2\rho \sqrt{I_1 I_2} \cos(\omega\tau).\end{aligned}\quad (6.7)$$

The first (second) term can be recognized as the intensity of the first (second) beam, while the last term is the interference term. In this term one can recognize the interferometric visibility

$$V(d) = \frac{2\sqrt{I_1 I_2}}{I_1 + I_2} = \frac{2\eta_c(d)r_1 t_1^2 r_2}{(r_1^2 + \eta_c^2(d)t_1^4 r_2^2)}. \quad (6.8)$$

³Mathematically, the condition holds if we can ignore the contribution $e^{\frac{i\pi r^2}{\lambda R(z)}}$ of the radius of curvature to the Gaussian beam, which is true if $\frac{\pi r^2}{\lambda R(z)} < 1$. At the fiber core, $r = w_0$, so the condition becomes $\frac{\pi w_0^2}{\lambda} = z_R < z + \frac{z^2}{z_R} = R(z)$, which always holds.

If we call $W_0 = \rho(I_1 + I_2)$ the midpoint signal, we can rewrite the previous equation in a more compact form

$$W(d, f) = W_0 - W_0 V \cos\left(\frac{4\pi f d}{c}\right). \quad (6.9)$$

A fiber interferometer is often used to detect small fluctuations ($\Delta d \ll \lambda$) on top of a large gap distance ($d \gg \lambda$). The sensitivity to detect these fluctuations is maximum at the quadrature point, which can be achieved by either tuning the gap distance or the laser frequency. In our set-up, we fix the gap distance and tune the laser frequency to quadrature. Since the visibility decreases at large distance, this gap distance cannot be too large. But if the gap distance is small, the frequency scan range of the laser can be insufficient to find the quadrature point. To overcome the requirement to operate the interferometer at quadrature point, the signal can be modulated. The modulated term in the interference signal is at phase quadrature with the original term, therefore always warranting maximal sensitivity. Since distance modulation is often not feasible, commercial interferometers tend to modulate the laser frequency, which may result in added noise to the signal. In chapter 7 we will describe this method in more detail.

The gap distance in the interferometer that reads out the cantilever motion is fixed at 200 – 300 μm , which is small enough to obtain a high visibility and large enough for our laser to scan almost half a period of the cosine in the interferometer signal. We therefore do not use any modulation techniques in this read-out.

The interferometers are fed by a 1550 nm, 20 mW laser module with a frequency scan range of 250 GHz. We use two distributed feedback (DWDM DFB) lasers with adjacent frequency ranges (Thorlabs LS5-C-24A-20-NM and LS5-C-22A-20-NM) to increase the scan range even further. The laser module where the frequency is in quadrature point is used for the cantilever interferometer, the other is used to read out the motion of the plate under the cantilever. The light of each laser first passes through an optical isolator (Thorlabs IO-H-1550APC) to protect the laser from back-reflected light. The light then goes through a 90/10 fiber coupler (Thorlabs 10202A-90-APC) of which the 90% port is terminated and the 10% port is connected to a fiber with a cleaved fiber end. The reflected light passes the coupler again, now 90% falls onto a detector (Thorlabs PDA10CS).

With the cantilever interferometer we want to detect small forces that are manifested as small deviations in the cantilever motion. A question that arises is what the smallest detectable motion, or noise floor, is. The noise floor is mostly influenced by mechanical noise from vibrations from the outside world. But even when the set-up is mechanically stable, there is an intrinsic noise floor caused by the laser phase noise. This noise floor can be calculated from the laser linewidth using the interferometer signal. We want to know the influence of the laser linewidth Δf on the signal linewidth ΔW when the laser is tuned at quadrature ($\sin(4\pi f d/c) = 1$):

$$\Delta W = W_0 V \frac{4\pi d}{c} \sin\left(\frac{4\pi f d}{c}\right) \Delta f = W_0 V \frac{4\pi d}{c} \Delta f. \quad (6.10)$$

To obtain the signal noise floor in meters, we divide the signal linewidth by the

sensitivity $4\pi W_0 V/\lambda$ and the square root of the bandwidth B :

$$\Delta d_{\min} = \frac{d\lambda}{c} \frac{\Delta f}{\sqrt{B}}. \quad (6.11)$$

With a fiber-to-cantilever distance $d = 200 \mu\text{m}$, laser wavelength $\lambda = 1550 \text{ nm}$ and linewidth $\Delta f < 10 \text{ MHz}$ we find a noise floor of $\Delta d_{\min} < 327 \text{ fm}/\sqrt{\text{Hz}}$ for a bandwidth of 1 kHz . To check this value, we measured the spectrum of the cantilever interferometer signal, shown in Figure 6.2. The cantilever motion is clearly visible around 2.3 kHz . From a fit through the data, we could obtain a resonance frequency of 2306 Hz and mechanical quality factor $Q = 4.85 \times 10^3$. These are reasonable values for a cantilever in vacuum at room temperature. This tells us that the fit is reasonable, despite the fact that the spectrum analyzer's low frequency noise has not been taken into account in the fit. From the fit we determine a noise floor of $103 \text{ fm}/\sqrt{\text{Hz}}$. This is somewhat lower than the calculated value, but differences can be explained by a smaller fiber-to-cantilever distance and lower laser linewidth.

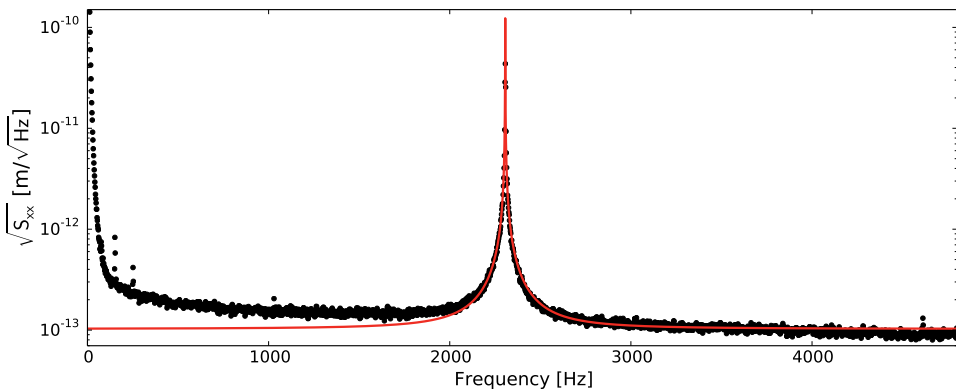


Figure 6.2: Noise spectrum from the cantilever interferometer signal. The cantilever motion at 2.3 kHz is clearly visible. From a fit (red line) through the data we could determine a noise floor of $103 \text{ fm}/\sqrt{\text{Hz}}$. This value is somewhat lower than the calculated value of $327 \text{ fm}/\sqrt{\text{Hz}}$, which may be explained by a lower laser linewidth or smaller fiber-to-cantilever distance. The low frequency range of the spectrum is dominated by pink noise from our spectrum analyzer, which is not taken into account in the fit.

We have compared our home build fiber interferometer with several commercially available interferometers from Optics11 (OP1550) and Attocube (IDS3010). The OP1550 came in two versions, standard with a sampled grating distributed Bragg reflector (SG-DBR) laser diode or upgraded with an external-cavity diode laser (ECL). The interferometers of Optics11 could be directly connected to our set-up, such that the measurements could be obtained under similar circumstances. The Attocube interferometers can only be combined with their sensor heads, that require a large distance between the reflective surfaces of at least several millimeters. All interferometers showed a higher noise floor. The noise floor of the OP1550 was $3 \text{ pm}/\sqrt{\text{Hz}}$

for the SG-DBR laser and $300 \text{ fm}/\sqrt{\text{Hz}}$ for the ECL. With the IDS3010 we measured a noise floor between 22 and $33 \text{ pm}/\sqrt{\text{Hz}}$ depending on the sensor head. This shows that the flexible use of commercial interferometers limits their achievable sensitivity and that our noise floor of $100 \text{ fm}/\sqrt{\text{Hz}}$ is very reasonable. It is especially advantageous that our interferometer can operate at very small distances, since the noise floor depends linearly on the fiber-to-cantilever distance when the dominant noise source is laser phase noise. Note that this requires a laser with a reasonably large frequency scan range, such that the laser can always be set at the quadrature point.

When the distance can no longer be decreased, the noise floor can be lowered by using a laser with a smaller linewidth. But this effect is not limitless. Interference occurs between all reflected light beams, not just between light reflected at the fiber end facet and at the cantilever. Reflections at for example fiber connectors may result in unwanted interferences. Due to small changes in the fiber length caused by temperature fluctuations in the cryostat, or changes in the amount of the light reflected at the connectors, the unwanted interferences do not just add a static background. All vibrations in the system now show up in the interferometer signal. Since interference can only occur between coherent beams, a solution to avoid this effect is to lower the coherence length of the laser to the fiber-to-cantilever distance. This however also enlarges the laser linewidth, so a compromise has to be made. Our lasers allow for coherence control via a small signal modulation on the laser current. The effect of this modulation is depicted in the noise spectrum of our cantilever interferometer signal in Figure 6.3. The laser current was modulated at 18.5 kHz at different modulation depths. The laser linewidth can be increased from less than 10 MHz with no modulation to more than 1 GHz at full modulation. The red line in Figure 6.3 displays the noise spectrum without any modulation, which results in

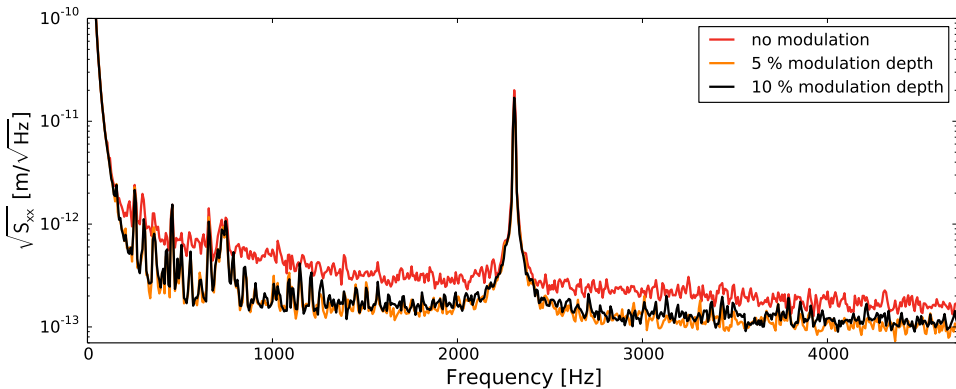


Figure 6.3: Noise spectrum from the cantilever interferometer, without modulation (red line) and with 5 percent (orange line) and 10 percent (black line) modulation. The modulation decreases the noise floor by a factor of three, but a modulation depth of more than a few percent has no further effect. The noise peaks are caused by noise in our electronics and by mechanical vibrations in our cryostat.

a noise floor of about $300 \text{ fm}/\sqrt{\text{Hz}}$. A modulation depth of five percent lowers the noise floor roughly three times, but further reduction of the coherence length has no more influence on the noise floor. We therefore kept the modulation at a modulation depth of five percent during our measurements.

6.1.1 GRIN lenses to focus light

Our measurement scheme based on interferometric read-out of the cantilever motion assumes only interference between the light reflected at the fiber end facet and cantilever. Spurious reflections will result in parasitic interferences in our signal. Especially harmful is light reflected at the plate underneath the cantilever, because that results in a parasitic interference that changes during a measurement run while the cantilever-plate distance is varied. To prevent this, several options are available. Decreasing the laser coherence length to only several hundred micrometers is technically not achievable. The plate can be made from an absorptive material, but this will severely limit the choice of materials for the Casimir measurements. Another option is to position the fiber under an angle, to prevent light reflected at the plate from coupling back into the fiber (compare with the read-out in atomic force microscopes via a quadrature detector), but this will also influence the read-out of the cantilever motion. The best option is to use the cantilever to block the light from the fiber before it reaches the plate. Especially since a relatively large sphere is attached to the cantilever, this proves to be a practical solution. It is not completely reliable, however, because during our sample fabrication we have no way to check that all the light is blocked.

The possibility of stray light to couple back into the fiber is significant since the light from the fiber is divergent. We therefore investigated the option to focus the light onto the cantilever, using graded index lenses because of their size and compatibility with fibers. A graded index (GRIN) lens is a cylindrical rod where the index of refraction varies radially [152] according to

$$n(r) = n_0 \left(1 - \frac{\zeta^2 r^2}{2} \right), \quad (6.12)$$

where n_0 is the index of refraction at the center and ζ a positive constant indicating the variation towards the curved edge. How the light is propagated through the lens is determined by the change in refraction index and by its length. A common use of GRIN lenses is to collimate light from a fiber by placing a lens with the correct length directly behind it. The collimated light then has a beam waist (radius) of roughly 40 to 200 μm for commercial GRIN lenses. This is still too large compared to our cantilever width of 50 μm . By increasing the distance between the fiber and GRIN lens (distance v in Figure 6.4), it is possible to focus the beam onto the cantilever.

The resulting beam waist and the required distances depend on the GRIN lens and can be calculated via ray matrices [154, 155], with the ray matrix describing the propagation through a GRIN lens given by [151]

$$M_{\text{GRIN}} = \begin{bmatrix} \cos(\zeta z) & \sin(\zeta z)/n_0\zeta \\ -n_0\zeta \sin(\zeta z) & \cos(\zeta z) \end{bmatrix}, \quad (6.13)$$

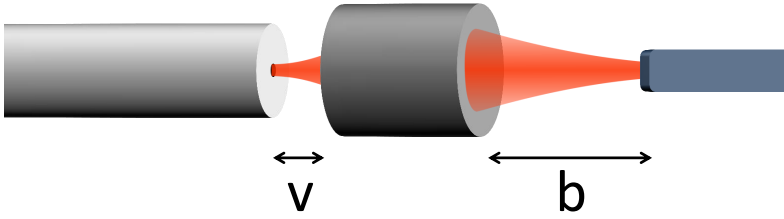


Figure 6.4: Diagram of the single mode fiber (left), graded index (GRIN) lens (middle) and cantilever (right). The light beam path is indicated, as well as the fiber-to-lens distance v and lens-to-cantilever distance b . By focusing the beam onto the cantilever via a GRIN lens, it is less likely that light reflects on the plate under the cantilever and is coupled back into the fiber to cause unwanted interference.

where z is the length of the lens. To block the light completely with the cantilever, a beam waist of less than $25\ \mu\text{m}$ is required. This can be achieved with distances v and b of several millimeters. Combined with the GRIN lens length of several millimeters, this results in a distance of at least 8 mm between the cantilever and the fiber end facet. These are the only reflective surfaces in the set-up, since GRIN lenses are AR coated to suppress extra reflections on the facets. However, a gap of 8 mm significantly increases the noise floor of the interferometer, such that the cantilever motion can no longer be detected. A technically challenging solution would be to apply anti-reflection coatings on the fiber end and on one facet of the GRIN lens, such that the reflective surface is now the facet of the GRIN lens positioned closest to the cantilever. But even then the minimum gap distance is of the order of a millimeter.

Therefore, a reliable way to focus the beam onto the cantilever using GRIN lenses could not be obtained with commercially available lenses. A custom-made GRIN lens designed for a small gap between the reflective surfaces may still be a solution, but this would have to be investigated further.

6.2 Sample characterization

As a second step in our set-up characterization, we take a closer look at our samples. Our force probe is a polystyrene sphere (Thermo Scientific 4320A, radius $100\ \mu\text{m}$) that is attached to a micromechanical cantilever (Bruker RESP-20) with UV-curable adhesive (NOA 81), using a micropositioning system. The sphere and cantilever are then coated with a 4 nm titanium adhesion layer and a 200 nm conductive layer of gold in a sputtering machine (Leybold Z400).

A larger sphere radius increases the strength of the force. Also, in our data analysis we use several approximations that become more valid with larger sphere radius, as will be discussed in chapter 7. The largest commercially available spheres that we could find which still have an acceptable surface roughness [156], have a radius of $100\ \mu\text{m}$.

Surface roughness influences the strength of the Casimir and electrostatic forces at small distances and can even influence the effective separation [157, 158]. Therefore, the surface roughness limits the smallest distance at which the Casimir force can be reliably measured. Figure 6.5 shows an investigation of the large and small scale surface roughness of our spheres. The scanning electron microscope (SEM) image in Figure 6.5(a) shows that there are some flakes on the sphere. These may prevent an approach closer than several micrometers if they are located in the area of closest approach. There are, however, no other larger scale irregularities. Note that even though the SEM image is taken with a beam energy of 15 kV, no charging effects are shown on the sphere surface. This means that the gold layer is indeed conductive.

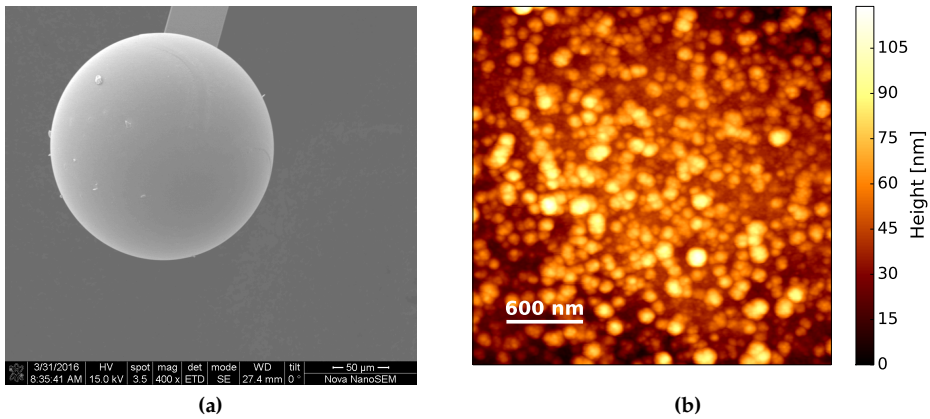


Figure 6.5: Characterization of the surface roughness of our force sensor, a $100\ \mu\text{m}$ radius sphere attached to a cantilever and coated with a $200\ \text{nm}$ conductive layer of gold: (a) SEM image, except for some micrometer sized flakes, there is no large scale surface roughness; (b) AFM topography image ($3\ \mu\text{m}$ by $3\ \mu\text{m}$) of the sphere surface, the surface roughness has an RMS value of $16.8\ \text{nm}$.

A tapping-mode atomic force microscopy (AFM) topography image of the sphere surface is shown in Figure 6.5(b). The surface roughness has an RMS value of $16.8\ \text{nm}$, mostly due to the surface roughness of the polystyrene sphere. Therefore, an approach of several tens of nanometers is in principle possible without a significant effect of surface roughness.

These force probes are meant to be operated at a base temperature of $4\ \text{K}$. But it is unknown whether the difference in thermal contraction between the polystyrene sphere and gold layer will cause the gold layer to flake. The SEM images in Figure 6.6 show the effect of cooling a gold coated sphere to $4\ \text{K}$ and warming up again. There is no difference visible before (Figure 6.6(a)) and after (Figure 6.6(b)) cool-down. This means that effects like peeling do not occur and that the force probes can safely be used at low temperatures.

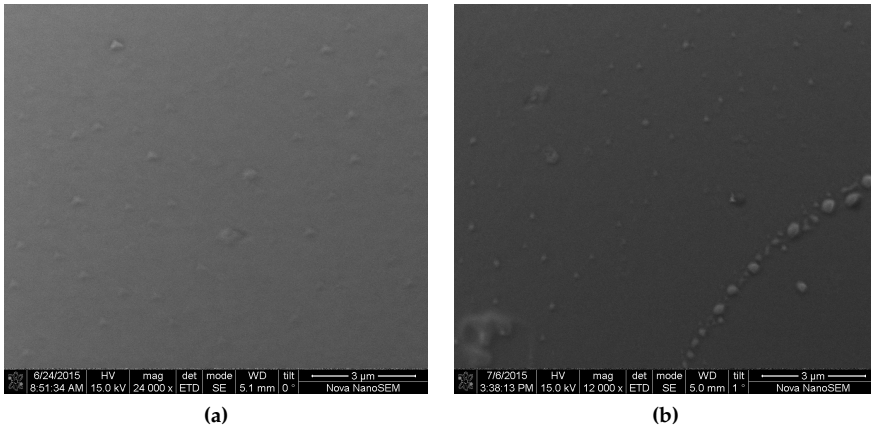


Figure 6.6: SEM images of the gold coated sphere surface (a) before and (b) after cooling the sphere down to 4 K. The absence of notable differences shows that cooling does not affect the coating on the spheres.

The distance of closest approach is not only determined by the surface roughness of the sphere, but also by that of the plate. The plate's surface roughness is determined with tapping-mode AFM topography scans. The scans are shown in Figure 6.7 for the different plate materials that were used: 150 nm gold on sapphire and 200 nm niobium titanium nitride (NbTiN) on SiO_2 respectively. From these scans we can determine the RMS surface roughness as 0.75 nm for gold and 1.13 nm for NbTiN. For all materials it should be possible to approach the sphere up to several tens of nanometers and we consider the plates to be perfectly flat for all practical purposes.

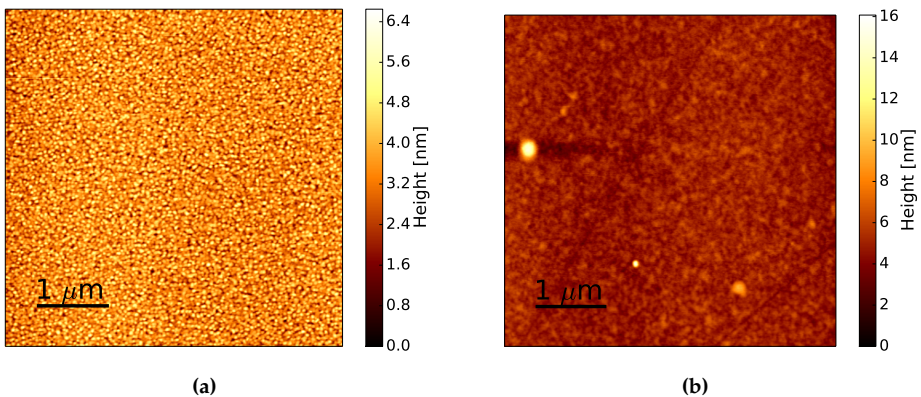


Figure 6.7: AFM topography images of the plates used for Casimir force measurements: (a) 150 nm gold on sapphire, with a surface roughness of 0.75 nm RMS; (b) 200 nm NbTiN on SiO_2 , with a surface roughness of 1.13 nm RMS

6.3 Plate resistance

Even though the NbTiN plate is made of a superconducting material, we want to be sure that the plate is superconducting at the time of a Casimir force measurement. Therefore we designed a resistance bridge that constantly compares the current through the plate with that through a reference resistance. We do not want this measurement to interfere with the Casimir measurements, where the calibration is based on the voltage $V = V_{DC} + V_{AC}$ between the sphere and the plate. This means we do not want our resistance detection scheme to cause any high voltages at the center of the plate, where the sphere is positioned. So we keep the potential of the plate's center at the voltage $V_{DC} + V_{AC}$ with respect to the sphere and then lift and lower the potential at the edges of the plate, each with a voltage $V_b/2$ with respect to the center. As is shown in Figure 6.8, the total voltage over the plate is then V_b and the current through the plate is detected by comparing it to an adjustable resistance at room temperature. When the plate resistance is equal to the adjustable resistance, the output of the resistance bridge is zero. Since a DC measurement is susceptible to drifts, we alternate the voltage V_b at 63 Hz with an amplitude of 0.5 V. The bridge imbalance output can then be monitored with a lock-in amplifier.

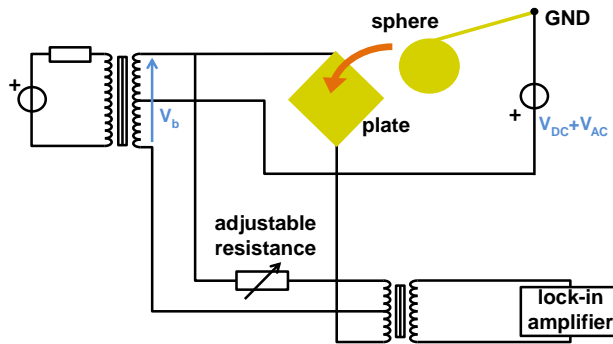


Figure 6.8: Schematic of the implementation of an extra plate resistance measurement while keeping the center of the plate at the desired potential for the electrostatic calibration.

At room temperature, we set the reference resistance to be equal to the plate's resistance. During cool-down we monitor the bridge output and the temperature of the plate. At the superconducting transition of the plate we observe a sudden jump in the bridge output, as shown in Figure 6.9. This jump is visible every time we heat or cool the plate through the superconducting transition. Since this detection method does not interfere with our other voltages, we can apply it during a Casimir measurement run and tell for each data point whether the plate was superconducting or not.

A real-time monitoring of the plate's resistance is necessary, since the critical temperature depends not only on the parameters of the NbTiN coating, but also on setup parameters that may differ per measurement run. This is demonstrated in Fig-

ure 6.9. Using a heater in the cryostat, we have swept the temperature of the plate through its superconducting transition as measured by the bridge imbalance output. During this sweep we have switched off the lasers and all unnecessary voltages. The sphere was retracted to a distance of several millimeters. Under these conditions, we measured a critical temperature of 13.7 K for the NbTiN coating (see yellow dots in Figure 6.9). Next we repeated these sweeps, but now we switched the laser feeding the plate interferometer on at different laser powers.

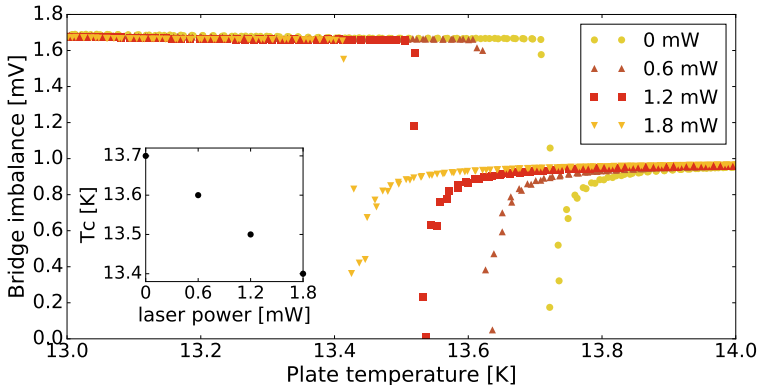


Figure 6.9: Output of the resistance bridge as a function of plate temperature. A sudden jump in the output is caused by the superconducting transition of the plate. The critical temperature of the NbTiN is found to be 13.7 K, but depends on the power of the laser light incident on the plate. The inset shows a linear dependence of the measured transition temperature on the laser power.

It is clear from the plot that the measured transition temperature is lowered when light shines on the plate. The inset shows a linear dependence on laser power, with the critical temperature being lowered to 13.4 K at 1.8 mW laser power. At low temperature, we use a laser power of 0.4 mW at the plate. There are several explanations for this behaviour. Since the laser light heats the plate from above and the thermometer is placed underneath, the plate may be warmer than the thermometer monitors, such that the actual critical temperature remains unaltered. It is also likely that the light negatively influences the superconducting state, thus lowering its critical temperature [159]. More precise measurement can find the actual reason behind this phenomenon, but lie outside the scope of this thesis.



Simultaneous Calibration Scheme for Casimir Force Measurements

In 1948 Casimir predicted the attractive force between two perfectly conducting plates in a vacuum. But experimental confirmation of this force proved to be difficult due to several factors. The challenge of positioning the two plates perfectly parallel [44, 135] is often circumvented by measuring the force between a plate and a sphere. But two other challenges remain, namely the calibration of the set-up and sphere-plate separation and the presence of the electrostatic force caused by a difference in surface potential between the two materials.

Calibration of the set-up and the distance is often done prior to the Casimir force measurements. Compensation of the electrostatic force is achieved at the start of a measurement run by setting a voltage over the sphere and plate such that the detected force is minimized. The disadvantage of these methods is that it is still sensitive to time-related drifts and distance-dependent contributions to the electrostatic force. That is why we use a method that runs simultaneously with our measurement run [144, 160]. We modulate the electrostatic force at a certain frequency by applying an AC voltage between the sphere and the plate. Based on the modulated force signal we can create a feedback loop that sets the distance at a desired value by adjusting the amplitude of the AC voltage.

In this chapter we will describe this measurement method. We show Casimir force measurements between a gold coated microsphere with radius $R = 100 \mu\text{m}$ and a gold coated sapphire plate. We compare our results with calculations of the Casimir force between two gold surfaces to show that our set-up can reliably measure the Casimir force.

7.1 Detection of the plate motion

The set-up is designed to measure forces at submicron distances in a sphere-plate geometry. The gold-coated sphere is attached to an atomic force microscope cantilever that acts as a force sensor. Read-out of the cantilever motion is done using a fiber-optic interferometer. The technique behind fiber interferometry, as well as our sample characterization is described in chapter 6. The cantilever is placed above a gold coated sapphire plate. The measurements were done at room temperature at a background pressure of 2.2×10^{-1} mbar and the whole set-up was placed on an isolated foundation separating it from vibrations from the outside world. A schematic image of the main components of our set-up is shown in Figure 7.1.

The plate is coated with a 150 nm thick layer of gold. It is mounted on a mechanical translation stage consisting of a stick-slip stepper motor (Attocube ANPz101) for coarse approach and a piezo-electric transducer for accurately varying the distance d between the sphere and plate. In this section we will describe the detection of the motion of the plate. In a later section we will show how the electrostatic force is used to relate this motion to the actual sphere-plate distance and to calibrate our force sensitivity.

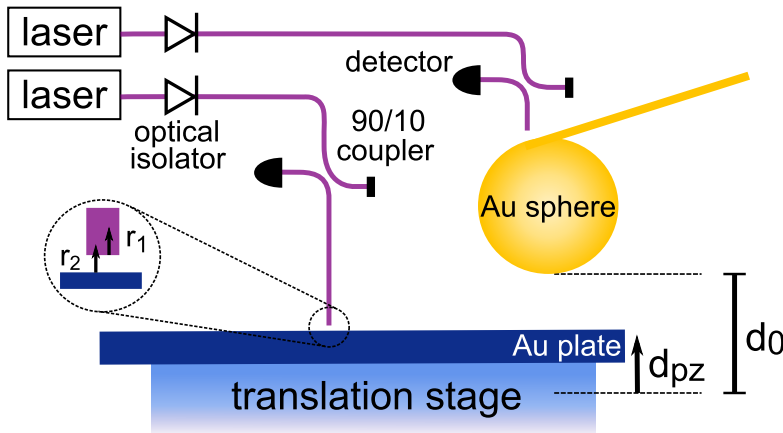


Figure 7.1: Schematic image of the set-up. During a measurement run, the distance d is varied by setting d_{pz} by a translation stage under the gold plate. A force between the gold sphere and plate results in a change in cantilever motion. The motion of both the cantilever and the plate is read out with fiber-optic interferometers. The interferometric signal depends on the interference of light reflected at the fiber end facet (r_1) and at the plate surface (r_2).

During a measurement run, the plate moves towards the sphere in steps. The distance between the sphere and the plate changes with d_{pz} compared to the initial separation d_0 , such that the actual sphere-plate distance is equal to $d = d_0 - d_{pz}$. The distance change d_{pz} , or plate motion, is recorded with a fiber-based common path interferometer [92]. The interferometer is fed by a tunable continuous wave dis-

tributed feedback (CW DFB) laser module (Thorlabs LS5-C-24A-20-NM) operating around $\lambda = 1550$ nm. The light is transported via a 90/10 fiber coupler to a cleaved fiber end positioned above the plate. Light reflected at the fiber end (r_1) interferes with light reflected from the plate (r_2) when it passes through the fiber coupler again and falls onto a detector. The interference signal at the detector is given by

$$W_{\text{DC}} = W_0 - W_0 V \cos\left(\frac{4\pi d_{\text{pz}}}{\lambda}\right) \quad (7.1)$$

where W_0 is the midpoint interference signal and V the interferometric visibility. The interferometer is most sensitive for values of d_{pz} where the phases from both reflections are in quadrature. This requirement can only be met for small changes in the distance ($d_{\text{pz}} \ll \lambda/4\pi$). This is not feasible for a typical measurement run, where we want to measure over a distance of several hundred nanometers.

To overcome this issue, the plate motion d_{pz} is modulated at $\omega/2\pi = 119$ Hz, with amplitude Δd of roughly 0.5 nm. Following a Taylor expansion, the interference signal now also contains an oscillating component in phase quadrature with the original signal, with amplitude

$$W_\omega = \frac{4\pi W_0 V \Delta d}{\lambda} \sin\left(\frac{4\pi d_{\text{pz}}}{\lambda}\right). \quad (7.2)$$

A point with low sensitivity in one term is now compensated by a high sensitivity in the other term. The distance change d_{pz} can be deduced from the phase-angle between the two terms:

$$d_{\text{pz}} = \frac{\lambda}{4\pi} \arctan\left(\frac{\lambda}{4\pi \Delta d} \frac{W_\omega}{W_0 - W_{\text{DC}}}\right). \quad (7.3)$$

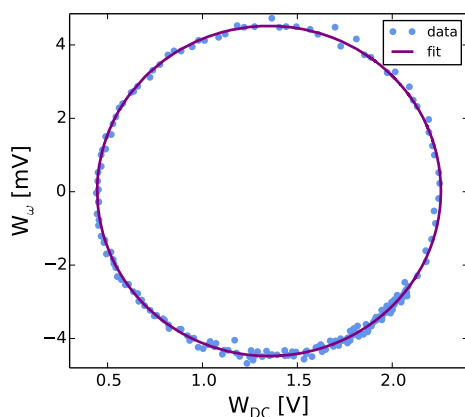


Figure 7.2: Lissajous plot of the two components of the plate interferometer signal, W_ω and W_{DC} (blue dots). The resulting ellipse is fitted (purple line) to find the distance change d_{pz} .

During a measurement run, the DC level of the detector signal from the plate interferometer, W_{DC} , is low-pass filtered and recorded with an ADC and the modulated signal W_{ω} with a lock-in amplifier with time constant 30 ms. To determine the values for W_0 and Δd , it is possible to fit W_{DC} and W_{ω} separately. But a more convenient choice is to display the two signals in a Lissajous plot and fit the resulting ellipse. Both the data and the fit are shown in Figure 7.2.

The correspondence between the fit and data tells us that the plate interferometer is well able to follow the plate motion and that disturbing effects such as external vibrations or piezo creep do not affect our measurements. From the axes and the center position we can deduce $W_0 = 1.35 \text{ V}$, $\Delta d = 0.61 \text{ nm}$ and the plate interferometric visibility $V = 0.67$. Using these values and Eq. 7.3 we can then determine d_{pz} . To calibrate the offset distance d_0 and therefore the actual distance between the sphere and the plate, we use the electrostatic force. In the next section we will explain the calibration method.

7.2 Calibration with the electrostatic force

The force sensor is based on a doped silicon micromechanical cantilever with nominal spring constant $k = 0.9 \text{ N/m}$ (Bruker RESP-20). A polystyrene sphere (Thermo Scientific 4320A) with radius $R = 100 \mu\text{m}$ is attached at the end of it. Both the sphere and the cantilever are covered with a 200 nm conductive gold coating. The cantilever motion and resonance frequency ($f_0 = 2.3 \text{ kHz}$) are read out by a second fiber-optic interferometer, positioned $200 \mu\text{m}$ from the cantilever and fed by a second, similar laser source. The laser frequency is tuned to quadrature point corresponding to the fiber-cantilever distance. A self oscillating circuit [161] drives the cantilever at its resonance frequency to ensure a constant cantilever amplitude of roughly 1 nm RMS.

With this force sensor we wish to detect the Casimir force F_C , but there also exists an electrostatic force caused by a voltage across the plate and the sphere. Even when there is no external voltage applied, there exists a contact potential difference V_0 caused by a difference in the materials' work functions. This difference can also exist between two surfaces of the same material, since different application circumstances may lead to variations in crystal face or in possible contamination. Although the electrostatic force can easily overcome the Casimir force in magnitude, it allows us to calibrate our force sensor and the actual distance between the sphere and plate as well as to detect and compensate V_0 .

Because the electrostatic force depends on the potential difference between the sphere and the plate, it can be altered we apply an additional voltage. More specifically, since the Casimir force does not depend on the voltage across the sphere and the plate, modulating this voltage at a known frequency allows us to separate the two forces. The signal from the force sensor at the modulation frequency $\omega_1/2\pi = 72.2 \text{ Hz}$ only shows the electrostatic contribution. The total voltage across the sphere and plate consists of an applied AC and DC voltage, plus the naturally present contact potential difference V_0 :

$$V = V_0 + V_{\text{DC}} + V_{\text{AC}} \cos(\omega_1 t). \quad (7.4)$$

We use the expression $F_{\text{ES}} = -\pi\varepsilon_0RV^2/d$ for the electrostatic force in a sphere-plate geometry, with ε_0 the vacuum permittivity. This expression is an approximation that holds in the limit of small distance compared to the sphere radius [138]. Later in this section we will check its validity. The total electrostatic force acting on the cantilever has multiple frequency components as well as a static component:

$$F_{\text{ES}} = -\frac{\varepsilon_0\pi R}{d} \left[(V_0 + V_{\text{DC}})^2 + 2(V_0 + V_{\text{DC}})V_{\text{AC}} \cos(\omega_1 t) + \frac{1}{2}V_{\text{AC}}^2 + \frac{1}{2}V_{\text{AC}}^2 \cos(2\omega_1 t) \right]. \quad (7.5)$$

The total force between the sphere and plate is detected as a change in the cantilever motion, where the cantilever's static deflection, oscillation amplitude and resonance frequency are influenced. The cantilever is deflected in accordance to Hooke's law, which results in a interferometer signal S given by

$$S = \frac{\gamma(F_C + F_{\text{ES}})}{k}, \quad (7.6)$$

with γ the sensitivity of the interferometric read-out in units of V/m. When the force oscillates slowly compared to the cantilever's resonance frequency, the cantilever can easily move in phase with the force. We will call this method of detection the quasi-static (QS) detection.

Since the electrostatic force has different frequency components, the signal can also be divided into different parts:

$$S = S_s + S_{\omega_1} \cos(\omega_1 t) + S_{2\omega_1} \cos(2\omega_1 t), \quad (7.7)$$

with static deviation and oscillation amplitudes given by

$$S_s = \frac{\gamma F_C}{k} - \frac{\gamma\pi\varepsilon_0 R}{kd} (V_0 + V_{\text{DC}})^2 - \frac{\gamma\pi\varepsilon_0 R}{2kd} V_{\text{AC}}^2 \quad (7.8)$$

$$S_{\omega_1} = -\frac{2\gamma\pi\varepsilon_0 R}{kd} (V_0 + V_{\text{DC}})V_{\text{AC}} \quad (7.9)$$

$$S_{2\omega_1} = -\frac{\gamma\pi\varepsilon_0 R}{2kd} V_{\text{AC}}^2 = -\frac{\kappa}{2d} V_{\text{AC}}^2, \quad (7.10)$$

with $\kappa = \gamma\pi\varepsilon_0 R/k$ the force sensitivity. The amplitudes are detected with lock-in amplifiers (time constant 300 ms) set directly on the cantilever interferometer signal. The static deviation can be influenced by drifts, which makes it an unreliable measure for the Casimir force. It is possible to modulate the Casimir force as well [160] by slightly oscillating the plate, thereby modulating the distance. But since our cantilever interferometer is very sensitive to spurious reflections from the plate (see chapter 6), we cannot separate the modulated Casimir force from the modulated plate motion. That is why we use a different detection method.

Since the force between the sphere and plate depends on separation, there exists a force gradient that changes the cantilever's resonance frequency according to [161]

$$\Delta f = -\frac{f_0}{2k} \frac{\partial(F_C + F_{\text{ES}})}{\partial d}. \quad (7.11)$$

A static force gradient leads to a frequency shift, while an oscillating force gradient results in a frequency modulation. We will refer to this force gradient detection method as the frequency modulation (FM) detection. There are also different components in the cantilever frequency change

$$\Delta f = \Delta f_s + \Delta f_{\omega_1} \cos(\omega_1 t) + \Delta f_{2\omega_1} \cos(2\omega_1 t). \quad (7.12)$$

with static frequency shift and frequency deviations given by

$$\Delta f_s = f - f_0 = -\frac{f_0}{2k} \frac{\partial F_C}{\partial d} - \frac{f_0 \pi \epsilon_0 R}{2kd^2} (V_0 + V_{DC})^2 - \frac{f_0 \pi \epsilon_0 R}{4kd^2} V_{AC}^2 \quad (7.13)$$

$$\Delta f_{\omega_1} = -\frac{f_0 \pi \epsilon_0 R}{kd^2} (V_0 + V_{DC}) V_{AC} \quad (7.14)$$

$$\Delta f_{2\omega_1} = -\frac{f_0 \pi \epsilon_0 R}{4kd^2} V_{AC}^2 = -\frac{\mu}{2d^2} V_{AC}^2, \quad (7.15)$$

where we assign the system parameter $\mu = f_0 \pi \epsilon_0 R / 2k$. Since a lock-in amplifier doesn't detect frequencies, we send the cantilever interferometer signal through a frequency-to-voltage converter that detects the cantilever frequency and translates it linearly to a DC voltage. Frequency modulations translate to modulations of the voltage, with the frequency deviation equal to the amplitude of the signal at the modulation frequency. The static frequency shift can be used to extract the Casimir force gradient. We detect the instantaneous cantilever frequency using a home-built software radio and a frequency counter (Agilent 53131A) on the (filtered) cantilever interferometer signal. We also use the phase-locked loop option of our lock-in amplifier (Zurich Instruments HF2LI). To obtain the frequency shift, we determine f_0 from data points far away enough that the Casimir force has an undetectable influence. The instantaneous frequency there is only affected by the known electrostatic force, which we can subtract to obtain f_0 .

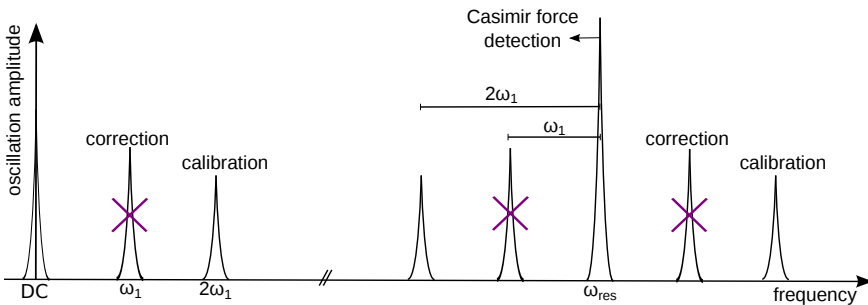


Figure 7.3: Frequency components in the cantilever interferometer signal. The quasi-static signals are at the low-frequency range of the spectrum, at ω_1 and $2\omega_1$. The frequency modulation signals appear as double side-bands around the resonator frequency. The signals at ω_1 are used to correct for the contact potential difference, via a feedback loop that minimizes these signals by applying a compensating DC voltage. The signals at $2\omega_1$ are used to calibrate the system. The Casimir force is detected as a shift in the cantilever resonance frequency.

An overview of the frequency components of our cantilever interferometer signal is shown in Figure 7.3. The quasi-static signals are located near DC and the frequency modulation signals appear as double sidebands around the resonance frequency of the cantilever. Both QS and FM signals can be used to calibrate the system and correct for the contact potential difference. The static shift of the resonance frequency is used to measure the Casimir force gradient.

We will first discuss how the influence of the contact potential difference is compensated using a technique similar to what is used in Kelvin probe force microscopy [162]. Note that the QS amplitude S_{ω_1} as well as the frequency deviation Δf_{ω_1} are proportional to the sum of the contact potential difference and our applied DC voltage. Both terms are linear in V_{DC} and are zero when $V_{\text{DC}} = -V_0$, i.e. when the contact potential difference is compensated. We have checked that this is true by sweeping the DC voltage while measuring S_{ω_1} and Δf_{ω_1} . Both lines should be linear and cross zero at the same point. The result is shown in Figure 7.4. These data were obtained at room temperature between the gold sphere and plate separated by roughly $1 \mu\text{m}$. During the sweep we applied an AC voltage of $1 V_{\text{pp}}$. The results are indeed linear in V_{DC} and both signals are zero around the same DC voltage, although a slight offset exists. The FM signal decreases faster with distance than the QS signal. At the relative large distance of $1 \mu\text{m}$, it is therefore not surprising that it is more influenced by noise. Note that even between two gold surfaces at room temperature, we detect a contact potential difference of 61 mV. This is probably caused by different circumstances in the coating process and/or the different substrates.

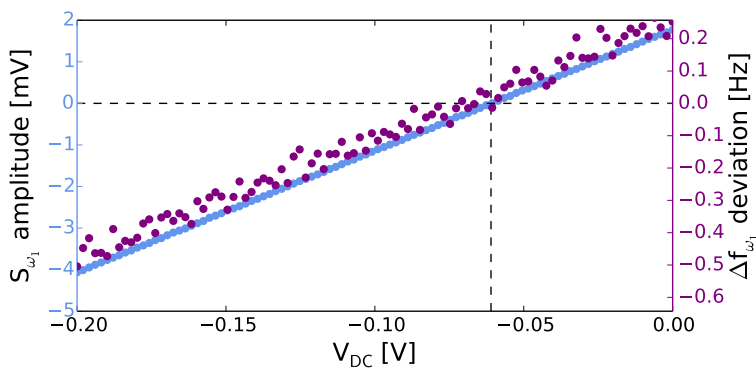


Figure 7.4: The QS and FM signals at ω_1 as a function of the DC voltage; S_{ω_1} (blue) and Δf_{ω_1} (purple). Both signals are linear in V_{DC} and cross zero at the same DC voltage, indicating a contact potential difference of 61 mV between two gold surfaces.

Knowing V_0 , we can simply set V_{DC} at the start of a measurement. But since V_0 can change over time during a measurement, we create a feedback loop keeping either S_{ω_1} or Δf_{ω_1} zero. In Figure 7.5 we show the output DC voltage from the feedback loop during a measurement run, as well as the remaining potential difference calculated from S_{ω_1} .

The contact potential difference is fed back up to only a few millivolts during the

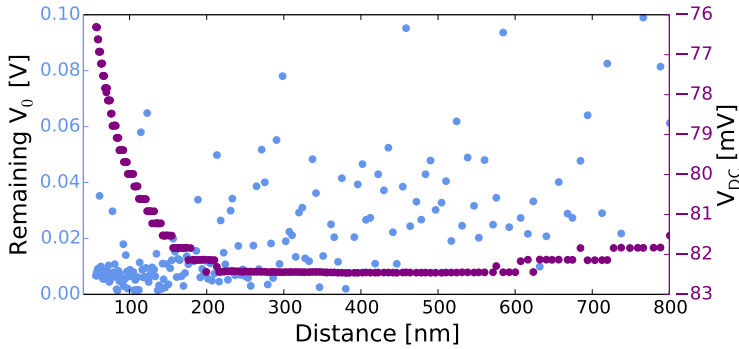


Figure 7.5: Result of the electrostatic compensation scheme. From the quasi-static signal S_{ω_1} can be calculated that the surface potential V_0 is successfully reduced. The remaining potential as a function of distance is shown in blue. The output DC voltage (purple), equal to $-V_0$, changes as a function of distance.

whole measurement run. However, there is a clear distance-dependence of the output DC voltage. This would suggest that the mean surface potential V_0 is distance-dependent, but it is only determined by the material properties. There are several possible explanations for the behaviour in our measurements. One is the presence of another conductor, for example the cantilever or the sample mount, that is gradually shielded during approach [163]. Another explanation is the influence of variations in the surface potential, which leads to an electrostatic force with a different distance-dependence than following from the mean surface potential [164, 165]. The presence of this extra force shows that compensating for V_0 only at a far away distance is not sufficient and that a real-time compensation scheme is clearly needed.

Apart from compensation, the electrostatic force is used to calibrate the force sensitivity of the set-up and the distance between the sphere and the plate. As described in the previous section, we use a fiber interferometer positioned above the plate to determine the distance the plate moves during one measurement run, d_{pz} . The sphere-plate distance is equal to $d = d_0 - d_{pz}$. The initial separation d_0 is obtained from a fit to the electrostatic signals at $2\omega_1$. Instead of fitting $S_{2\omega_1}$ directly, we rewrite Eq. 7.10 as $V_{AC}^2/(2S_{2\omega_1}) = (d_0 - d_{pz})/\kappa$, which is linearly dependent on d_{pz} . Similarly, we can rewrite Eq. 7.15 as $V_{AC}/\sqrt{2\Delta f_{2\omega_1}} = (d_0 - d_{pz})/\sqrt{\mu}$. The data from a typical measurement run based on the QS signals is shown in Figure 7.6(a), and based on the FM signals in Figure 7.6(b). The fits follow the data, especially at large d_{pz} where the distance between the sphere and the plate is smallest and the electrostatic force is largest. From the fit we can determine an offset distance $d_0 = 832$ nm which we can use to deduce the actual sphere-plate distance.

From the slope of the fit in Figure 7.6(a) we can determine the force sensitivity $\kappa = 1.69 \times 10^{-8} \text{ m V}^{-1}$. This value is close to the expected value of $\kappa = 2 \times 10^{-8} \text{ m V}^{-1}$ based on the values $k = 0.9 \text{ N/m}$, $R = 100 \mu\text{m}$ and $\gamma = 7 \text{ MV/m}$. The difference is caused in uncertainties in the spring constant and/or sphere radius. The interferometric sensitivity γ can be determined separately from the cantilever interferometer

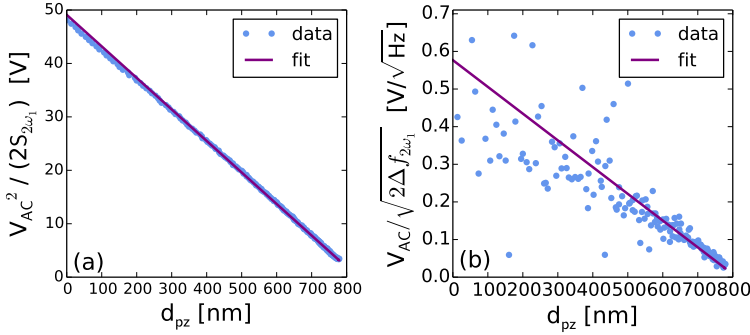


Figure 7.6: Data (blue dots) and fit (purple line) used to find the offset distance d_0 from the modulated electrostatic force: (a) $V_{AC}^2 / (2S_{2\omega_1})$ as a function of the distance change d_{pz} ; (b) $V_{AC} / \sqrt{2\Delta f_{2\omega_1}}$ as a function of the distance change d_{pz} .

signal as a function of the laser frequency. The system parameter μ is found from the fit in Figure 7.6(b), $\mu = 1.98 \times 10^{-12} \text{ Hz m}^2 \text{ V}^{-2}$, close to the calculated value of $3.55 \times 10^{-12} \text{ Hz m}^2 \text{ V}^{-2}$.

Once we know these parameters, we can determine the distance from the ratio between either $S_{2\omega_1}$ or $\Delta f_{2\omega_1}$ and the AC voltage V_{AC} :

$$d = \frac{\kappa V_{AC}^2}{2S_{2\omega_1}} = \sqrt{\frac{\mu V_{AC}^2}{2\Delta f_{2\omega_1}}}. \quad (7.16)$$

This approach is preferable, because it is less sensitive to noise in our plate interferometer. It also allows us to set the distance by applying a certain AC voltage and creating a feedback loop that moves the piezo-electric transducer until the corresponding electrostatic force signal (either $S_{2\omega_1}$ or $\Delta f_{2\omega_1}$) is reached. This way it is possible to reach a certain distance by simply setting the AC bias voltage. We typically do one measurement run with an educated guess for either κ or μ , then we determine the correct values for κ and μ from the fits such that we can set the desired distances for the following runs. It is even possible to do a measurement run where we keep the distance fixed at one value. This allows us to directly measure the effect of the superconducting transition by sweeping the temperature across the critical temperature, without the influence of drift or thermal expansion.

7.2.1 Validity of the proximity force approximation

As mentioned before, our calibration scheme is based on an approximation of the electrostatic force. Here we will check the validity of this approximation by comparing it to the full electrostatic force. From the self-capacitance of the sphere and plate and their mutual capacitance it is possible to find a complete expression [166]:

$$F_{ES} = 2\pi\epsilon_0 V^2 \sum_{n=1}^{\infty} \frac{\coth(\alpha) - n \coth(n\alpha)}{\sinh(n\alpha)} \quad (7.17)$$

with $\alpha = \text{arccosh}(1 + d/R)$. We approximated the infinite sum by taking the first 100.000 terms. Within the precision of our calculations, we could see no change when more terms were taken into consideration.

It is possible to calculate the sum at several distances and calibrate our measurement with (an interpolation of) the full electrostatic theory. But this may be an unnecessarily complex method if a more simple expression is also valid. For practical purposes, we use the expression given in Eq. 7.5. This expression is obtained via the Proximity Force Approximation (PFA) [136–138] that relates the force in a sphere-plate geometry (F_{sp}) to the free energy per unit area in a parallel-plate geometry (U_{pp}):

$$F_{\text{sp}}(d, R) \approx 2\pi R U_{\text{pp}}(d). \quad (7.18)$$

From the energy per unit area of two infinite parallel conducting plates, $U_{\text{pp}}(d) = \varepsilon_0 V^2/2d$, we deduce the expression given in Eq. 7.5. It must be noted, however, that the PFA only holds under two conditions: the interaction energy must be localized and the distance of closest approach must be small compared to the sphere radius ($d \ll R$). In our set-up we have a $100 \mu\text{m}$ radius sphere at a distance of less than $1 \mu\text{m}$ from the plate. So the condition is only met up to 1%. To see if this indeed leads to errors in our measurements, we look at the QS electrostatic signal $S_{2\omega_1}$ as a function of distance. During a typical measurement run we keep this signal constant in a feedback loop that adjusts the distance to match a given AC voltage. There should therefore be a linear dependence between V_{AC}^2 and the distance as long as the electrostatic approximation holds. In Figure 7.7 we show data obtained during a typical Casimir force measurement run. The black dots show the applied AC voltage as a function of distance. The two lines indicate the calculated AC voltage based on experimental parameters, either using the approximation or the full theory. The purple line is derived from the approximation according to

$$V_{\text{AC,approx}}^2 = \frac{2kdS_{2\omega_1}}{\gamma\varepsilon_0\pi R}. \quad (7.19)$$

The distance here is derived with our calibration method based on the approximated expression for the electrostatic force. The blue line is obtained using the full electrostatic force and is given by

$$V_{\text{AC,full}}^2 = \frac{kS_{2\omega_1}}{\gamma\pi\varepsilon_0} \left(\sum_{n=1}^{100.000} \frac{\coth(\alpha) - n \coth(n\alpha)}{\sinh(n\alpha)} \right)^{-1}. \quad (7.20)$$

In both calculations we have used the measured value of $S_{2\omega_1}$. The ratio k/γ is derived from the calibration of κ , with the value $R = 100 \mu\text{m}$. The sum is calculated for 2000 distances between $d = 100 \text{ nm}$ and $10 \mu\text{m}$ and then interpolated with the distances from our measurement.

From the overlap in Figure 7.7(a) it is clear that both the full electrostatic force and the approximation describe our data well within the measurement fluctuations. This is even better visible in the residuals between the data and the two calculations shown in Figure 7.7(b). The two calculations start to deviate from each other at a distance larger than 700 nm , which shows the limits of the PFA. But it is clear that we can safely use the approximated electrostatic force for our calibration scheme.

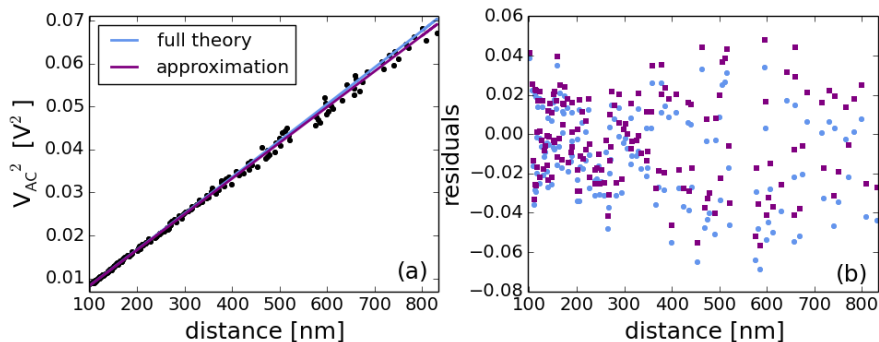


Figure 7.7: Comparison of electrostatic force approximation with full theory: (a) V_{AC}^2 as a function of distance, both measured experimentally (black dots) and calculated from either the full electrostatic force (blue line) or its approximation (purple line). Any deviation from linear dependence shows that the approximation no longer holds; (b) Residuals of the measurements in (a) show negligible deviation compared to the fluctuations in the measurement.

7.3 Casimir force measurements

In the previous section we described how we use the electrostatic force to compensate the contact potential difference and to set the distance at a fixed value. We mentioned that this calibration scheme operates simultaneously with our Casimir force measurements. The Casimir force gradient itself is obtained from the static frequency shift Δf_s given by Eq. 7.13. When V_0 is compensated, the middle term on the right hand side in this equation is zero. The other terms can be rewritten to give the Casimir force gradient, normalized to the sphere radius:

$$\frac{1}{R} \frac{\partial F_C}{\partial d} = \frac{\epsilon_0 \pi}{\mu} [\Delta f_{2\omega_1} - \Delta f_s]. \quad (7.21)$$

Via the proximity force approximation we can compare this to theoretical computations of the Casimir force in the parallel-plate geometry, since the measured, normalized, Casimir force gradient only differs a factor 2π from the calculated pressure.

The result of one of our measurement runs between two gold surfaces at room temperature is shown in Figure 7.8. During this run the distance feedback was active, setting the distance at 200 logarithmically distributed values between 800 nm and 56 nm. The feedback was set on the quasi-static signal $S_{2\omega_1}$, with set-point 0.5 mV_{rms} and based on a force sensitivity $\kappa = 1.69 \times 10^{-8} \text{ m V}^{-1}$. This set-point corresponds to a force amplitude at $2\omega_1$ of 0.1 nN. A second feedback loop was set to minimize S_{ω_1} by applying a DC voltage of about 80 mV, this value changed with distance.

The calculation shown in the same plot is done according to the Lifshitz theory using the Drude model for the reflectivity of the gold surfaces [112]. For an explanation of these calculations we refer to chapter 5. There may be slight deviations due

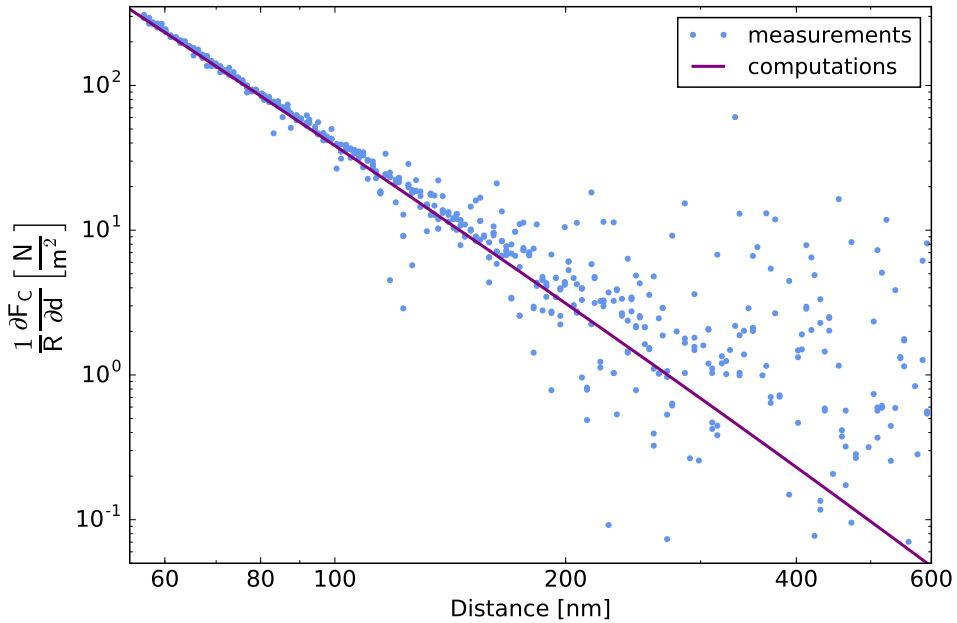


Figure 7.8: Casimir force gradient, normalized to the sphere radius, between a sapphire plate coated with 150 nm gold and a $100\ \mu\text{m}$ radius sphere with a 200 nm gold coating. The measurement was performed at room temperature with a background pressure of 2.2×10^{-1} mbar. The good overlap between calculations and measurements shows that we can reliably measure the Casimir force with a method based on simultaneous calibration with the electrostatic force.

to surface roughness or the specific optical properties of our samples. Also the calculated Casimir force would be somewhat larger if it was based on the plasma model. However, these deviations will be less than a percent compared to the calculations shown in the figure. This is still within the precision of our measurements which is of the order of several percent.

From the good overlap between experiment and theory it is clear that our set-up is capable of detecting the Casimir force gradient between two gold surfaces in a sphere-plate geometry. It is also clear that there persist no systematic errors in our set-up, at least no errors larger than the measurement fluctuations of order $1\ \text{N/m}^2$. This means that with our electrostatic force calibration scheme, we can reliably measure the Casimir force gradient in the range 50 – 200 nm. This scheme also allows us to measure the temperature dependence directly by setting the distance at a certain value and keeping it fixed while we sweep the temperature. The next step is to exchange the gold coated plate for a plate coated with a superconductor.

Dependence of the Casimir Force on the Dielectric Permittivity of NbTiN

The magnitude of the Casimir force is determined by circumstances like the geometry of the system and the closest distance between the surfaces. Another important factor is the reflectivity of the surfaces. The reflectivity of the material can be determined via optical reflection measurements, and can be used to calculate the Casimir force via the method described in chapter 5. We have followed these steps to compute the force between a gold sphere and a superconducting plate. These calculations show very good agreement with Casimir force measurements obtained at room temperature.

The exact calculation of the Casimir force between real materials requires full knowledge of the complex dielectric permittivity of the materials [97, 98]. At high frequencies, we can rely on the measured optical spectra, but these are available only in a certain frequency range. At low frequencies, it remains uncertain whether to include Ohmic dissipation in the calculation of the Casimir force or not. Since dissipation is not present in superconductors, it has been proposed [49, 55] to measure the Casimir force between superconducting materials. Comparison of the Casimir force below and above the critical temperature may give insight into the low frequency contribution of the dielectric permittivity.

Measurements of the Casimir force gradient between a gold coated sphere with radius $R = 100 \mu\text{m}$ and a 150 nm thick gold layer on a sapphire substrate were shown in chapter 7. In that chapter we described our measurement method in detail, we will therefore not elaborate on that in this chapter. Here we will show the results obtained by exchanging the gold coated sapphire plate by a SiO_2 plate coated with a 200 nm thick layer of niobium titanium nitride (NbTiN), which is a superconductor below its critical temperature of 13.6 K. The Casimir force is measured as a function of distance at two different temperatures, below and above the critical temperature, and as a function of temperature at a distance of 83 nm. We detect no large influence of the superconducting transition on the strength of the Casimir force.

8.1 Casimir force computed from the measured optical spectrum of NbTiN

In chapter 7 we demonstrate the accurate calibration of our system by comparing measurements with calculations of the Casimir force between two gold surfaces. To compute the Casimir force, we used optical reflection measurements of gold [112]. Extrapolation to frequencies where these data are incomplete can be done based on the Drude or on the plasma model, using the plasma and relaxation frequencies that can be obtained from a fit to the optical reflection data. We are interested in the Casimir force between gold and NbTiN, but a comparison with computations could not directly be obtained due to the lack of optical reflection data on NbTiN in literature [167]. We therefore sent our NbTiN sample to Erik van Heumen from the optical spectroscopy lab at the University of Amsterdam [168], who measured the optical spectrum between 1 cm^{-1} and $60\,000 \text{ cm}^{-1}$ (between $1.89 \times 10^{11} \text{ rad/s}$ and $1.13 \times 10^{16} \text{ rad/s}$). The dielectric permittivity of our sample was calculated via a fit of the reflection data and its real and imaginary part are shown in Figure 8.1. The optical spectrum was measured at room temperature and at lower temperatures, since the spectrometer is combined with a cryostat. Figure 8.1 also shows the permittivity at 16 K, the base temperature of that cryostat.

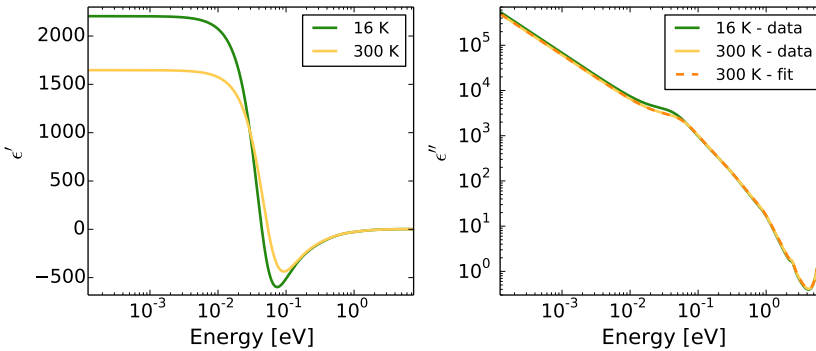


Figure 8.1: Dielectric permittivity of NbTiN as a function of frequency, measured at the optical spectroscopy lab at the University of Amsterdam, both at room temperature and at 16 K: (a) Real part; (b) Imaginary part, a fit to the room temperature spectrum based on the Drude model combined with Lorentz oscillators is also shown.

Extra resonances resulting from the restoring force that binds the core electrons to the nuclei [116] are visible in the spectra. A fit to the imaginary part of the spectrum, shown in Figure 8.1(b) for the room temperature data, based on the imaginary part of the Drude-Lorentz model,

$$\epsilon''_{\text{DL}}(\omega) = \frac{\Omega_p^2 \gamma}{\omega(\omega^2 + \gamma^2)} + \sum_j^K \frac{f_j \beta_j \omega}{\beta_j^2 \omega^2 + (\omega_{0j}^2 - \omega^2)^2}, \quad (8.1)$$

yielded $K = 4$ resonances with resonance frequencies ω_{0j} at 0.059 eV, 0.88 eV, 2.4 eV and 6.2 eV respectively. Their oscillator strengths f_j and damping rates β_j were also found, as well as values for the plasma frequency $\Omega_p = 43\,000\text{ cm}^{-1} \approx 5.33\text{ eV}$ and relaxation rate $\gamma = 3750\text{ cm}^{-1} \approx 0.465\text{ eV}$ at room temperature and $\gamma = 3350\text{ cm}^{-1} \approx 0.415\text{ eV}$ at 16 K. Based on these values, the dielectric permittivity at imaginary frequencies is given by the Drude-Lorentz model

$$\varepsilon_{\text{DL}}(i\xi) = 1 + \frac{\Omega_p^2}{\xi(\xi + \gamma)} + \sum_j \frac{f_j}{\omega_{0j}^2 + \xi^2 + \beta_j \xi}, \quad (8.2)$$

or by the generalized plasma model

$$\varepsilon_{\text{gp}}(i\xi) = 1 + \frac{\Omega_p^2}{\xi^2} + \sum_j \frac{f_j}{\omega_{0j}^2 + \xi^2 + \beta_j \xi}. \quad (8.3)$$

For comparison, we also integrate the imaginary part of the dielectric permittivity via the Kramers-Kronig relations (see Eq. 5.12), after we extrapolate the data to lower and higher frequencies according to the Drude model. This should lead to the same dielectric permittivity at imaginary frequencies as described by the Drude-Lorentz model.

From these dielectric permittivities, the reflectivity of the surfaces is then determined via the Fresnel equations. The Casimir pressure between gold and NbTiN is found by putting in the appropriate reflectivities in Eq. 5.11. Finally, to compare the calculated parallel plate pressure with our measurements of the Casimir force gradient in the sphere-plate geometry, we use the proximity force approximation [137, 138].

8.1.1 Comparison to room temperature measurements

For a detailed description of the set-up and measurement scheme, we refer to chapters 6 and 7. The room temperature data shown here were obtained with the following settings. Compensation of the contact potential difference V_0 was done via the FM side-bands at ω_1 . We first performed a measurement run based on an educated guess of the system parameter μ . From the fit to the frequency deviation $\Delta f_{2\omega_1}$ as a function of separation we determined a value $\mu = 1.9 \times 10^{-12}\text{ Hz m}^2\text{ V}^{-2}$, close to the calculated value of $3.6 \times 10^{-12}\text{ Hz m}^2\text{ V}^{-2}$ based on values of $f_0 = 2.3\text{ kHz}$, $R = 100\text{ }\mu\text{m}$ and $k \approx 1\text{ N/m}$. During the measurements shown here the distance was set by a feedback loop that adjusted the piezo-electric transducer under the plate until the set-point at the $2\omega_1$ FM side-bands was reached, via the relation

$$d = \sqrt{\frac{\mu V_{\text{AC}}^2}{2\Delta f_{2\omega_1}}}. \quad (8.4)$$

The set-point was $\Delta f_{2\omega_1} = 0.54\text{ Hz}$, corresponding to a force gradient modulation with an amplitude of $4.7 \times 10^{-4}\text{ N/m}$ at the frequency $2\omega_1$.

The room temperature measurements shown here were obtained in the same cryostat as the low temperature measurements shown later in this chapter. The

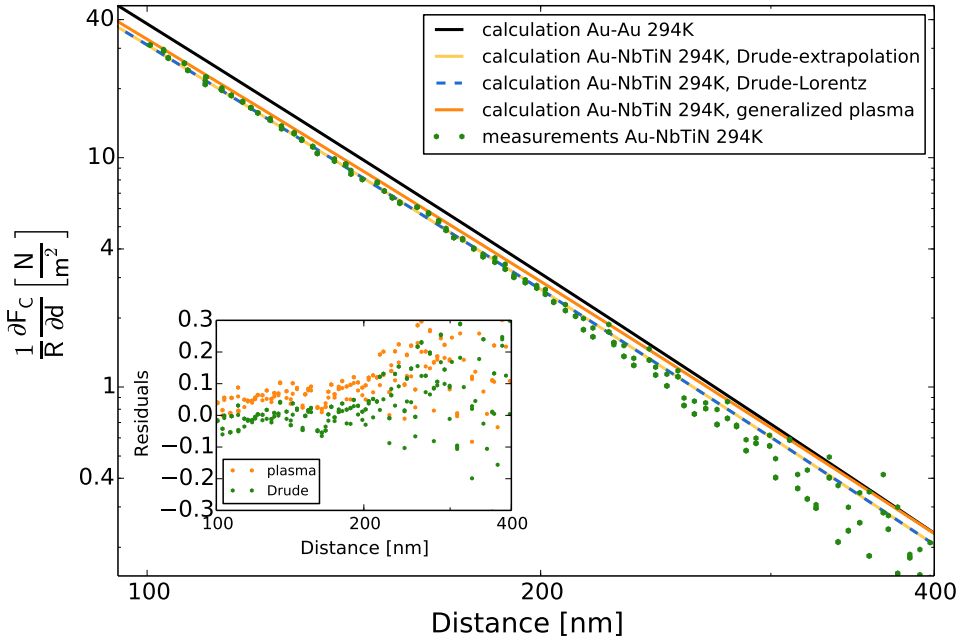


Figure 8.2: Measured Casimir force gradient, normalized to the sphere radius, between a gold coated sphere and a NbTiN thin film at room temperature (green dots). The lines indicate calculations of the Casimir force gradient at room temperature, between two gold surfaces (black line) and between gold and niobium titanium nitride. Three methods, discussed above, were used to determine the dielectric permittivity for NbTiN at imaginary frequencies: the Drude model based on extrapolation of the data (yellow line), the Drude-Lorentz model (blue dashed line) and the generalized plasma model (orange line). The good overlap between the calculations and measurements in general shows our control of the measurement as well as our ability to base calculations on actual optical reflection data. Compared to the calculations between two gold surfaces there is a decrease of about twenty percent in the force gradient between gold and NbTiN. The inset shows the difference between the calculations and data for the Drude-Lorentz and generalized plasma models, normalized to the model values.

background pressure in the cryostat was 6.2×10^{-2} mbar. A four stage mass-spring system, in fact the mechanical equivalent of an electrical wave filter [94, 169], was used to isolate the set-up from vibrational noise. To check that the data are not accidentally influenced by the surroundings, we have repeated our measurements in different circumstances. The same results were obtained in a different cryostat, with a different gold coated sphere, a different NbTiN plate and with the distance lock and electrostatic compensation done via the quasi-static signals.

The green dots in Figure 8.2 show the Casimir force gradient normalized to the sphere radius measured at room temperature. The lines show calculations of the normalized Casimir force gradient at room temperature. The dielectric permittivity of NbTiN at imaginary frequencies is determined via the three methods described above: via extrapolation of the optical data using the Drude model (yellow line), via the Drude-Lorentz model accounting for resonances in the material (blue dashed line) and via the generalized plasma model (orange line). The first two methods lead to the same Casimir force gradient, as can be expected. Using the generalized plasma model results in a stronger force gradient, at small separation the deviation is about five percent. This is significantly more than between two gold surfaces (compare Figure 5.4). As already explained in chapter 5, due to the higher resistance of NbTiN compared to gold, the two models diverge already at a higher frequency. The two models lead to different contributions to the Casimir force not only at the zero Matsubara frequency, but at higher order Matsubara frequencies as well. At room temperature, at the first eight or nine Matsubara frequencies the two models predict different contributions, while about a hundred frequencies contribute in total. Measuring the Casimir force between high resistive materials therefore seems a prudent way to distinguish between the Drude and plasma models [170].

If we compare our data with our calculations between gold and NbTiN, we notice the good general overlap. Note that the lines are not fits and that the measurements and calculations were obtained in two completely independent ways. The overlap shows both our control and good calibration of the measurements and our ability to base Casimir force calculations on measured optical spectra. Taking a closer look at the overlap between the data and the computations based on the plasma and Drude models, we observe that the data seem to coincide better with the Drude model than with the plasma model. This is illustrated by the inset in Figure 8.2, which shows the difference between the data and Drude-Lorentz model (green dots) and between the data and generalized plasma model (orange dots), normalized to the values calculated by the models. This shows that for distances up to 200 nm, the data deviate $6.2 \pm 2.8\%$ from the plasma model and $0.4 \pm 2.7\%$ from the Drude model. This is just one measurement run, but other data runs show the same trend. Note that in general, the presence of an extra (electrostatic) force that is not calibrated in the experiments may lead to an overestimation of the Casimir force [165], an underestimation of the force is less likely [107]. More extensive data analysis, combined with more measurements, is required to draw a more definitive conclusion.

When we compare our data and calculations with calculations between two gold surfaces at room temperature (black line in Figure 8.2, equal to the line in Figure 7.8), we notice that the force between gold and NbTiN is twenty percent weaker than between two gold surfaces. This is a direct result of the smaller dielectric permittivity

of NbTiN. A decrease of twenty percent is substantial, different metallic surfaces produce nearly the same Casimir force [98]. For comparison, the Casimir force between gold and indium tin oxide (ITO), which is transparent in a large frequency range, reduces the force by about 40-50% [144].

Since the Drude model accounts correctly for Ohmic resistivity, it would seem more prudent to base calculations of the Casimir force on this model. However, certain measurements coincide better with the plasma model description that does not take Ohmic dissipation into account [11, 52, 107, 124]. These measurements were obtained at short distances, where the difference between the two models is relatively small. Measurements at a larger separation on the other hand have indicated a better accordance with the Drude model [50]. To our knowledge, the measurements shown in this chapter are the first that demonstrate a better overlap with the Drude model description at small separation.

8.2 Low temperature measurements

The measurements were repeated at 13.9 K, just above the critical temperature, such that the NbTiN is not yet superconducting. The orange squares in Figure 8.3 show these results. These data were obtained in the same circumstances as the room temperature measurements, except that the electrostatic compensation and distance lock were set on the quasi-static signals (set-point $50 \mu\text{V}_{\text{rms}}$, or 0.7 nN amplitude). Although the FM side-bands were not stable enough to be used for feedback, they were still recorded. A value for the system parameter could be determined as $\mu = 2.4 \times 10^{-12} \text{ Hz m}^2 \text{ V}^{-2}$. The small change compared to the room temperature value can be explained by a change in spring constant. This is also apparent in the resonance frequency, which shifts 60 Hz upwards from room temperature to low temperatures.

At low temperature, the Casimir force gradient has increased significantly compared to room temperature. We can even deduce an increase of the order of twenty percent. This cannot be an effect of the thermal Casimir force [50, 97], which is only a fraction of the zero-point contribution even at room temperature. Another explanation would be the change in the optical reflectivity of the surfaces. The reflectivity of gold is slightly temperature dependent [171, 172], but this influence is negligible [120]. The low temperature dielectric permittivity of NbTiN is measured and shown in Figure 8.1. Based on this optical spectrum we calculate via the Drude-Lorentz model the expected Casimir force at 16 K, equal to the temperature at which the optical spectrum of NbTiN was obtained. Figure 8.3 shows the result, denoted by the blue line. If we overlap the calculated Casimir force gradient at 16 K with the calculations at room temperature (the blue dashed line in Figure 8.3), we see that the force gradient differs only slightly between the two temperatures. It is clear that the change in reflectivity cannot account for the change in Casimir force gradient. Also if we base our calculations on the generalized plasma model, as indicated by the yellow line in Figure 8.3, the increased Casimir force gradient cannot be explained.

The black line shows the Casimir force gradient between two gold surfaces at 16 K, from the overlap between this line and the data, it would almost seem that the

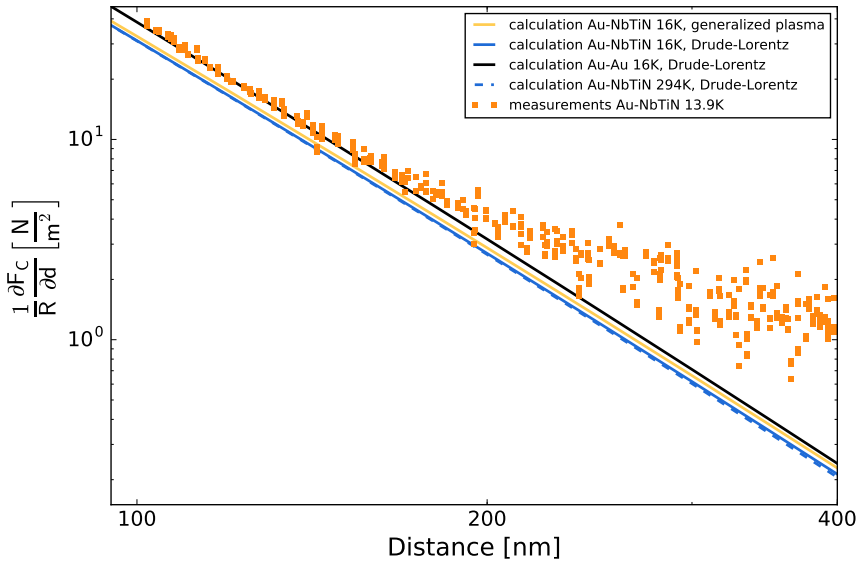


Figure 8.3: Casimir force gradient, normalized to the sphere radius, between a gold coated sphere and a NbTiN thin film measured at 13.9 K (orange squares). The solid lines indicate calculations of the Casimir force between gold-gold and gold-niobium titanium nitride at 16 K, based on the Drude-Lorentz model (blue line) as well as on the generalized plasma model (yellow line). The blue dashed line shows the calculated Casimir force gradient between gold and NbTiN at room temperature (equal to the yellow line in Figure 8.2). It is remarkable that the data overlap best with the calculations between two gold surfaces (black line), since we would expect an overlap with the calculated force gradient between gold and NbTiN (blue or yellow line).

NbTiN surface appears metallic for the Casimir force. To confirm these measurements, we repeated these measurements at temperatures between 9.3 K and 22 K, and at different cool-down runs. All these low temperature data overlap within our measurement error. This effect of increased Casimir force gradient should therefore begin at higher temperatures. It would be interesting to repeat our experiments in the temperature regime between 22 K and room temperature. If we take a look at low temperature measurements reported in literature, comparison between measurements at room temperature and at 77 K show no discrepancy [54]. Measurements at 4 K did report a ten percent difference, but ascribed it to an outdated system calibration [51].

We have no explanation for the increase in the detected Casimir force gradient at low temperatures. It may still have a technical cause. However, our room temperature calibration measurements between two gold surfaces (see Figure 7.8), as well as the good overlap between theory and our room temperature gold-NbTiN measurements (Figure 8.2) show that our measurement scheme is well capable of calibrating the sphere-plate distance and the sensitivity of our force sensor. For a conclusive

indication of the validity of our calibration scheme at low temperatures we would need to precede our low temperature Casimir force measurements between a gold sphere and NbTiN plate with calibration measurements between the sphere and a gold plate, during the same cool-down and under the same circumstances.

We are ultimately interested in the effect of the superconducting transition to the Casimir force. Since this results in a relative change, an absolute calibration of our set-up does not seem to be a strict requirement. The room temperature measurements convince us that we are indeed capable of measuring the Casimir force. However, we need to be cautious to ascribe any change across the superconducting transition to a change in the Casimir force.

8.2.1 The effect of superconductivity

In chapter 5 we discussed that measuring the Casimir force between superconductors may give insight in the uncertain contribution of the dielectric permittivity at low frequencies. The dielectric permittivity of a superconductor differs from the normal state in two ways. First is that static magnetic fields are expelled. Another change is the opening of the superconducting gap at high frequencies, which leads to a zero resistivity of the material. Both effects may have measurable impact on the Casimir force. These effects become greater when the temperature approaches 0 K. It is therefore optimal to measure the force over a large temperature range below the critical temperature, but unfortunately the base temperature of our cryostat was limited to 9.3 K. However, our measurements still allow us to impose an upper limit on the effect of superconductivity on the Casimir force.

In Figure 8.4 we show the normalized Casimir force gradient as a function of distance measured just below (9.3 K) and just above (13.9 K) the critical temperature of our NbTiN plate (13.6 K). The data were obtained during the same cool-down under equal circumstances. For both measurements, the electrostatic compensation of the contact potential difference V_0 was done via the quasi-static signal S_{ω_1} . The distance lock was set on the quasi-static signal $S_{2\omega_1}$ with a set-point of $50 \mu V_{\text{rms}}$ corresponding to a force modulation with an amplitude of 0.6 nN at the frequency $2\omega_1$, based on a spring constant of 1 N/m and interferometric read-out sensitivity of 125 kV/m. The force sensitivity, deduced from the fit to $S_{2\omega_1}$ as a function of separation, had a value of $\kappa = 2.56 \times 10^{-10} \text{ m V}^{-1}$ at 9.3 K and $\kappa = 2.48 \times 10^{-10} \text{ m V}^{-1}$ at 13.9 K. The difference can be explained by a small deflection of the cantilever that is caused by the change in temperature, which in turn causes a change in the interferometric read-out sensitivity γ .

The calculation of the Casimir force between two gold surfaces at 16 K is also depicted in Figure 8.4 as a guide to the eye. The choice for this calculation is motivated by the low temperature results shown above. At distances larger than 200 nm the data points start to deviate towards our measurement precision of 1.5 N/m^2 .

The Casimir force measurements below the critical temperature overlap with the measurements above the critical temperature, at least within our measurement accuracy. We can therefore conclude that there is no significant influence of the superconducting state. There is definitely no new, unexpected effect that has a significantly greater influence on the Casimir force than what we predicted based on the

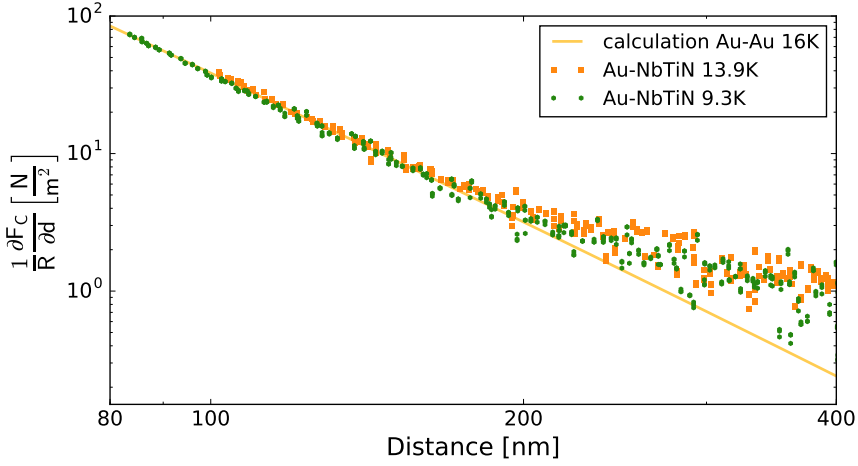


Figure 8.4: Casimir force gradient, normalized to the sphere radius, between a gold coated sphere and a NbTiN thin film as a function of distance. The film was in a superconducting state at 9.3 K (green dots) and in a normal state at 13.9 K (orange spheres). Within our measurement accuracy we can set an upper limit of about seven percent on the effect of superconductivity to the Casimir force.

possible change in reflectivity of the superconductor. To make this statement more quantitative, we take a closer look at the force at a distance of 120 nm. Values for the normalized force gradient are indicated in Table 8.1. From these values we can deduce that the effect of the superconducting state is less than seven percent.

Temperature	Normalized force gradient
9.3 K	$20.9 \pm 1.5 \text{ N/m}^2$
13.9 K	$21.8 \pm 1.2 \text{ N/m}^2$

Table 8.1: Casimir force gradient, normalized to the sphere radius, between a gold coated sphere and a NbTiN plate at a distance of 120 nm at two different temperatures, just below and just above the critical temperature of the plate.

Since the precision of 1.5 N/m^2 is constant over distance, we can improve on this limit by measuring at a smaller separation. Our measurement method allows us to keep the distance fixed even when circumstances like the temperature change. It is therefore possible to do a temperature sweep of the Casimir force gradient. Since we monitor the plate conductance simultaneously, we can directly indicate the superconducting transition in our measurements. These measurements are shown in Figure 8.5. Since the cantilever may deflect as the temperature changes, the interferometric read-out sensitivity γ can change, which will influence the force sensitivity κ . It is therefore not possible to set the distance lock on the QS signal $S_{2\omega_1}$. We set it instead on the FM side-band $\Delta f_{2\omega_1}$, with a set-point of 1 Hz ($8.7 \times 10^{-4} \text{ N/m}$). The sys-

tem parameter was determined from a previous measurement of the Casimir force gradient as a function of distance and was found to be $\mu = 2.22 \times 10^{-12} \text{ Hz m}^2 \text{ V}^{-2}$. We set the AC bias voltage between the sphere and the plate such that the PI feedback loop will set the distance to 83 nm. Note that a deviation in the distance of about 1.5% will result in a variation in the measured force gradient of about 6%. With resistance heaters in the cryostat we sweep the temperature. During the run the temperature was increased from 10.2 K to 14.5 K before the heaters were switched off again, lowering the temperature to 10.4 K. The output of the resistance bridge that monitors the plate resistance (described in chapter 7) is shown in Figure 8.5(a). The green dots show the data during the temperature increase, the data obtained during the downward sweep are depicted in orange. The superconducting transition occurred at a value of 12.5 K on the plate thermometer. This is lower than the expected critical temperature of 13.6 K. The difference can be caused by a larger temperature gradient between the thermometer and plate due to a higher heating rate than we used to determine the critical temperature in chapter 7. Since we determine the superconducting transition based on the plate's resistance and not on the temperature, this is not an issue.

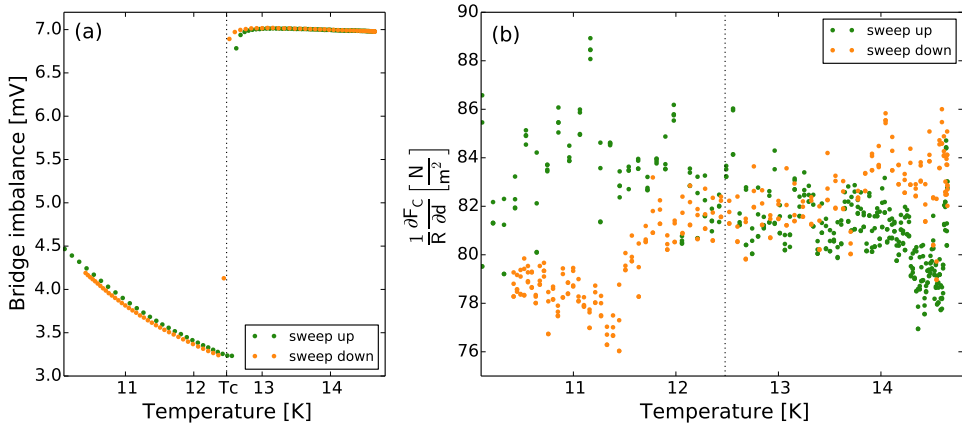


Figure 8.5: Temperature dependency of the Casimir force: (a) The simultaneous resistance measurement of the plate detects the superconducting transition at a temperature of 12.5 K; (b) Casimir force gradient at a distance of 83 nm as a function of temperature, the superconducting transition is indicated by the dotted vertical line.

The normalized Casimir force gradient as a function of temperature is shown in Figure 8.5(b). The sweep up is indicated in green, the downward sweep in orange. The superconducting transition is indicated by the dotted line. Above the critical temperature the Casimir force gradient, normalized to the sphere radius, is equal to $81 \pm 2.1 \text{ N/m}^2$. The expected change with temperature, based on the theory developed in chapter 5, depends on which model is used to extrapolate the dielectric permittivity. If we use the (generalized) plasma model, we expect no temperature dependence. The Drude-Lorentz model predicts an increase of the force as the tem-

perature is lowered, of about 5% between the critical temperature and $T \ll T_c$. This number is an overestimation since we use the two-fluid model for our prediction, which does not account for impurity scattering [134]. Since we only measure at temperatures around T_c , and not at $T \ll T_c$, the force should not have increased maximally yet. But we can still expect a change of 3.4% between our data at the lowest temperature and above the critical temperature when the low frequency permittivity of the normal state of NbTiN is described by the Drude model instead of the plasma model.

If we look at the data in Figure 8.5(b), we see no such increase in the force below the critical temperature. It seems that two branches appear below 12 K, but a similar deviation is visible above 14 K. We are not sure what causes this effect, but we do not exclude that it is caused by small fluctuations in the distance. The deviations in the measured force gradient of about 5 N/m^2 can be explained by an imprecision in the distance of about 1.3 nm at 83 nm. We need to repeat this measurement after minimizing the effect of noise in our distance lock in order to give a more conclusive answer to the effect of the superconducting transition on the Casimir force.

If we compare our accuracy of 2.1 N/m^2 to the average force gradient that we measured, we can set an upper limit of 2.6% of the influence of the superconducting state to the Casimir force. This is in the same order of magnitude as the maximally expected effect obtained from calculations based on the Drude-Lorentz model. Recall that the plasma model predicts no measurable changes. Although, at first glance our upper limit seems to be smaller than the effect predicted by the Drude model, we must be careful to draw conclusions. The estimation is likely to be too large, as was mentioned above. Furthermore, we cannot guarantee that the distance is fixed within 0.2 nm at 83 nm, such that changes in the force of the order of a percent cannot be ascribed to or concealed by changes in the distance.

There is another effect that may lessen the effect of the superconducting state. The Casimir force is mostly determined by the surface modes of the material [36, 173], as it depends on the penetration depth of the electromagnetic fields. Very simply put, the bulk properties are screened by the surface. This penetration depth varies with frequency and depends on the plasma and relaxation frequencies, we estimate it to be of order 100 nm. Superconductors, on the other hand, are characterized by their coherence length ξ_0 . This length can be interpreted as the distance from the surface over which the density of superconducting Cooper pairs recovers to the bulk value assumed in our calculations [174]. This means that at the surface, up to the coherence length, the material cannot be considered as a full superconductor. The effect of the superconducting state on the Casimir force can only be measured if the coherence length is significantly shorter than the penetration depth. And even then, the effect is less than what we have calculated based on bulk values of the superconducting electron density only. We can only make an estimate of the coherence length of our NbTiN sample based on literature [167], which is $\xi_0 = 170 \text{ nm}$. But the coherence length depends on temperature, such that it diverges at the critical temperature and becomes significantly smaller near 0 K. Correctly taking the surface effects into account will therefore lead to a smaller effect of superconductivity, but approaches our bulk value calculations near $T \ll T_c$. We therefore need to repeat our measurements at significantly lower temperatures.

However, it is already a significant result to set an upper limit of 2.6% on the effect of superconductivity, significantly larger than the effect predicted by the plasma model, but of the same order as the effect predicted by the Drude-Lorentz model. This means that only small improvements are needed to be able to distinguish the effect of the superconducting state.

8.3 Conclusion

The Casimir force depends on the reflectivity of the interacting surfaces. When the dielectric permittivity of a material is known, the Casimir force can be calculated. We have shown these calculations based on optical reflection measurements of NbTiN. The computed Casimir force gradient is then compared to measurements between a gold coated microsphere and a NbTiN thin film. At room temperature, the overlap with the calculations is striking. Due to the higher resistivity of NbTiN compared to gold, the Drude-Lorentz and generalized plasma models coincide at a higher frequency, such that even at room temperature the two models predict different contributions at higher order Matsubara frequencies. The two models lead to a significant difference in the Casimir force gradient that is detectable even with moderate sensitivity at close distances. Our measurements show better agreement with the Drude-Lorentz description and seem to exclude the plasma description.

At low temperatures, the experiments showed a twenty percent increase in the measured Casimir force, which does not coincide with our calculations of the force at these temperatures. We could find no satisfying explanation for this effect. However, our real-time calibration scheme and the good overlap between theory and experiment at room temperature convince us that the measurements are not dominated by other forces or drifts in the system between the moment of calibration and the measurements. Measurements of the Casimir force between 22 K and room temperature will demonstrate when this effect occurs and whether the transition is gradual or sudden. Comparison to Casimir force measurements between two gold surfaces at low temperature will exclude any technical errors leading to this effect. The measurements seem to indicate that the NbTiN plate behaves metallic, although optical reflection measurements do not show this behaviour. This may indicate that Casimir force measurements can provide new information on the reflection and conductance properties of materials that are not visible with other experiments.

Measuring the Casimir force between superconductors is a good way to gain insight in the role of dissipation in the Casimir force [49, 55], since dissipation becomes absent in superconductors. Our experiments show no significant influence of the superconducting state and can set an upper limit of 2.6% on its effect. This is of the same order of magnitude as the expected effect of superconductivity on the Casimir force, if such an effect exists.

Increased Read-Out Sensitivity with an Optomechanical Cavity

Interest in the Casimir force has increased significantly since technological progress allowed for more sensitive measurements of the force. The Casimir force has been measured between different materials, such as metals [11, 47, 50, 52, 54, 135, 142, 143, 146], semiconductors [51, 175–178], conductive oxides [144], ferromagnets [107] and even superconductors [179].

Also theoretically, methods have been developed for accurate calculations of the force between real materials in different geometries [113, 114, 180, 181]. These calculations in general show good agreement with experiment within several percent. But for a more accurate comparison improvements are required in the force sensitivity of the measurements. One question that is still not answered with satisfaction is what model to use to extrapolate the measured dielectric permittivity of the surfaces to lower frequencies. Two models are proposed, one that includes Ohmic dissipation (Drude model) and one that does not account for dissipation (plasma model).

As discussed in chapter 5 and Refs. [49, 55] differentiating between the two models would be possible by measurements of the Casimir force between superconductors. Since we know that dissipation is not present in superconductors, we can compare these experiments with measurements above the critical temperature. From the presence or absence of notable differences we can deduce the role of dissipation in normal conductors. This experimental investigation of the Casimir force between gold and a superconductor is discussed in chapter 8. We found that the measurement precision was of the same order of magnitude as the maximally expected effect of superconductivity on the Casimir force. To get a more definite insight into this effect, it is necessary to increase our force sensitivity.

In this chapter we will discuss our current sensitivity and remark on some possible changes. One major change would be to combine the Casimir set-up with an optomechanical cavity to read out the motion of the resonator acting as the force sensor. With this set-up it would in principle be possible to increase the force sensitivity by an order of magnitude.

9.1 Considerations for Further Improvements

Measurements of the Casimir force gradient as a function of temperature, see Figure 8.5, show a force sensitivity that is of the same order of magnitude as the expected influence of superconductivity. This influence is negligible near the critical temperature, and only approaches the expected maximum value near 0 K. It is therefore unfortunate that the lowest temperature in our measurements was only a few Kelvin below the critical temperature. We could lower the base temperature of our cryostat, or double the effect by measuring the Casimir force between two superconductors. But even then we need to improve on the force sensitivity of our set-up.

To investigate the force sensitivity of our set-up and its limitations, we first look at the frequency read-out of our cantilever. The cantilever frequency is determined via interferometric read-out of the motion, with the signal sent to a frequency counter (Agilent 53131A). A self-oscillating circuit drives the cantilever at a constant amplitude [161]. In Figure 9.1(a) we show the detected frequency as a function of time with a time interval of one second. During this measurement, the cantilever was in vacuum ($p \approx 10^{-4}$ mbar) and at room temperature. The cantilever was withdrawn several millimeters from the plate. Over the measurement time of several hours, no drifts were present in the cantilever frequency, interferometric read-out and frequency counter. From a fit to the histogram of the data, see Figure 9.1(b), we determine that the read-out sensitivity of the cantilever frequency is 13 mHz. Via the system parameter $\mu = 2.22 \times 10^{-12}$ Hz m² V⁻² we calculate that the sensitivity of the normalized force gradient is equal to 0.16 N/m², based solely on the read-out of the cantilever motion. This corresponds to a parallel-plate pressure of 0.025 N/m². The actual measurement precision based on our Casimir force measurements shown in chapter 8 is an order of magnitude higher. But these measurements were obtained while the distance between the plate and the sphere was fixed. Since the Casimir force depends strongly on the distance, any deviation in the distance results in a

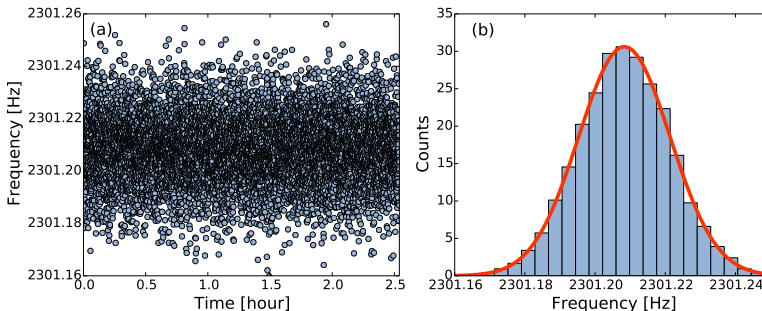


Figure 9.1: Force sensitivity of our set-up: (a) Cantilever frequency measured with fiber interferometry and detected by a frequency counter for several hours. The time interval between data is set at 1 s. The frequency counter, interferometric read-out and cantilever frequency are not sensitive to drifts in a few hours; (b) Histogram of the data in (a). The frequency sensitivity is 13 mHz, which results in a force gradient sensitivity of 0.16 N/m².

strong deviation in the measured force. The difference between the predicted and actual force sensitivity can therefore be explained by the fact that the distance lock is not tight enough. This is again a result of our force sensitivity, since small, low frequency fluctuations in the detection lead to small fluctuations in the distance. For the current settings of our force detection, mostly determined by the AC voltage that sets the magnitude of the electrostatic force, the fluctuations in the distance are of the order of a nanometer.

The lock can be improved by setting reasonable feedback parameters. But the distance feedback is based on the electrostatic force and thus on the force read-out. Improving the force sensitivity will therefore also improve the distance lock.

Theoretically, the minimum force gradient that can be detected with the frequency modulation (FM) technique and interferometric read-out is given by [161]

$$\left. \frac{\partial F}{\partial d} \right|_{\min} = \sqrt{\frac{4k_B k_B T}{\omega_0 Q \langle x_{\text{osc}}^2 \rangle}} \quad (9.1)$$

with k the spring constant, B the measurement bandwidth, k_B Boltzmann's constant, T the temperature and ω_0 and Q the cantilever's angular frequency and quality factor respectively. The mean-square amplitude $\langle x_{\text{osc}}^2 \rangle$ is the driven amplitude of the cantilever, which is generally larger than the thermal motion. Via the proximity force approximation (see Eq. 5.31) we can relate this value to the minimal detectable parallel-plate pressure

$$P_{pp}|_{\min} \approx \frac{1}{2\pi R} \sqrt{\frac{4k_B k_B T}{\omega_0 Q \langle x_{\text{osc}}^2 \rangle}}. \quad (9.2)$$

If we put in our experimental parameters $R = 100 \mu\text{m}$, $k \approx 1 \text{ N/m}$, $B = 1 \text{ Hz}$, $\omega_0/2\pi = 2.3 \text{ kHz}$, $Q = 5000$ and take a driven amplitude of $x_{\text{rms}} = 5 \text{ nm}$, we find at room temperature that the minimal detectable pressure is equal to 0.005 N/m^2 . The difference between this value and the measured sensitivity in Figure 9.1 is caused either by laser phase noise or by noise in the electronics driving the cantilever at constant amplitude.

At low temperature, the minimal detectable pressure is an order of magnitude lower, $3 \times 10^{-4} \text{ N/m}^2$, directly due to the influence of the temperature, but also indirectly because the mechanical quality factor is higher, $Q \approx 30\,000$. The resonance frequency and spring constant shift a few percent up, but this is a negligible effect. We could further lower the detectable force gradient by limiting the bandwidth further, but this will increase our measurement time. Increasing the cantilever amplitude has a positive effect on the detectable pressure. But a large oscillation means a large modulation of the sphere-plate distance. And since the Casimir force, but also the electrostatic force, decreases nonlinearly with distance, this modulation results in an larger average force. If the cantilever amplitude is large compared to the average distance, mixing between the frequency components of our modulation technique can occur. A large cantilever amplitude results in a large average electrostatic force, which causes a large amplitude at the modulation frequency ω_1 , such that the Casimir force is also modulated at this frequency. Increasing the cantilever amplitude is therefore limited to only a few nanometers.

Measuring at low temperatures theoretically lowers the minimal detectable pressure, but in our experiment we see no difference between the room temperature force sensitivity and the sensitivity at low temperature. This means that other noise sources, like laser noise, are still dominant [51]. If we want to increase our force sensitivity, we can gain a lot by improving the feedback parameters of the distance lock, by increasing the electrostatic force set-point and by upgrading the electronics that drive the cantilever. Increasing the read-out sensitivity would also be a great improvement.

9.2 A New Measurement Set-up

The force sensitivity of our current set-up can be increased via the recommendations mentioned above. But even if all the technical noise is cleared up, there is still a limit from the interferometric read-out. In chapter 7 we found that the noise floor of our interferometric read-out is equal to $\sigma = 100 \text{ fm}/\sqrt{\text{Hz}}$. If we take a measurement bandwidth of 1 Hz, spring constant of 1 N/m, a sphere with radius 100 μm and a sphere-plate distance of 100 nm, we find via

$$P_{pp} = \frac{\sigma k \sqrt{B}}{2\pi R d} \quad (9.3)$$

that the detection limit of the parallel-plate pressure is equal to 0.002 N/m². To reach the minimal detectable pressure at low temperature as given by Eq. 9.3, we should also improve the detection of the cantilever motion.

In general, an optical cavity provides a more sensitive read-out of the resonator motion than a fiber interferometer, due to a stronger light-resonator interaction. To demonstrate this, with our optomechanical cavity we measure a noise floor of 300 am/ $\sqrt{\text{Hz}}$, which is a factor 300 lower than what we can achieve with our fiber interferometer. Note that this is measured at the resonance frequency of the trampoline resonator, which is two orders of magnitude higher than for the cantilevers with microspheres.

We can use the trampoline resonator as our force sensor, the only adaption to our current optomechanical set-up would be a conductive coating of the resonator, which is required for our calibration and compensation scheme based on the electrostatic force. An advantage of the trampoline resonators is that we can increase the interaction area of the force. Whereas spheres with a large radius generally also have a larger surface roughness [156], trampoline resonators or nanomembranes can be manufactured with an area of the order of 1 mm² while maintaining practically flat surfaces. The idea of using a nanomembrane to read out the motion has been proposed before [182–185], but in these proposals it was not combined with a high-finesse cavity for read-out.

At first glance, it would seem imprudent to pair our flat trampoline resonator with a flat conductive plate for the Casimir force measurements, because of the technical challenge to align them perfectly parallel. But having to align a sphere directly opposite the resonator is also not ideal. Fortunately, it was shown [186] that the trampoline resonators are curved due to the tensile stress in the silicon nitride. The

radius of curvature is commonly about $R \approx 1$ mm. We can therefore pair a curved trampoline resonator with a flat conductive plate.

Another advantage of using trampoline resonators is that its mechanical properties can be tuned. Compared to microspheres attached to cantilevers, the mechanical quality factor, resonance frequency and radius of curvature are higher. The spring constant can be tuned by the design of the arms of the resonator. A low spring constant is better for the force sensitivity, but when it is too low, the resonator may snap under the influence of the large forces. Fortunately, further tunability is possible due to the optical spring effect [187]. In principle, the spring constant can be adapted as the distance between the resonator and the plate changes. A comparison of typical parameters of the two systems is shown in Table 9.1.

	microsphere on cantilever	trampoline resonator
radius of curvature	100 μm	1 mm
resonance frequency	2 kHz	200 kHz
mechanical quality factor	5000 - 30 000	400 000
spring constant	1 N/m	0.2 N/m, tunable
read-out	interferometric	high-finesse cavity

Table 9.1: Comparison of typical parameters of two systems for Casimir force measurements; a microsphere attached to an atomic force microscope cantilever that was used in this thesis and the proposed improvement based on a trampoline resonator.

Based on the noise floor of $300 \text{ am}/\sqrt{\text{Hz}}$ of our optomechanical cavity, we find that the optical cavity can read out a pressure of $1 \times 10^{-7} \text{ N/m}^2$, at a distance of 100 nm and a bandwidth of 1 Hz. The minimal pressure that can be detected by the trampoline resonator, using the FM technique, is according to Eq. 9.3 equal to $9 \times 10^{-5} \text{ N/m}^2$ at room temperature based on a thermal resonator RMS amplitude of 144 pm. The trampoline resonator can be driven [80, 188] to an amplitude of around 1 nm, which would result in a minimal detectable pressure of $1.3 \times 10^{-5} \text{ N/m}^2$, a significant enhancement compared to our current sensitivity.

To set the distance between the trampoline resonator, it is possible to position the plate on a piezo-electric translation stage. The distance can be determined by modulating the electrostatic force between the two surfaces in a similar fashion described in this thesis. This method requires an independent read-out of the plate's distance change d_{pz} during a measurement run. We therefore need to install a fiber interferometer directed towards the plate. Since we are not interested in the absolute direction of the distance change, we can place the fiber on either side of the plate. Behind the plate would be more advantageous for spatial arguments. Another, more challenging, but also more sensitive option would be to align a second beam between the large cavity mirror and the plate to form a second optical cavity that is tilted slightly with respect to the first cavity.

To set the distance more accurately than can be done with a piezo, we can use the nested resonator described in chapter 4. The coated outer resonator and the plate form a capacitor. By setting an adequate voltage between them, the electrostatic force will pull the nested resonator closer to the plate. Since this requires different volt-

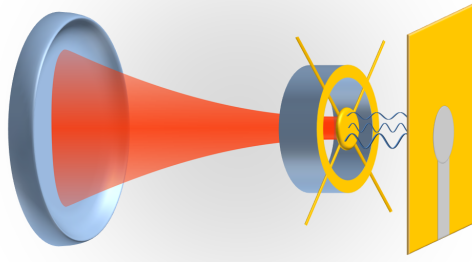


Figure 9.2: Impression of the set-up for Casimir force measurements with an optomechanical cavity for force detection. The large cavity mirror (left), nested resonator (middle) and plate (right) are indicated, as well as the cavity light and vacuum fluctuations. The plate is separated into two areas which can be set at different potentials. The center area (grey) is used for calibration and compensation as described in chapter 7 of this thesis, the outer area (yellow) is used to set the distance between the nested resonator and the plate.

ages than needed for our calibration and compensation technique, the plate needs to be divided into two areas that can be set at different voltages with respect to the nested resonator. The voltages V_{DC} and V_{AC} , required for our modulation scheme, are applied to the inner area, indicated in grey in Figure 9.2. The distance between the outer resonator and plate is set by the potential of the outer area. A large degree of control of the nested resonator motion with the dielectric force was already shown in Ref. [96]. A similar degree of control can be expected with the capacitive force, as the main objection in chapter 4 against this force was the alignment procedure, which is required in this set-up anyway.

Combining the Casimir force measurement method based on modulation of the electrostatic force with an optomechanical cavity to read out the motion of the trampoline resonator serving as a force sensor is a promising way to significantly improve our force sensitivity. Our current force gradient sensitivity of 2 N/m^2 (corresponding to a pressure sensitivity of 0.3 N/m^2) is limited by noise in our electronics. If we can eliminate this noise, we are still limited to a minimal detectable pressure of 0.005 N/m^2 at room temperature based on the read-out sensitivity of our fiber interferometer. We can improve on this further if we switch to optomechanical cavities. The resulting pressure sensitivity of $1.3 \times 10^{-5} \text{ N/m}^2$ at low temperatures is significantly better than with our current set-up. For comparison, the lowest experimental error reported so far is $2.2 \times 10^{-3} \text{ N/m}^2$ [11].

Casimir force in terms of reflection coefficients

In this appendix we will show the calculations to rewrite the Lifshitz expression for the Casimir force in terms of the reflection coefficients of the plates [110]. The reflection coefficients are expressed in terms of the Fresnel equations. The calculations and expressions are partially based on Ref. [98]. We start with the original expression found by Lifshitz (Equation 5.10 of this thesis and Equation 5.2 of Ref. [97]):

$$F_C = \frac{k_B T}{\pi c^3} \sum'_{n=0} \int_1^{\infty} p^2 \xi_n^3 \left\{ \left[\frac{(s_1 + p)(s_2 + p)}{(s_1 - p)(s_2 - p)} e^{2p\xi_n d/c} - 1 \right]^{-1} + \left[\frac{(s_1 + \varepsilon_1 p)(s_2 + \varepsilon_2 p)}{(s_1 - \varepsilon_1 p)(s_2 - \varepsilon_2 p)} e^{2p\xi_n d/c} - 1 \right]^{-1} \right\} dp, \quad (\text{A.1})$$

where T is the temperature, d the distance between the plates and k_B and c Boltzmann's constant and the speed of light respectively. The prime on the summation mark indicates that the term with $n = 0$ is multiplied by $\frac{1}{2}$. For imaginary frequencies $\omega = i\xi_n = i\frac{2k_B T}{\hbar}n$,

$$p = \sqrt{1 + \frac{c^2}{\xi_n^2} k_{\parallel}^2}, \quad (\text{A.2})$$

$$s_{1,2} = \sqrt{\varepsilon_{1,2}(i\xi_n) - 1 + p^2} = \sqrt{\varepsilon_{1,2}(i\xi_n) + \frac{c^2}{\xi_n^2} k_{\parallel}^2}, \quad (\text{A.3})$$

with k_{\parallel} the wave vector component tangential to the plates. If we multiply the numerators and denominators in Equation A.1 by ξ_n^2/c^2 and write out the expressions

of p and $s_{1,2}$, we find for the fractions

$$\frac{s_{1,2} + p}{s_{1,2} - p} = \frac{\sqrt{\varepsilon_{1,2} \frac{\xi_n^2}{c^2} + k_{\parallel}^2} + \sqrt{\frac{\xi_n^2}{c^2} + k_{\parallel}^2}}{\sqrt{\varepsilon_{1,2} \frac{\xi_n^2}{c^2} + k_{\parallel}^2} - \sqrt{\frac{\xi_n^2}{c^2} + k_{\parallel}^2}}, \quad (\text{A.4})$$

$$\frac{s_{1,2} + \varepsilon_{1,2} p}{s_{1,2} - \varepsilon_{1,2} p} = \frac{\sqrt{\varepsilon_{1,2} \frac{\xi_n^2}{c^2} + k_{\parallel}^2} + \varepsilon_{1,2} \sqrt{\frac{\xi_n^2}{c^2} + k_{\parallel}^2}}{\sqrt{\varepsilon_{1,2} \frac{\xi_n^2}{c^2} + k_{\parallel}^2} - \varepsilon_{1,2} \sqrt{\frac{\xi_n^2}{c^2} + k_{\parallel}^2}}, \quad (\text{A.5})$$

where $\varepsilon_{1,2} = \varepsilon_{1,2}(i\xi_n)$. We can simplify these expressions if we introduce $q_n = \sqrt{\frac{\xi_n^2}{c^2} + k_{\parallel}^2}$ and $k_n^{(1,2)} = \sqrt{\varepsilon_{1,2} \frac{\xi_n^2}{c^2} + k_{\parallel}^2}$:

$$\frac{s_{1,2} + p}{s_{1,2} - p} = \frac{k_n^{(1,2)} + q_n}{k_n^{(1,2)} - q_n} \quad (\text{A.6})$$

$$\frac{s_{1,2} + \varepsilon_{1,2} p}{s_{1,2} - \varepsilon_{1,2} p} = \frac{k_n^{(1,2)} + \varepsilon_{1,2} q_n}{k_n^{(1,2)} - \varepsilon_{1,2} q_n}. \quad (\text{A.7})$$

When we apply the expressions above and use $p dp = \frac{c^2}{\xi_n^2} k_{\parallel} dk_{\parallel}$, Equation A.1 looks like

$$F_C = \frac{k_B T}{\pi c^3} \sum_{n=0}^{\infty} \int_0^{\infty} \sqrt{1 + \frac{c^2}{\xi_n^2} k_{\parallel}^2} \xi_n^3 \left\{ \left[\frac{k_n^{(1)} + q_n k_n^{(2)} + q_n}{k_n^{(1)} - q_n k_n^{(2)} - q_n} e^{2\sqrt{\frac{\xi_n^2}{c^2} + k_{\parallel}^2} d} - 1 \right]^{-1} + \left[\frac{k_n^{(1)} + \varepsilon_{1,2} q_n k_n^{(2)} + \varepsilon_{2,2} q_n}{k_n^{(1)} - \varepsilon_{1,2} q_n k_n^{(2)} - \varepsilon_{2,2} q_n} e^{2\sqrt{\frac{\xi_n^2}{c^2} + k_{\parallel}^2} d} - 1 \right]^{-1} \right\} \frac{c^2}{\xi_n^2} k_{\parallel} dk_{\parallel}. \quad (\text{A.8})$$

For any further simplification we turn to the Fresnel equations for the reflection coefficients for the transverse electric and transverse magnetic waves [189], where θ_0 is the angle of incidence for a wave in vacuum reflecting on a medium with dielectric permittivity ε :

$$r_{\text{TE}} = \frac{\cos \theta_0 - \sqrt{\varepsilon - \sin^2 \theta_0}}{\cos \theta_0 + \sqrt{\varepsilon - \sin^2 \theta_0}},$$

$$r_{\text{TM}} = \frac{\varepsilon \cos \theta_0 - \sqrt{\varepsilon - \sin^2 \theta_0}}{\varepsilon \cos \theta_0 + \sqrt{\varepsilon - \sin^2 \theta_0}}. \quad (\text{A.9})$$

For an electromagnetic wave in vacuum $\sin \theta_0 = k_{\parallel} c / \omega$, such that $\cos^2 \theta_0 = 1 - k_{\parallel}^2 c^2 / \omega^2$. By setting $\omega = i\xi_n$ and multiplying by ξ_n / c , we arrive at $\frac{\xi_n}{c} \cos \theta_0 =$

$\sqrt{\frac{\xi_n^2}{c^2} + k_{\parallel}^2} = q_n$ and $\frac{\xi_n}{c} \sqrt{\varepsilon - \sin^2 \theta_0} = \sqrt{\varepsilon \frac{\xi_n^2}{c^2} + k_{\parallel}^2} = k_n$. This means we can write

$$r_{\text{TE}}^{(1,2)} = \frac{q_n - k_n^{(1,2)}}{q_n + k_n^{(1,2)}}, \quad (\text{A.10})$$

$$r_{\text{TM}}^{(1,2)} = \frac{\varepsilon_{1,2} q_n - k_n^{(1,2)}}{\varepsilon_{1,2} q_n + k_n^{(1,2)}}. \quad (\text{A.11})$$

If we compare this with the fractions in Equation A.8, we see that we can replace them directly with the inverted reflection coefficients¹. After some final transformations, we arrive at the expression for the Casimir force in terms of the reflection coefficients:

$$F_C = \frac{k_B T}{\pi} \sum_{n=0}^{\infty} \int_0^{\infty} q_n k_{\parallel} \left\{ \left[\left(r_{\text{TE}}^{(1)} r_{\text{TE}}^{(2)} \right)^{-1} e^{2q_n d} - 1 \right]^{-1} + \left[\left(r_{\text{TM}}^{(1)} r_{\text{TM}}^{(2)} \right)^{-1} e^{2q_n d} - 1 \right]^{-1} \right\} dk_{\parallel}. \quad (\text{A.12})$$

¹Actually, the fractions are inversely proportional to $-r_{\text{TE,TM}}$, but since the reflection coefficient of medium 1 is multiplied by the reflection coefficient of medium 2, the minus signs cancel out.

Bibliography

- [1] J. Kepler, *De cometis libelli tres* (Andreas Pergeri, 1619).
- [2] J. C. Maxwell, *A Treatise on Electricity and Magnetism* (Clarendon Press, Oxford, 1873).
- [3] P. Lebedev, *Ann. Phys. (Berlin)* **311**, 433 (1901).
- [4] E. F. Nichols and G. F. Hull, *Phys. Rev.* **13**, 307 (1901).
- [5] V. B. Braginsky, A. B. Manukin, and M. Y. Tikhonov, *JETP* **31**, 829 (1970).
- [6] A. Dorsel, J. McCullen, P. Meystre, E. Vignes, and H. Walther, *Phys. Rev. Lett.* **51**, 1550 (1983).
- [7] P.-F. Cohadon, A. Heidmann, and M. Pinard, *Phys. Rev. Lett.* **83**, 3174 (1999).
- [8] B. P. Abbott, R. Abbott, T. D. Abbott, M. R. Abernathy, F. Acernese, K. Ackley, C. Adams, T. Adams, P. Addesso, R. X. Adhikari, et al. (LIGO Scientific Collaboration and Virgo Collaboration), *Phys. Rev. Lett.* **116**, 061102 (2016).
- [9] V. M. Mostepanenko and I. Y. Sokolov, *Phys. Lett. A* **125**, 405 (1987).
- [10] E. Fischbach, D. E. Krause, V. M. Mostepanenko, and M. Novello, *Phys. Rev. D* **64**, 075010 (2001).
- [11] R. S. Decca, D. López, E. Fischbach, G. L. Klimchitskaya, D. E. Krause, and V. M. Mostepanenko, *Phys. Rev. D* **75**, 077101 (2007).
- [12] E. Schrödinger, *Naturwissenschaften* **23**, 807 (1935).
- [13] S. Bose, K. Jacobs, and P. L. Knight, *Phys. Rev. A* **56**, 4175 (1997).
- [14] S. Bose, K. Jacobs, and P. L. Knight, *Phys. Rev. A* **59**, 3204 (1999).

- [15] W. H. Zurek, *Phys. Today* **44**, 36 (1991).
- [16] G. C. Ghirardi, A. Rimini, and T. Weber, *Phys. Rev. D* **34**, 470 (1986).
- [17] L. Diósi, *Phys. Rev. A* **40**, 1165 (1989).
- [18] R. Penrose, *Gen. Rel. Gravit.* **28**, 581 (1996).
- [19] I. Pikovski, M. R. Vanner, M. Aspelmeyer, M. Kim, and Č. Brukner, *Nature Physics* **8**, 393 (2012).
- [20] M. Brune, E. Hagley, J. Dreyer, X. Maître, A. Maali, C. Wunderlich, J. M. Raimond, and S. Haroche, *Phys. Rev. Lett.* **77**, 4887 (1996).
- [21] W. Marshall, C. Simon, R. Penrose, and D. Bouwmeester, *Phys. Rev. Lett.* **91**, 130401 (2003).
- [22] D. Kleckner, I. Pikovski, E. Jeffrey, L. Ament, E. Eliel, J. van den Brink, and D. Bouwmeester, *New J. Phys.* **10**, 095020 (2008).
- [23] B. Pepper, R. Ghobadi, E. Jeffrey, C. Simon, and D. Bouwmeester, *Phys. Rev. Lett.* **109**, 023601 (2012).
- [24] M. Arndt and K. Hornberger, *Nature Physics* **10**, 271 (2014).
- [25] M. Aspelmeyer, T. J. Kippenberg, and F. Marquardt, *Rev. Mod. Phys.* **86**, 1391 (2014).
- [26] A. D. O'Connell, M. Hofheinz, M. Ansmann, R. C. Bialczak, M. Lenander, E. Lucero, M. Neeley, D. Sank, H. Wang, M. Weides, et al., *Nature* **464**, 697 (2010).
- [27] J. Chan, T. M. Alegre, A. H. Safavi-Naeini, J. T. Hill, A. Krause, S. Gröblacher, M. Aspelmeyer, and O. Painter, *Nature* **478**, 89 (2011).
- [28] J. Teufel, T. Donner, D. Li, J. Harlow, M. Allman, K. Cicak, A. Sirois, J. Whittaker, K. Lehnert, and R. Simmonds, *Nature* **475**, 359 (2011).
- [29] R. W. Peterson, T. P. Purdy, N. S. Kampel, R. W. Andrews, P.-L. Yu, K. W. Lehnert, and C. A. Regal, *Phys. Rev. Lett.* **116**, 063601 (2016).
- [30] A. Noguchi, R. Yamazaki, M. Ataka, H. Fujita, Y. Tabuchi, T. Ishikawa, K. Usami, and Y. Nakamura, *New J. Phys.* **18**, 103036 (2016).
- [31] S. Weis, R. Rivière, S. Deléglise, E. Gavartin, O. Arcizet, A. Schliesser, and T. J. Kippenberg, *Science* **330**, 1520 (2010).
- [32] A. H. Safavi-Naeini, T. M. Alegre, J. Chan, M. Eichenfield, M. Winger, Q. Lin, J. T. Hill, D. E. Chang, and O. Painter, *Nature* **472**, 69 (2011).
- [33] F. M. Buters, F. Luna, M. J. Weaver, H. J. Eerkens, K. Heeck, S. de Man, and D. Bouwmeester, *Opt. Express* (submitted).

-
- [34] S. Gröblacher, K. Hammerer, M. R. Vanner, and M. Aspelmeyer, *Nature* **460**, 724 (2009).
- [35] E. Verhagen, S. Deléglise, S. Weis, A. Schliesser, and T. J. Kippenberg, *Nature* **482**, 63 (2012).
- [36] P. W. Milonni, *The Quantum Vacuum: An Introduction to Quantum Electrodynamics* (Academic Press, San Diego, 1993).
- [37] H. B. G. Casimir, *Proc. K. Ned. Akad. Wet.* **51**, 793 (1948).
- [38] S. J. Minter, K. Wegter-McNelly, and R. Y. Chiao, *Physica E* **42**, 234 (2010).
- [39] J. Q. Quach, *Phys. Rev. Lett.* **114**, 081104 (2015).
- [40] B. C. Denardo, J. J. Puda, and A. Larraza, *Am. J. Phys* **77**, 1095 (2009).
- [41] E. D'Hoker and P. Sikivie, *Phys. Rev. Lett.* **71**, 1136 (1993).
- [42] D. J. Griffiths and E. Ho, *Am. J. Phys.* **69**, 1173 (2001).
- [43] J. Th. Overbeek and M. J. Sparnaay, *Disc. Faraday Soc.* **18**, 12 (1954).
- [44] M. J. Sparnaay, *Physica* **24**, 751 (1958).
- [45] B. V. Derjaguin and I. I. Abrikosova, *Sov. Phys. JETP* **3**, 819 (1957).
- [46] I. I. Abrikosova and B. V. Derjaguin, *Sov. Phys. JETP* **4**, 2 (1957).
- [47] S. K. Lamoreaux, *Phys. Rev. Lett.* **78**, 5 (1997).
- [48] J. S. Høye, I. Brevik, J. B. Aarseth, and K. A. Milton, *Phys. Rev. E* **67**, 056116 (2003).
- [49] G. Bimonte, *Phys. Rev. A* **78**, 062101 (2008).
- [50] A. O. Sushkov, W. J. Kim, D. A. R. Dalvit, and S. K. Lamoreaux, *Nature Physics* **7**, 230 (2011).
- [51] J. Laurent, H. Sellier, A. Mosset, S. Huant, and J. Chevrier, *Phys. Rev. B* **85**, 035426 (2012).
- [52] C.-C. Chang, A. A. Banishev, R. Castillo-Garza, G. L. Klimchitskaya, V. M. Mostepanenko, and U. Mohideen, *Phys. Rev. B* **85**, 165443 (2012).
- [53] R. Castillo-Garza and U. Mohideen, *Rev. Sci. Instrum.* **84**, 025110 (2013).
- [54] R. Castillo-Garza, J. Xu, G. L. Klimchitskaya, V. M. Mostepanenko, and U. Mohideen, *Phys. Rev. B* **88**, 075402 (2013).
- [55] G. Bimonte, E. Calloni, G. Esposito, and L. Rosa, *Nucl. Phys. B* **726**, 441 (2005).
- [56] I. Wilson-Rae, N. Nooshi, W. Zwerger, and T. Kippenberg, *Phys. Rev. Lett.* **99**, 093901 (2007).

- [57] F. Marquardt, J. P. Chen, A. Clerk, and S. Girvin, *Phys. Rev. Lett.* **99**, 093902 (2007).
- [58] O. Arcizet, P.-F. Cohadon, T. Briant, M. Pinard, and A. Heidmann, *Nature* **444**, 71 (2006).
- [59] A. Schliesser, R. Rivière, G. Anetsberger, O. Arcizet, and T. J. Kippenberg, *Nature Physics* **4**, 415 (2008).
- [60] A. Schliesser, O. Arcizet, R. Riviere, G. Anetsberger, and T. Kippenberg, *Nature Physics* **5**, 509 (2009).
- [61] T. Purdy, R. Peterson, P. Yu, and C. Regal, *New J. Phys.* **14**, 115021 (2012).
- [62] A. H. Safavi-Naeini, J. Chan, J. T. Hill, T. P. M. Alegre, A. Krause, and O. Painter, *Phys. Rev. Lett.* **108**, 033602 (2012).
- [63] D. Kleckner, B. Pepper, E. Jeffrey, P. Sonin, S. M. Thon, and D. Bouwmeester, *Opt. Express* **19**, 19708 (2011).
- [64] E. D. Black, *Am. J. Phys.* **69**, 79 (2001).
- [65] G. A. Phelps and P. Meystre, *Phys. Rev. A* **83**, 063838 (2011).
- [66] J. M. W. Milatz, J. J. van Zolingen, and B. B. van Iperen, *Physica* **19**, 195 (1953).
- [67] H. Hirakawa, S. Hiramatsu, and Y. Ogawa, *Phys. Lett. A* **63**, 199 (1977).
- [68] A. Hopkins, K. Jacobs, S. Habib, and K. Schwab, *Phys. Rev. B* **68**, 235238 (2003).
- [69] D. Kleckner and D. Bouwmeester, *Nature* **444**, 75 (2006).
- [70] W. B. Case, *Am. J. Phys.* **64**, 215 (1996).
- [71] C. H. Metzger and K. Karrai, *Nature* **432**, 1002 (2004).
- [72] H. J. Eerkens, F. M. Buters, M. J. Weaver, B. Pepper, G. Welker, K. Heeck, P. Sonin, S. de Man, and D. Bouwmeester, *Opt. Express* **23**, 8014 (2015).
- [73] V. Braginsky, S. Strigin, and S. P. Vyatchanin, *Phys. Lett. A* **287**, 331 (2001).
- [74] T. Carmon, H. Rokhsari, L. Yang, T. J. Kippenberg, and K. J. Vahala, *Phys. Rev. Lett.* **94**, 223902 (2005).
- [75] F. Marino and F. Marin, *Phys. Rev. E* **87**, 052906 (2013).
- [76] L. Bakemeier, A. Alvermann, and H. Fehske, *Phys. Rev. Lett.* **114**, 013601 (2015).
- [77] T. Kippenberg, H. Rokhsari, T. Carmon, A. Scherer, and K. Vahala, *Phys. Rev. Lett.* **95**, 033901 (2005).
- [78] M. Ludwig, B. Kubala, and F. Marquardt, *New J. Phys.* **10**, 095013 (2008).

-
- [79] F. Marquardt, J. Harris, and S. Girvin, *Phys. Rev. Lett.* **96**, 103901 (2006).
- [80] F. Buters, H. Eerkens, K. Heeck, M. Weaver, B. Pepper, S. de Man, and D. Bouwmeester, *Phys. Rev. A* **92**, 013811 (2015).
- [81] F. M. Buters, H. J. Eerkens, K. Heeck, M. J. Weaver, B. Pepper, P. Sonin, S. de Man, and D. Bouwmeester, *Phys. Scr.* **T165**, 014003 (2015).
- [82] J. Poirson, F. Bretenaker, M. Vallet, and A. Le Floch, *JOSA B* **14**, 2811 (1997).
- [83] M. Ludwig, Ph.D. thesis, Friedrich-Alexander-Universität, Erlangen-Nürnberg (2013).
- [84] D. Rugar and P. Grütter, *Phys. Rev. Lett.* **67**, 699 (1991).
- [85] B. Pepper, Ph.D. thesis, University of California Santa Barbara (2014).
- [86] J. A. Haringx, *Philips Tech. Rev.* **1**, 16 (1947).
- [87] G. M. Harry and the LIGO Scientific Collaboration, *Class. Quantum Grav.* **27**, 084006 (2010).
- [88] E. Serra, A. Borrielli, F. S. Cataliotti, F. Marin, F. Marino, A. Pontin, G. A. Prodi, and M. Bonaldi, *Phys. Rev. A* **86**, 051801 (2012).
- [89] J. Liu, F. A. Torres, Y. Ma, C. Zhao, L. Ju, D. G. Blair, S. Chao, I. Roch-Jeune, R. Flaminio, C. Michel, et al., *Appl. Opt.* **53**, 841 (2014).
- [90] R. A. Norte, Ph.D. thesis, California Institute of Technology (2014).
- [91] M. J. Weaver, B. Pepper, F. Luna, F. M. Buters, H. J. Eerkens, G. Welker, B. Percock, K. Heeck, S. de Man, and D. Bouwmeester, *Appl. Phys. Lett.* **108**, 033501 (2016).
- [92] D. Rugar, H. J. Mamin, R. Erlandsson, J. E. Stern, and B. D. Terris, *Rev. Sci. Instrum.* **59**, 2337 (1988).
- [93] Q. P. Unterreithmeier, E. M. Weig, and J. P. Kotthaus, *Nature* **458**, 1001 (2009).
- [94] J. B. Marion and S. T. Thornton, *Classical Dynamics of Particles and Systems* (Harcourt College Publishers, 1995), 4th ed.
- [95] D. J. Griffiths, *Introduction to Electrodynamics* (Prentice Hall, 1999), 3rd ed.
- [96] F. M. Buters, K. Heeck, H. J. Eerkens, M. J. Weaver, F. Luna, S. de Man, and D. Bouwmeester, *Appl. Phys. Lett.* **110**, 104104 (2017).
- [97] E. M. Lifshitz, *Soviet Physics* **2**, 73 (1956).
- [98] M. Bordag, G. L. Klimchitskaya, U. Mohideen, and V. M. Mostepanenko, *Advances in the Casimir Effect* (Oxford University Press, 2009).
- [99] J. Schwinger, L. L. DeRaad, and K. A. Milton, *Ann. Phys.* **115**, 1 (1978).

- [100] P. W. Milonni, *Phys. Rev. A* **25**, 1315 (1982).
- [101] R. L. Jaffe, *Phys. Rev. D* **72**, 021301 (2005).
- [102] O. Kenneth, I. Klich, A. Mann, and M. Revzen, *Phys. Rev. Lett.* **89**, 033001 (2002).
- [103] J. N. Munday, F. Capasso, and V. A. Parsegian, *Nature* **457**, 170 (2009).
- [104] A. D. Phan and N. A. Viet, *Phys. Rev. A* **84**, 062503 (2011).
- [105] S. M. Rytov, *Theory of Electrical Fluctuations and Thermal Radiation* (Academy of Sciences Press, Moscow, 1953).
- [106] M. S. Tomaš, *Phys. Lett. A* **342**, 381 (2005).
- [107] A. A. Banishev, G. L. Klimchitskaya, V. M. Mostepanenko, and U. Mohideen, *Phys. Rev. Lett.* **110**, 137401 (2013).
- [108] R. Esquivel-Sirvent, C. Villarreal, W. L. Mochán, A. M. Contreras-Reyes, and V. B. Svetovoy, *J. Phys. A* **39**, 6323 (2006).
- [109] G. S. Agarwal, *Phys. Rev. A* **11**, 243 (1975).
- [110] E. I. Kats, *JETP* **46**, 109 (1977).
- [111] I. Pirozhenko, A. Lambrecht, and V. B. Svetovoy, *New J. Phys.* **8**, 238 (2006).
- [112] E. D. Palik, ed., *Handbook of Optical Constants of Solids* (Academic Press Inc., San Diego, 1985).
- [113] S. K. Lamoreaux, *Phys. Rev. A* **59**, R3149 (1999).
- [114] A. Lambrecht and S. Reynaud, *Eur. Phys. J. D* **8**, 309 (2000).
- [115] N. W. Ashcroft and N. D. Mermin, *Solid State Physics* (Brooks Cole, 1976).
- [116] J. Peatross and M. Ware, *Physics of Light and Optics* (BYU Bookstore, Provo, USA, 2015).
- [117] M. Bordag, B. Geyer, G. L. Klimchitskaya, and V. M. Mostepanenko, *Phys. Rev. Lett.* **85**, 503 (2000).
- [118] G. L. Klimchitskaya and V. M. Mostepanenko, *Phys. Rev. A* **63**, 062108 (2001).
- [119] V. B. Bezerra, G. L. Klimchitskaya, V. M. Mostepanenko, and C. Romero, *Phys. Rev. A* **69**, 022119 (2004).
- [120] I. Brevik, J. B. Aarseth, J. S. Høyve, and K. A. Milton, *Phys. Rev. E* **71**, 056101 (2005).
- [121] I. Brevik, S. A. Ellingsen, and K. A. Milton, *New J. Phys.* **8**, 236 (2006).
- [122] F. Intravaia and C. Henkel, *J. Phys. A: Math. Theor.* **41**, 164018 (2008).

-
- [123] F. Intravaia and C. Henkel, Phys. Rev. Lett. **103**, 130405 (2009).
- [124] M. Boström and B. E. Sernelius, Phys. Rev. Lett. **84**, 4757 (2000).
- [125] F. Chen, G. L. Klimchitskaya, U. Mohideen, and V. M. Mostepanenko, Phys. Rev. Lett. **90**, 160404 (2003).
- [126] G. Bimonte, E. Calloni, G. Esposito, L. Milano, and L. Rosa, Phys. Rev. Lett. **94**, 180402 (2005).
- [127] R. Pöpel, J. Appl. Phys. **66**, 5950 (1989).
- [128] C. J. Gorter and H. Casimir, Physica **1**, 306 (1934).
- [129] H. Haakh, Ph.D. thesis, University of Potsdam (2009).
- [130] J. Bardeen, L. N. Cooper, and J. R. Schrieffer, Phys. Rev. **106**, 162 (1957).
- [131] J. Bardeen, L. N. Cooper, and J. R. Schrieffer, Phys. Rev. **108**, 1175 (1957).
- [132] D. C. Mattis and J. Bardeen, Phys. Rev. **111**, 412 (1958).
- [133] A. J. Berlinsky, C. Kallin, G. Rose, and A.-C. Shi, Phys. Rev. B **48**, 4074 (1993).
- [134] G. Bimonte, H. Haakh, C. Henkel, and F. Intravaia, J. Phys. A: Math. Theor. **43**, 145304 (2010).
- [135] G. Bressi, G. Carugno, R. Onofrio, and G. Ruoso, Phys. Rev. Lett. **88**, 041804 (2002).
- [136] B. Derjaguin, Kolloid Z. **69**, 155 (1934).
- [137] J. Blocki, J. Randrup, W. J. Swiatecki, and C. F. Tsang, Ann. Phys. **105**, 427 (1977).
- [138] V. A. Parsegian, *Van der Waals Forces: a handbook for biologists, chemists, engineers, and physicists* (Cambridge University Press, 2006).
- [139] M. Schaden and L. Spruch, Phys. Rev. Lett. **84**, 459 (2000).
- [140] J. R. Gavaler, D. W. Deis, J. K. Hulm, and C. K. Jones, Appl. Phys. Lett. **15**, 329 (1969).
- [141] T. de Jong, Master's thesis, Leiden University (2016).
- [142] U. Mohideen and A. Roy, Phys. Rev. Lett. **81**, 4549 (1998).
- [143] B. W. Harris, F. Chen, and U. Mohideen, Phys. Rev. A **62**, 052109 (2000).
- [144] S. de Man, K. Heeck, R. J. Wijngaarden, and D. Iannuzzi, Phys. Rev. Lett. **103**, 040402 (2009).
- [145] H. B. Chan, V. A. Aksyuk, R. N. Kleiman, D. J. Bishop, and F. Capasso, Science **291**, 1941 (2001).

- [146] R. S. Decca, D. López, E. Fischbach, and D. E. Krause, *Phys. Rev. Lett.* **91**, 050402 (2003).
- [147] R. S. Decca, D. López, and E. Osquiguil, *Int. J. Mod. Phys. A* **25**, 2223 (2010).
- [148] A. W. Rodriguez, F. Capasso, and S. G. Johnson, *Nature Photonics* **5**, 211 (2011).
- [149] W. A. Ducker, T. J. Senden, and R. M. Pashley, *Nature* **353**, 239 (1991).
- [150] D. Rugar, H. J. Mamin, and P. Guethner, *Appl. Phys. Lett.* **55**, 2588 (1989).
- [151] A. E. Siegman, *Lasers* (University Science Books, Sausalito, 1986).
- [152] E. Hecht, *Optics* (Addison Wesley, San Francisco, 2002), 4th ed.
- [153] G. Brooker, *Modern Classical Optics* (Oxford University Press, Oxford, 2002).
- [154] S. Yuan and N. A. Riza, *Appl. Opt.* **38**, 3214 (1999).
- [155] M. A. Arain and G. Mueller, *Opt. Express* **17**, 19181 (2009).
- [156] P. J. van Zwol, G. Palasantzas, M. van de Schootbrugge, J. T. M. de Hosson, and V. S. J. Craig, *Langmuir* **24**, 7528 (2008).
- [157] A. A. Maradudin and P. Mazur, *Phys. Rev. B* **22**, 1677 (1980).
- [158] G. L. Klimchitskaya, A. Roy, U. Mohideen, and V. M. Mostepanenko, *Phys. Rev. A* **60**, 3487 (1999).
- [159] M. Tinkham, *Introduction to Superconductivity* (Dover Publications, Mineola, New York, USA, 1996), 2nd ed.
- [160] S. de Man, K. Heeck, and D. Iannuzzi, *Phys. Rev. A* **82**, 062512 (2010).
- [161] T. R. Albrecht, P. Grütter, D. Horne, and D. Rugar, *J. Appl. Phys.* **69**, 668 (1991).
- [162] M. Nonnenmacher, M. P. O'Boyle, and H. K. Wickramasinghe, *Appl. Phys. Lett.* **58**, 2921 (1991).
- [163] A. Hadjadj, B. Equer, A. Beorchia, and P. Roca Cabarrocas, *Philos. Mag. B* **82**, 1257 (2002).
- [164] C. C. Speake and C. Trenkel, *Phys. Rev. Lett.* **90**, 160403 (2003).
- [165] R. O. Behunin, F. Intravaia, D. A. R. Dalvit, P. A. Maia Neto, and S. Reynaud, *Phys. Rev. A* **85**, 012504 (2012).
- [166] W. R. Smythe, *Static and Dynamic Electricity* (McGraw-Hill, New York, 1950), 2nd ed.
- [167] T. Hong, K. Choi, K. I. Sim, T. Ha, B. C. Park, H. Yamamori, and J. H. Kim, *J. Appl. Phys.* **114**, 243905 (2013).

-
- [168] E. van Heumen (UvA), Optical spectroscopy lab, <http://vanheumen.quantummatter.nl/>.
- [169] G. A. Campbell, *Electric wave-filter* (1917), US Patent 1,227,113.
- [170] A. Lambrecht, I. Pirozhenko, L. Duraffoung, and P. Andreucci, *EPL* **77**, 44006 (2007).
- [171] G. Joos and A. Klopfer, *Z. Physik* **138**, 251 (1954).
- [172] K. Ujihara, *J. Appl. Phys.* **43**, 2376 (1972).
- [173] G. Barton, *Rep. Prog. Phys.* **42**, 963 (1979).
- [174] J. F. Annett, *Superconductivity, Superfluids and Condensates* (Oxford University Press, 2004).
- [175] R. S. Decca, D. López, H. B. Chan, E. Fischbach, D. E. Krause, and C. R. Jamell, *Phys. Rev. Lett.* (2005).
- [176] F. Chen, U. Mohideen, G. L. Klimchitskaya, and V. M. Mostepanenko, *Phys. Rev. A* **72**, 020101 (2005).
- [177] H. B. Chan, Y. Bao, J. Zou, R. A. Cirelli, F. Klemens, W. M. Mansfield, and C. S. Pai, *Phys. Rev. Lett.* **101**, 030401 (2008).
- [178] W. J. Kim, A. O. Sushkov, D. A. R. Dalvit, and S. K. Lamoreaux, *Phys. Rev. Lett.* (2009).
- [179] G. Bimonte, D. Born, E. Calloni, G. Esposito, U. Huebner, E. Il'ichev, L. Rosa, F. Tafuri, and R. Vaglio, *J. Phys. A* **41**, 164023 (2008).
- [180] A. Lambrecht, P. A. M. Neto, and S. Reynaud, *New J. Phys.* **8**, 243 (2006).
- [181] S. J. Rahi, T. Emig, N. Graham, R. L. Jaffe, and M. Kardar, *Phys. Rev. D* **80**, 085021 (2009).
- [182] P. Antonini, G. Bressi, G. Carugno, G. Galeazzi, G. Messineo, and G. Ruoso, *New J. Phys.* **8**, 239 (2006).
- [183] D. Garcia-Sanchez, K. Y. Fong, H. Bhaskaran, S. Lamoreaux, and H. X. Tang, *Phys. Rev. Lett.* **109**, 027202 (2012).
- [184] D. Garcia-Sanchez, K. Y. Fong, H. Bhaskaran, S. Lamoreaux, and H. X. Tang, *Rev. Sci. Instrum.* **84**, 015115 (2013).
- [185] O. Suchoi and E. Buks, *Europhys. Lett.* **115**, 14001 (2016).
- [186] F. M. Buters, M. J. Weaver, H. J. Eerkens, K. Heeck, S. de Man, and D. Bouwmeester, *Phys. Rev. A* **94**, 063813 (2016).
- [187] B. S. Sheard, M. B. Gray, C. M. Mow-Lowry, D. E. McClelland, and S. E. Whitcomb, *Phys. Rev. A* **69**, 051801(R) (2004).

- [188] A. Pontin, M. Bonaldi, A. Borrielli, F. S. Cataliotti, F. Marino, G. A. Prodi, E. Serra, and F. Marin, *Phys. Rev. Lett.* **112**, 023601 (2014).
- [189] L. D. Landau and E. M. Lifshitz, *Electrodynamics of Continuous Media* (Pergamon Press, Oxford, 1960).

Samenvatting

Dit proefschrift bevat twee verschillende onderwerpen, die verbonden worden door het begrip stralingsdruk. Stralingsdruk ontstaat wanneer (electromagnetische) straling tegen een object botst en daarbij van richting verandert of wordt geabsorbeerd. Het verschil in impuls wordt overgedragen op het voorwerp dat hierdoor een kracht ondervindt. Deze kracht is in het algemeen erg klein, waardoor het effect alleen merkbaar is als er veel straling is, als het voorwerp erg klein is, of als het voorwerp goed geïsoleerd is van andere invloeden. Een bekend voorbeeld van stralingsdruk is de staart van een komeet. Die beweegt niet achter de komeet aan, zoals in eerste instantie verwacht, maar wijst altijd van de zon af door de stralingsdruk die het licht van de zon levert op het gas dat de staart van de komeet vormt. In het lab kan stralingsdruk ook gemeten worden, of zelfs worden gebruikt om de beweging van mechanische resonatoren te beïnvloeden. Als de resonator klein genoeg is, kan deze significant worden afgeremd of juist aangedreven. Deze interactie wordt onderzocht in het eerste deel van dit proefschrift. Dat straling in zijn vacuümtoestand ook druk kan uitoefenen wordt aangetoond door het Casimireffect. Dit effect wordt bestudeerd in het tweede deel van dit proefschrift. Specifiek richten we ons op de invloed van supergeleidende materialen op de sterkte van de Casimirkracht.

Optomechanica

In het vakgebied optomechanica wordt gebruikt gemaakt van stralingsdruk veroorzaakt door de reflectie van licht om de beweging van een microscopische resonator te beïnvloeden. Deze koppeling biedt de mogelijkheid om de kwantummechanische eigenschappen van het licht over te brengen op de resonator. Hierdoor zou het in de toekomst mogelijk kunnen worden om de kwantummechanische eigenschappen van relatief grote objecten te onderzoeken.

De grootte van de resonator kan sterk verschillen, net als de frequentie van het gebruikte licht. In ons systeem gebruiken we een spiegelkje met een diameter van $80\ \mu\text{m}$ dat via vier silicium nitride armpjes verbonden is met de buitenwereld. De beweging van de spiegel valt te vergelijken met dat van een trampoline, vandaar dat we spreken van een trampolineresonator. De spiegel weerkaatst infrarood laserlicht met een golflengte van $1064\ \text{nm}$. Om de interactie te versterken plaatsen we een tweede, vaste spiegel tegenover de trampolineresonator. De intensiteit van laserlicht

gevat in deze optische trillholte is vele malen sterker dan de intensiteit van het licht buiten de trillholte. Door de frequentie van het inkomende laserlicht te ontstemmen ten opzichte van de resonantiefrequentie van de trillholte, is het mogelijk de resonator af te remmen of aan te drijven. Omdat het laserlicht erg weinig ruis heeft, kan je er een lage effectieve temperatuur aan toekennen. Koppeling van de trampoline resonator met dit bad resulteert in een verminderde ruis in de beweging van de resonator en daarmee een lagere effectieve temperatuur, waardoor we het niet alleen kunnen afremmen maar ook kunnen koelen. Het mechanisme dat we hiervoor gebruiken heet optisch zijbandkoelen. Hoofdstuk twee van dit proefschrift toont aan hoe dit mechanisme werkt en hoe wij dit toepassen in onze opstelling.

We gebruiken de optomechanische interactie ook om de resonator aan te drijven. In hoofdstuk drie laten we zien dat de amplitude zo'n 450 keer vergroot kan worden ten opzichte van de thermische beweging op kamertemperatuur. Het systeem laat zich goed beschrijven door de gekoppelde bewegingsvergelijkingen van de mechanische spiegel en de optische trillholte. Dit toont de ongevoeligheid van ons systeem voor absorptie van licht.

Het optisch zijbandkoelen van de spiegel is gelimiteerd door mechanische trillingen die ruis in het spectrum veroorzaken, zodanig dat de beweging van de spiegel bij zekere koefactor niet meer waarneembaar is. Om de trampolineresonator te isoleren van deze trillingen, hebben we hem omringd met een tweede trampolineresonator, zodat een genestelde resonator ontstaat. De isolatie van de buitenresonator wordt geschat op zo'n 80 dB. Met deze constructie zijn we in staat om een effectieve temperatuur van 23 mK te bereiken vanaf kamertemperatuur. De beweging van de buitenresonator beïnvloedt echter ook de stabiliteit van de optische trillholte, wat weer een nadelig effect heeft op de mogelijkheid om optisch te koelen. Het is dus belangrijk de beweging van de buitenresonator te dempen. Dit kan met behulp van een fiberoptische interferometer om de beweging uit te lezen en terugkoppeling op basis van ofwel de elektrostatische ofwel de diëlectrische kracht. Beide mogelijkheden worden onderzocht in hoofdstuk vier.

Casimireffect

Het vacuüm is niet leeg en bevat nog altijd electromagnetische straling. Hierdoor kunnen voorwerpen in vacuüm toch stralingsdruk ondervinden. Dit wordt aangetoond door het Casimireffect, de kracht die twee ongeladen voorwerpen in elkaars nabijheid ondervinden. Deze kracht is over het algemeen heel zwak en wordt alleen significant als de twee voorwerpen dicht bij elkaar staan, op een afstand van niet meer dan een paar micrometer. De sterkte van de kracht hangt verder af van de hoeveelheid reflectie of absorptie die de electromagnetische straling ondervindt aan het oppervlak van de voorwerpen en is dus materiaalafhankelijk. De reflectie en absorptie van een materiaal worden bepaald door zijn diëlectrische permittiviteit. Die kan gemeten worden, maar alleen voor bepaalde frequenties binnen het electromagnetische spectrum, afhankelijk van de beschikbaarheid van stralingsbronnen en detectoren. Het bereik van frequenties die bijdragen aan de kracht is echter heel groot. In principe zijn dit alle frequenties tot een zekere afsnijdfrequentie, die geen bijdrage meer levert omdat de bijbehorende golflengte kleiner is dan de atomen van

het materiaal. In veel gevallen is het bereik van frequenties die bijdragen aan de Casimirkracht dus groter dan het bereik van frequenties waarbij de diëlectrische permittiviteit bekend is. Om toch een berekening van de kracht te kunnen maken, wordt de gemeten diëlectrische permittiviteit geëxtrapoleerd met behulp van modellen. Twee modellen zijn in omloop en discussie bestaat welke het beste gebruikt kan worden. Het grote verschil is de invloed van de weerstand van de vrije elektronen in het materiaal. Het Drudemodel zegt dat dit mee moet worden genomen in het bepalen van de reflectiviteit en daarmee de Casimirkracht, terwijl het volgens het plasmamodel juist weggelaten moet worden. Voor veel materialen waartussen in het verleden de kracht is gemeten leiden de modellen tot een minimaal verschil in de kracht en zijn precisieingen met zeer betrouwbare kalibratie noodzakelijk.

Om dit laatste punt wat te versoepelen is voorgesteld om de Casimirkracht te meten tussen supergeleidende materialen. Van deze materialen is bekend dat de weerstand van de vrije elektronen wegvalt. Een verschil in de kracht boven en onder de kritische temperatuur van de supergeleider zal er dus op duiden dat het Drudemodel de voorkeur heeft, een afwezigheid van dit verschil duidt op het plasmamodel. Een absolute meting van de kracht is dus niet zeer noodzakelijk, zolang aangenomen kan worden dat er verder niets in het systeem verandert met temperatuur. In hoofdstuk vijf van dit proefschrift wordt de Casimirkracht tussen supergeleidende materialen berekend.

Hoewel berekeningen vaak uitgaan van twee parallele platen in elkaars nabijheid, is het perfect parallel uitlijnen van twee platen op een afstand van ongeveer een micrometer experimenteel uitdagend. Net als veel opstellingen gebruiken wij daarom een bol-plaatgeometrie, waarbij een polystyreen bol met een straal van $100\ \mu\text{m}$ boven een vlakke plaat wordt gepositioneerd. Zowel bol als plaat zijn voorzien van een laag van 200 nm van het gewenste materiaal. In dit proefschrift is de bol bedekt met een goudlaag, terwijl de plaat ofwel een goudlaag ofwel een niobium-titaan-nitridelaag heeft. De metingen tussen twee goudlagen worden gebruikt ter kalibratie en demonstratie van onze opstelling en meetmethode. Wij gebruiken de supergeleider niobium-titaan-nitride vanwege zijn hoge kritische temperatuur en zijn ongevoeligheid voor oxidatie.

De bol zit vast aan een microscopische hefboom, zoals gebruikt in atoomkracht-microscopie. Een kracht op de bol leidt tot een uitwijking van de hefboom, wat wordt uitgelezen via fiberinterferometrie. De techniek achter fiberinterferometrie wordt beschreven in hoofdstuk zes van dit proefschrift, net als enkele andere experimentele details. Het meten van de Casimirkracht heeft nogal wat voeten in de aarde. De grootste uitdaging is de accurate kalibratie van de afstand tussen de twee oppervlakken en van de krachtsensor die gebruikt wordt. Bovendien wordt de Casimirkracht vaak overschaduwde door de elektrostatistische kracht, die ontstaat door een verschil in uittreedpotentialaal tussen de twee oppervlakten. Het is dus noodzakelijk om voor deze kracht te compenseren, maar het kan ook gebruikt worden om de opstelling te kalibreren. In tegenstelling tot de Casimirkracht is de elektrostatistische kracht afhankelijk van de spanning tussen de bol en de plaat. Door die spanning te moduleren op een bepaalde frequentie, kunnen we de beide krachten onderscheiden en de bekende elektrostatistische kracht gebruiken voor kalibratie van de krachtsensor en de afstand. Het verschil in uittreedpotentialaal kan op deze manier ook worden

gecompenseerd. Het voordeel van onze meetmethode is dat de kalibratie tegelijk geschiedt met de Casimirkrachtmeting, waardoor we minder gevoelig zijn voor veranderingen in de kalibratie over tijd. In hoofdstuk zeven van dit proefschrift laten we zien hoe onze kalibratiemethode werkt en dat we daarmee succesvol de Casimirkracht tussen twee gouden oppervlakten kunnen meten.

De Casimirkrachtmetingen tussen goud en niobium-titaan-nitride staan beschreven in hoofdstuk acht. Hier vinden we op kamertemperatuur dat de hoge weerstand van dit materiaal leidt tot een groot verschil tussen het Drude- en plasmamodel. Accurate metingen van de Casimirkracht lijken aan te tonen dat het gebruik van het Drudemodel meer overeenkomt dan het plasmamodel. Op lage temperatuur is de Casimirkracht significant sterker dan we verwachten op basis van optische reflectiemetingen. Dit lijkt geen effect te zijn van de supergeleidende toestand aangezien deze toename ook te zien is op enkele Kelvin boven de kritische temperatuur van de supergeleider. We kunnen niet uitsluiten dat het effect een technische oorsprong heeft. Rond de supergeleidende overgang van niobium-titaan-nitride zien we geen verschil in de Casimirkracht. Dit zou kunnen duiden op een betere overeenkomst met het plasmamodel, maar gezien de onverklaarde toename van de kracht bij lage temperatuur zijn we voorzichtig deze conclusie te trekken.

Vooralsnog is de gevoeligheid van de metingen gelimiteerd tot eenzelfde orde van grootte als het maximale verwachte effect van de supergeleidende overgang. Om de gevoeligheid te vergroten wordt in hoofdstuk negen de mogelijkheid onderzocht om een optomechanische trilholte, zoals beschreven in het eerste deel van dit proefschrift, te gebruiken als krachtsensor. De gevoeligheid zal hiermee vele malen kunnen toenemen.

Curriculum Vitae

Hedwig Julia Eerkens

10 February 1987 born in Diemen, The Netherlands

Sep 1999-Nov 2002 secondary education, **St. Vitus College, Bussum**

Nov 2002-Sep 2005 secondary education, **Vossius Gymnasium, Amsterdam**
thesis: *"De baan van een boemerang"*

Sep 2005-Sep 2009 bachelor Natuurkunde, **Universiteit Leiden**
thesis: *"Invloed van de membraandikte op de aggregatie van transmembrane peptiden middels elektron paramagnetische resonantie"*

Sep 2009-Apr 2012 master Research in Experimental Physics, **Universiteit Leiden**
theses: *"Kelvin Probe Force Microscopy on gold nanoparticle networks"*
"Fluctuations and transitions in weakly vibrated granular matter"

Sep 2012-Jun 2017 PhD research, **Universiteit Leiden**
Quantum Matter and Optics, promotor Dirk Bouwmeester

from Aug 2017 medical physicist in training, **VU Medical Center, Amsterdam**

List of Publications

Publications

1. Brian Pepper, Petro Sonin, **Hedwig Eerkens**, Sven de Man, and Dirk Bouwmeester, *Towards macroscopic superpositions via single-photon optomechanics* (Springer International Publishing, Cham, 2014), pp. 65-85, ISBN 978-3-319-04063-9.
2. **H. J. Eerkens**, F. M. Buters, M. J. Weaver, B. Pepper, G. Welker, K. Heeck, P. Sonin, S. de Man, and D. Bouwmeester, *Optical side-band cooling of a low frequency optomechanical system*, *Opt. Express*, **23**, 8014 (2015).
3. H. C. Overweg, A. M. J. den Haan, **H. J. Eerkens**, P. F. A. Alkemade, A. L. La Rooij, R. J. C. Spreeuw, L. Bossoni, and T. H. Oosterkamp, *Probing the magnetic moment of FePt micromagnets prepared by focused ion beam milling*, *Appl. Phys. Lett.* **107**, 072402, (2015).
4. F. M. Buters, **H. J. Eerkens**, K. Heeck, M. J. Weaver, B. Pepper, P. Sonin, S. de Man and D. Bouwmeester, *Large parametric amplification in an optomechanical system*, *Phys. Scr.* **T165**, 014003 (2015).
5. F. M. Buters, **H. J. Eerkens**, K. Heeck, M. J. Weaver, B. Pepper, S. de Man, and D. Bouwmeester, *Experimental exploration of the optomechanical attractor diagram and its dynamics*, *Phys. Rev. A* **92**, 013811 (2015).
6. F. M. Buters, M. J. Weaver, **H. J. Eerkens**, K. Heeck, S. de Man, and D. Bouwmeester, *Optomechanics with a polarization nondegenerate cavity*, *Phys. Rev. A* **94**, 063813 (2016).
7. M. J. Weaver, B. Pepper, F. Luna, F. M. Buters, **H. J. Eerkens**, G. Welker, B. Perock, K. Heeck, S. de Man, and D. Bouwmeester, *Nested trampoline resonators for optomechanics*, *Appl. Phys. Lett.* **108**, 033501 (2016).
8. F. M. Buters, K. Heeck, **H. J. Eerkens**, M. J. Weaver, F. Luna, S. de Man, and D. Bouwmeester, *High-Q nested resonator in an actively stabilized optomechanical cavity*, *Appl. Phys. Lett.* **110**, 104104 (2017).

9. F. M. Buters, F. Luna, M. J. Weaver, **H. J. Eerkens**, K. Heeck, S. de Man, and D. Bouwmeester, *Straightforward method to measure optomechanically induced transparency*, *Opt. Express* **25**, 12935 (2017).
10. **H. J. Eerkens**, F. Intraivaia, E. van Heumen, K. Heeck, S. de Man, and D. Bouwmeester, *A better comparison between the Drude and plasma model approaches using the high resistivity metal NbTiN*, to be submitted

Presentations

1. NNV AMO Lunteren 2014, "*Quest for the quantum ground state*", Lunteren, The Netherlands, contributed talk (7 October 2014).
2. Mechanical Systems in the Quantum Regime (Gordon Research Seminars), "*Exploring Nested Resonators for Optomechanical Cooling*", Ventura, California, USA, contributed talk (6 March 2016).
3. Physics@Veldhoven 2017, "*Experimental Investigation of the Effect of Superconductivity on the Casimir Force*", Veldhoven, The Netherlands, contributed talk (18 January 2017).

Acknowledgements

Science is hardly ever the result of only one person's effort. Therefore I wish to use this opportunity to thank the people that contributed to this work. I am sure that this list will be far from complete.

First of all I thank my supervisor Dirk Bouwmeester for his insights and the great amount of freedom to conduct this research. In the lab I enjoyed working closely together with Frank Buters, who taught me that patience is not always a virtue. From Sven de Man en Kier Heeck I learned to simplify problems and to clarify my thoughts. I believe this is the most valuable lesson I have learned during my research. I thank Matthew Weaver and Fernando Luna for the good times and useful discussions, both in the Netherlands and in the US. I also thank Petro Sonin, Brian Pepper and Evan Jeffrey for getting me started and showing me the details of the set-ups.

The technical support available at the institute is invaluable. I especially want to thank Harmen van der Meer from the fine mechanics department, his speed in bringing the designs to reality never ceased to amaze. Further thanks to Gert Koning and Fred Schenkel from the fine mechanics department, Arno van Amersfoort, Ko Koning and Peter van Veldhuizen from the electronics department, Wilfred van der Geest from the cryogenics department and our secretary Henriette van Leeuwen. I thank Federica Galli and Marcel Hesselberth for their support with the SEM and AFM. Operating cryostats is a skill on its own, I therefore thank Gesa Welker and Martin de Wit for saving me the effort of having to know all the details. I also thank Tjerk Oosterkamp for letting me use his cryostat for the Casimir force measurements.

I am grateful for the discussions with Wolfgang Loeffler, Martin van Exter and Michiel de Dood. It was always a very calming thought that I could walk into their offices with any question to be advised in the right direction. Francesco Intravaia was always willing to answer my Casimir force related questions and to proofread parts of my thesis, which improved my understanding significantly. I also thank Erik van Heumen for the optical reflection measurements, which proved crucial for our understanding of the Casimir force between NbTiN and gold.

In supervising students I hope to have learned as much as they have. I thank David Kok, Timo Blom and Tobias de Jong for this experience.

I am glad to have been a part of the quantum optics group during the time of my research. I will always have fond memories of our coffee breaks, sailing trips, test

defences and other traditions, and I thank the people from the group for creating those memories.

I realize that during my research I could not be available for my family and friends as much as I had wished. I am grateful for their understanding. Special thanks to my father for showing me the joys of physics from an early age. I thank my sisters for their willingness to be my paranymphs. Finally, I couldn't be more happy with Ron for joining me on the adventure called life.

Index

- BCS-theory, 61, 66
- Casimir force, 9, 12–14, 49–67, 74, 79, 82–84, 87–101, 103–105
- contact potential difference, 79, 82, 84, 85, 88, 93, 97
- dielectric permittivity, 13, 49–66, 91–97, 100, 101, 103
 - Drude model, 13, 49, 54–66, 90, 92–95, 100, 103
 - Drude-Lorentz model, 55, 56, 63, 65, 92–96, 100, 101
 - Drude-two-fluid model, 60–63, 100
 - generalized plasma model, 55, 56, 63, 65, 93–97
 - plasma model, 13, 49, 55–57, 59–62, 64–66, 90, 92, 95, 100, 101, 103
- effective linewidth, 21, 22, 28, 29, 36
- effective temperature, 11, 21–23, 33–36, 45
- electrostatic force, 13, 14, 38–45, 74, 79, 80, 82–84, 86–90, 95, 104–107
- fiber interferometry, 13, 38, 39, 42, 67–73, 76, 80–83, 86, 104, 106, 107
- FM detection, 83–86, 88, 93, 96, 99, 105, 106
- force sensitivity, 14, 32, 45, 67, 69–73, 80, 86, 97, 101, 103–107
- gravity, 9, 10, 12, 17, 18
- GRIN lens, 67, 73
- Kramers-Kronig relation, 54, 61, 93
- Lifshitz formulation, 13, 49, 51–54, 57, 90
- macroscopic quantum superposition, 9–11, 17, 18, 33
- Matsubara frequencies, 53, 56–59, 63–66, 95, 101
- mechanical vibrations, 11, 19, 31, 33–38, 45, 46, 70–72, 82
 - isolation, 19, 27, 33, 34, 39, 42, 80, 93
- Meissner effect, 50, 61, 66
- nested resonator, 11, 34, 35, 37, 40, 42, 43, 45, 107
 - inner resonator, 33–37, 40
 - outer resonator, 33–40, 43–45, 107
- noise floor (*see* force sensitivity)
- optical cavity, 10, 11, 17–23, 26, 27, 37, 38, 106, 107
 - linewidth, 17–24, 28, 36, 37
- optical cooling, 9, 11, 17–25, 29, 33–36
- optical damping (*see* effective linewidth)
- optical spring effect, 22, 23, 29, 36, 37, 106
- optomechanics, 9–11, 18, 36
- parametric oscillations, 25, 26, 29, 31

- phonon, 18, 19, 23, 29, 33, 46
- proximity force approximation, 64, 82, 87, 88, 93
- QS detection, 83–87, 90, 93, 96, 97, 99
- quantum mechanical ground state, 11, 17, 18, 23, 24, 33, 36
- radiation pressure, 9, 10, 12, 28, 29, 51
- side-band resolved regime, 18, 21, 23, 37
- superconductor, 9, 12–14, 49, 50, 54, 59–67, 76, 90, 91, 97, 98, 100, 101, 103, 104
 - dielectric permittivity, 13, 60, 61, 65, 97
- surface roughness, 67, 74, 75, 90, 106
- trampoline resonator, 11, 18, 20, 27, 33, 34, 45, 106, 107
 - mechanical linewidth, 19–21, 28, 31, 34, 36
- two-fluid model, 60–62, 65, 66, 100
- vacuum fluctuations, 9, 11, 12, 49, 51, 52, 96, 107
- van der Waals interaction, 12, 49
- zero-order mode, 53, 56, 57, 59–61, 64, 66, 95
 - TE mode, 57, 59, 61–64
 - TM mode, 57, 61